ROYAL HOLLOWAY, UNIVERSITY OF LONDON

Feasibility of Diffraction Radiation for Non-invasive Micron-scale Transverse Beam Size Measurement in Circular Machines

by

Lorraine M. Bobb

A thesis submitted in partial fulfillment for the
degree of Doctor of Philosophy

in the
Department of Physics

August 2016

DECLARATION OF AUTHORSHIP

I, Lorraine Bobb, hereby declare that this thesis and the work presented in it is entirely my own. Where I have consulted the work of others, this is always clearly stated.

Signed:

Date:

ABSTRACT

Beam size measurement using diffraction radiation has been investigated in recent years as a non-invasive counterpart to transition radiation monitors. Previous diffraction radiation monitors have been located on linear machines whereby the passage of the charged particle beam through the target aperture is somewhat simplified. For future accelerators, such as the Compact Linear Collider, the use of diffraction radiation monitors would be extended to include both linear and circular sections of the machine where high resolution non-invasive diagnostics are required.

In this thesis, the feasibility of diffraction radiation monitors for beam size measurement on circular machines is investigated. The design, installation and operation of such a monitor at CesrTA is described.

Beam size measurements of 17.6 μm and 45 μm were obtained using the diffraction radiation monitor at 600 nm wavelength. Measurements were also performed at 400 nm. Angular distributions were compared to two analytical models. Direct imaging of diffraction radiation on the target surface has demonstrated the potential of beam position monitoring as well as allowing for observations of the shadowing effect. Further discussions are made on the performance and limitations of the diffraction radiation monitor due to the complications unique to storage rings.

Acknowledgements

Firstly I would like to thank my supervisor Dr Pavel Karataev. Not only for his guidance and support during my PhD, but also for providing the foundation to my knowledge in accelerator physics from when I was an undergraduate student in his class. Without his patience in this project I would still be lost in the depths of theory. I hope to have furthered the work in Diffraction Radiation as much as he did in his own PhD thesis.

Next I must thank my CERN supervisors, Dr Thibaut Lefevre and Dr Stefano Mazzoni, for the time and energy they have invested in this project. Thibaut's enthusiasm and determination in exploring the limits of science and technology is something I will take with me in my future career in diagnostics; in addition to his work ethic of getting the job done and making sure you have fun along the way. Stefano's dedication to the project was always a source of motivation. I like to think (and hope!) he has managed to impart to me some of his vast knowledge of optics as well as his upbeat approach to problem-solving.

Thanks must also be paid to my section leader, Dr Enrico Bravin. Working within his section and from our many discussions, he has made me a better physicist whose judgement should always rely on experimental observations and a clear understanding of those observations.

I would also like to give thanks to Dr Rhodri Jones, Dr Hermann Schmickler and Professor David Rubin for their organisation and interest in this collaborative experiment. Thanks are also extended to the CLIC Collaboration.

This naturally leads me to thank those with whom I have spent many hours in the dark control room of Cesr. Dr Michael Billing has been a fountain of knowledge in all regards. From him I have learnt the importance of preparation for and problem-solving during our shifts at Cornell. I must also thank Dr Thomas Aumeyr, Joseph Conway and Dr James Shanks firstly for putting up with my somewhat maddening attention to detail and also for their humour and friendship over the last few years.

Here I should emphasise the scale of collaboration involved in this project. Between the three institutions and at each stage in the projects progression the expertise of so many people working cohesively together has been essential. In particular I would like to thank A. Apyan, S. Burger, N. Chritin, A. Goldblatt, A. Jeff, A. Nosych and S. Vulliez from CERN and J. Barley, L. Bartnik, M. Forster, T. Hawkins, Y. Li, T. O'Connell,

S. Peck, D. Rice, N. Ryder, J. Sexton, M. Stedinger, C. Strohman and S. Wang from Cornell.

Thanks must also be paid to Prof Stewart Boogert and Dr Andrew Casey, my advisor and moderator respectively for their professionalism in ensuring I have the skills needed to submit this thesis and for their pastoral care during my time in Switzerland.

With this in mind I would also like to thank Sylvia Aguilera for her friendship and kindness in both good and bad times and Joshua Stafford-Haworth for our shared love of tea and home comforts.

My greatest thanks must go to my parents who have always gone above and beyond to give me all they can in life. My motivation is to make them proud as to me, this is the best way to thank them.

Finally, I would like to thank my boyfriend Connor for his support in my time abroad and this research and most importantly, for never failing to make me smile.

Abbreviations

LHC	Large Hadron Collider
CLIC	Compact Linear Collider
MB	Main Beam of CLIC
RF	Radio Frequency
DB	Drive Beam of CLIC
MDI	Machine Detector Interface of CLIC
RTML	Ring To Main Linac of CLIC
OTR	Optical Transition Radiation
SR	Synchrotron Radiation
DR	Diffraction Radiation
TR	Transition Radiation
FTR	Forward Transition Radiation
BTR	Backward Transition Radiation
ATF(2) in KEK	Accelerator Test Facility (2) in KEK accelerator
PSF	Point Spread Function
SLAC	Stanford Linear Accelerator Center
CEBAF	Continuous Electron Beam Accelerator Facility
BPM	Beam Position Monitor
LWIP	Laser Wire Interaction Point
ILC	International Linear Collider
PETRA at DESY	Positron-Electron Tandem Ring Accelerator at the Deutsches Elektronen-Synchrotron
FDR	Forward Diffraction Radiation
BDR	Backward Diffraction Radiation
FLASH at DESY	Free-electron -LASer in Hamburg at the Deutsches Elektronen-Synchrotron
ODR	Optical Diffraction Radiation
EUV	Extreme Ultraviolet
PVPC	Projected Vertical Polarisation Component
ODRI	Optical Diffraction Radiation Interference
CESR	Cornell Electron Storage Ring
CesrTA	CESR Test Accelerator

xBSM	X-ray Beam Size Monitor at CESR
CHESS	Cornell High Energy Synchtron Source
vBSM	Visible Beam Size Monitor at CESR
CCD	Charge Coupled Device
CERN	European Organization for Nuclear Research
ICCD	Intensified CCD
MCP	Multi Channel Plate
μG	Micro Pulse Generator of ProxiKit Package camera by Proxivision
TTL	Transistor-Transistor Logic
μGDCU	Micro Digital Control Unit of ProxiKit Package camera by Proxivision
ESRF	European Synchrotron Radiation Facility
SRW	Synchrotron Radiation Workshop software by ESRF
IGOR	IGOR Pro interactive software environment
BLM	Beam Loss Monitor
HOM(s)	Higher Order Mode(s)
PMT(s)	Photomultiplier Tube(s)
BFP	Back Focal Plane
CTF3	CLIC Test Facility
OTRI	Optical Transition Radiation Interference

Contents

Abbreviations **v**

1 Introduction **1**

1.1 The Compact Linear Collider . . . 1
1.2 Diagnostics in Circular Machines . . . 3
  1.2.1 Wire Scanners . . . 3
  1.2.2 Optical Transition Radiation . . . 5
  1.2.3 Synchrotron Radiation Monitors . . . 6
  1.2.4 Laser Wire Scanners . . . 10
1.3 Motivation for Diffraction Radiation Monitors . . . 13

2 Theoretical Background **15**

2.1 Emission of Electromagnetic Radiation from Charged Particles . . . 15
2.2 Polarisation Radiation . . . 15
2.3 General Properties of Diffraction Radiation . . . 16
  2.3.1 DR in the Far-Field (Wave Zone) . . . 18
  2.3.2 DR in the Near-Field (Prewave Zone) . . . 18
2.4 DR from a Single-Edge Target . . . 20
2.5 DR from a slit . . . 22
2.6 Optical Diffraction Radiation (ODR) model and the Beam Size Effect . . . 23
  2.6.1 Projected Vertical Polarisation Component (PVPC) . . . 24
  2.6.2 ODR Model Analysis . . . 25
2.7 Optical Diffraction Radiation Interference (ODRI) model . . . 28
2.8 Target Imaging . . . 34

3 Experimental Setup **40**

3.1 CesrTA . . . 40
  3.1.1 X-ray Beam Size Monitor (xBSM) . . . 42
  3.1.2 Visible Beam Size Monitor (vBSM) . . . 44
3.2 DR Vacuum Chamber Assembly . . . 46
  3.2.1 Concept of the Vacuum Hardware . . . 46
3.3 Target and mask . . . 49
  3.3.1 Dummy Target . . . 49
  3.3.2 Chemically Etched Target . . . 50
  3.3.3 Molecular Adhesion Targets . . . 54
  3.3.4 Target Reflectance . . . 59
  3.3.5 Mask . . . 62

3.4 Optical System . . . 65
3.5 Zemax . . . 71

4 Analysis of Experimental Conditions **73**
4.1 Synchrotron Radiation Background . . . 73
4.2 Commissioning using the Dummy Target . . . 77
4.2.1 Alignment Procedure . . . 78
4.2.2 Target Imaging . . . 79
4.2.3 Beam Lifetime . . . 80

5 Experimental Results and Discussion **84**
5.1 Observation of ODR at CesrTA . . . 84
5.1.1 Vertical Polarisation Alignment . . . 84
5.1.2 Beam Alignment in the Target Aperture and Beam Position Sensitivity . . . 86
5.1.3 Shadowing of the Electromagnetic Field . . . 89
5.2 ODR Angular Distribution Measurements . . . 91
5.2.1 ODR Angular Distribution and Comparison with Theory . . . 91
5.2.2 Back Focal Plane Alignment . . . 92
5.2.3 Beam Size Effect and Analysis . . . 93
5.3 ODRI Angular Distribution Measurements . . . 98
5.3.1 Calculation of the Beam Divergence . . . 98
5.3.2 ODRI Measurements . . . 100

6 Conclusions **103**
6.1 Improvements to the CesrTA DR monitor . . . 105
6.2 Potential Application for the Large Hadron Collider . . . 105
6.3 Coherence Length Study at CTF3 . . . 107
6.4 Combined OTR/ODR Monitor at ATF2 . . . 107
6.5 Summary . . . 108

A Technical Drawings **110**

List of Figures **111**

List of Tables **116**

Bibliography **118**

Chapter 1

Introduction

1.1 The Compact Linear Collider

For decades particle accelerators have extended the energy frontier of physics exploration. The Large Hadron Collider (LHC) [1] has contributed to the verification of the Standard Model and the discovery of the Higgs boson [2]. However, to investigate physics beyond the Standard Model higher energy collisions must be observed. To complement the physics obtained through hadron-hadron collisions at the LHC, cleaner collisions could be observed using fundamental particles. An electron-positron collider in the TeV energy range allows for the investigation of new physics beyond the Standard Model, probes into the energy range of the lightest supersymmetric particles, the primary candidates for dark matter and for the testing of the existence of extra dimensions.

The Compact Linear Collider (CLIC) [3] is one option for a next generation multi-TeV electron-positron collider. Figure 1.1 shows the proposed layout for the accelerator complex designed to provide collisions with a centre-of-mass energy of 3 TeV and a luminosity of 2×10^{34} cm^{-2} s^{-1}. The injection linacs generate and pre-accelerate the Main Beams (MB) which then enter the Damping Rings for emittance reduction. At the exit of the injector complex the desired normalised beam emittances are 500 nm and 5 nm in the horizontal and vertical planes respectively. In a common booster linac the MB are further accelerated before being transported through the main tunnel to the turnarounds. After the turnarounds two main beam linacs with a combined length exceeding 40 km accelerate the MB with an accelerating gradient of 100 MV m^{-1}. In these linacs a two-beam acceleration scheme is applied. The MB are accelerated using a sophisticated approach where RF power typically generated by klystrons is replaced by a Drive Beam (DB) [3].

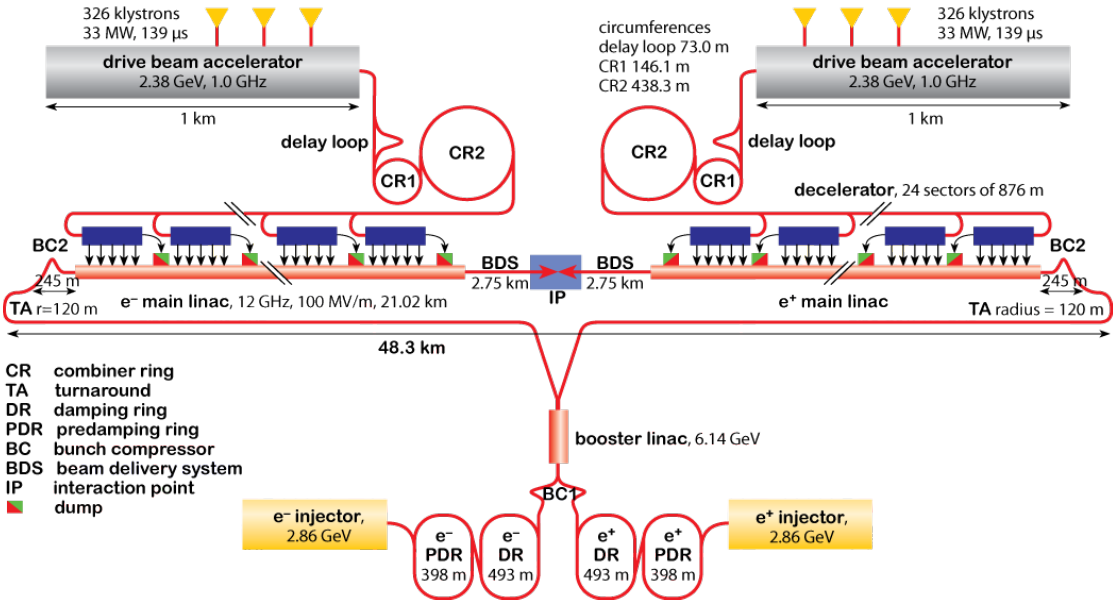

FIGURE 1.1: CLIC layout at 3 TeV [3].

Sub-systems	**Energy** [GeV]	**Resolution** [μm]	**Charge density** [nC/cm^2]
	Main Beam		
e^- source & pre-injector complex	0.2	50	$< 5 \times 10^5$
e^+ source & pre-injector complex	0.2	50	$< 5 \times 10^5$
Injector linac (e^-/e^+)	2.86	50	$< 5 \times 10^5$
Pre-Damping Rings (H/V)	2.86	50/10	$< 5 \times 10^6$
Damping Rings (H/V)	2.86	10/1	$< 5 \times 10^8$
RTML (H/V)	$2.86 \rightarrow 9$	10/1	$< 5 \times 10^8$
Main Linac (H/V)	$9 \rightarrow 1500$	10/1	$< 5 \times 10^8$
Beam Delivery System	1500	10/1	$< 5 \times 10^8$
MDI & Post-collision line	< 1500	1000	$< 5 \times 10^3$
	Drive Beam		
Source and linac	2.37	50	$< 40 \times 10^6$
Frequency multiplication complex	2.37	50	$< 40 \times 10^6$
Transfer to tunnel	2.37	50	$< 40 \times 10^6$
Turn around	2.37	50	$< 40 \times 10^6$
Decelerator	< 2.37	50	$< 1.5 \times 10^6$
Dump lines	< 2.37	100	$< 1.5 \times 10^6$

TABLE 1.1: Transverse beam size requirements for CLIC (where MDI is the Machine Detector Interface and RTML is the Ring To Main Linac) [3].

Future accelerators will typically operate using high charge density beams and transverse beam sizes on the micron-scale (see Table 1.1). To achieve high luminosity collisions, the beam is finally squeezed down to a few nanometres in the vertical direction and delivered to the interaction region. The luminosity $\mathscr{L}$ of a linear collider, defined as

$$\mathscr{L} = H_D \frac{N^2}{\sigma_x^* \sigma_y^*} n_b f_r, \tag{1.1}$$

where N is the number of particles per bunch, $\sigma_{x,y}^*$ is the horizontal (vertical) r.m.s. beam size at the collision point, n_b is the number of bunches per rf pulse, f_r is the linac repetition rate and H_D is the overall luminosity enhancement parameter representing the combined effect of the hour-glass (i.e. the change of beta function in longitudinal direction over the collision region) and the disruption enhancement (due to the attractive force that the two colliding bunches exert on each other) [3, 4]. Therefore the transverse beam dimensions must be monitored at every stage of the beam production, acceleration and delivery.

1.2 Diagnostics in Circular Machines

Diagnostic instruments in circular accelerators may be categorised into two groups: invasive and non-invasive. Traditional diagnostics fall into the first category, whereby measurement of the beam is obtained through the direct interaction of the beam with matter. Optical Transition Radiation (OTR) monitors [5], fluorescent screens [6] such as YAG or phosphor and wire scanners [7, 8] all fall into this category. Non-invasive instruments such as Synchrotron Radiation (SR) [9, 10] and Diffraction Radiation (DR) [11, 12, 13, 14] monitors exploit radiative processes due to the interaction of the electric field of the charged particle beam, rather than the beam itself, with matter. Laserwires [15, 16, 17] also fall into this non-invasive category.

1.2.1 Wire Scanners

In many accelerators, wire scanners are used as the standard reference devices for beam profile measurements. Wire scanners intercept a fraction of the particles across multiple bunches of the beam. Therefore they are considerably less invasive than other beam profilers. Often they are used to calibrate “online” instruments such as SR monitors [8].

A wire scanner consists of a thin (10 - 50 μm) wire as shown in Figure 1.2 which is swept through the beam. The interaction between the wire and the particle beam produces highly energetic radiation. These secondary particles are detected with scintillation

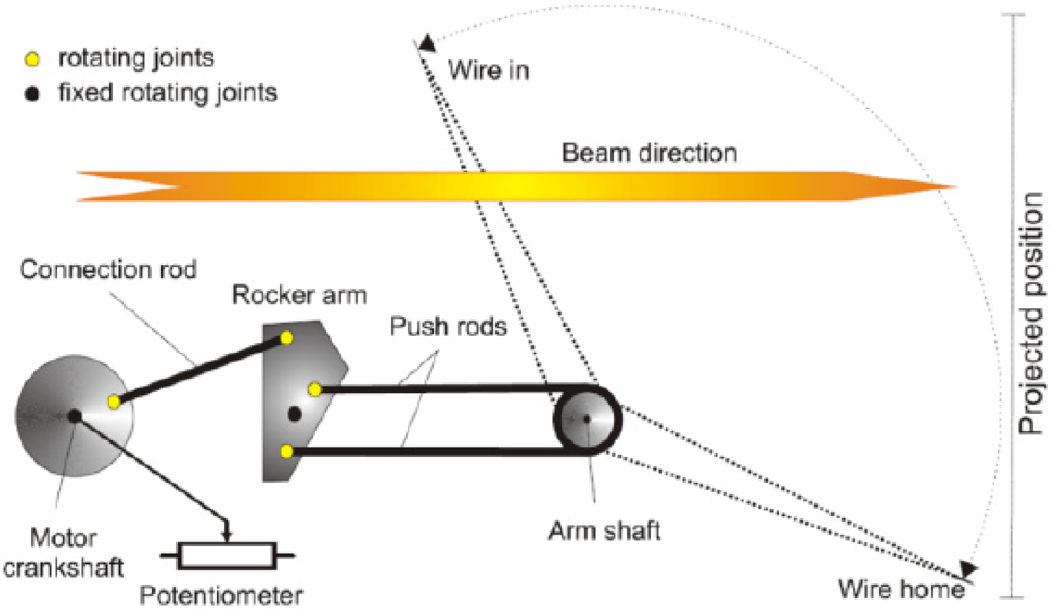

FIGURE 1.2: Schematic of the PS and PSB rotational wire scanner [8].

counters or Cherenkov detectors [7]. The signal is proportional to the number of particles of the beam which interact with the wire. By simultaneously recording the wire position and signal amplitude a beam profile is obtained [18]. It should be noted that single shot beam profile measurements are not possible due to the limited speed of the wire scanner. A wire scanner measures the average beam profile by sweeping through consecutive bunches of the charged particle beam.

Typically the wire is swept at a high speed (1 to 15 ms^{-1}). To move the wire at this high speed a circular movement is employed. However this has the detriment of reducing the position resolution and hence the profile resolution from 10 μm to 100 μm. The sweep speed or more accurately the acceleration, is primarily limited due to the stress properties of the surrounding components [18].

Although wire scanners are implemented on many circular machines there are some drawbacks. Heating of the wire due to the energy deposited by very intense particle beams can lead to wire breakage. The wire may also break due to the energy transferred through the interaction of the wire with the electromagnetic field of the particle beam. Further to these damage risks, vacuum leakage in the bellows due to wear may also occur.

With regards to the beam profile measurement itself, inaccuracy of the wire position measurement due to vibrations of the wire and associated mechanics and the beam stability are additional sources of error [19, 8].

1.2.2 Optical Transition Radiation

Transition radiation (TR) is generated when a charged particle crosses the interface between two media. Similarly to DR, polarisation currents are formed on the surface resulting in the emission of photons [20]. The photons are emitted in two directions: along the path of the charged particle beam known as Forward Transition Radiation (FTR) and in the direction of spectral reflection known as Backward Transition Radiation (BTR). Using the BTR, primarily in the optical spectral range, the two dimensional beam profile, tilt angle and position may be measured in a single shot.

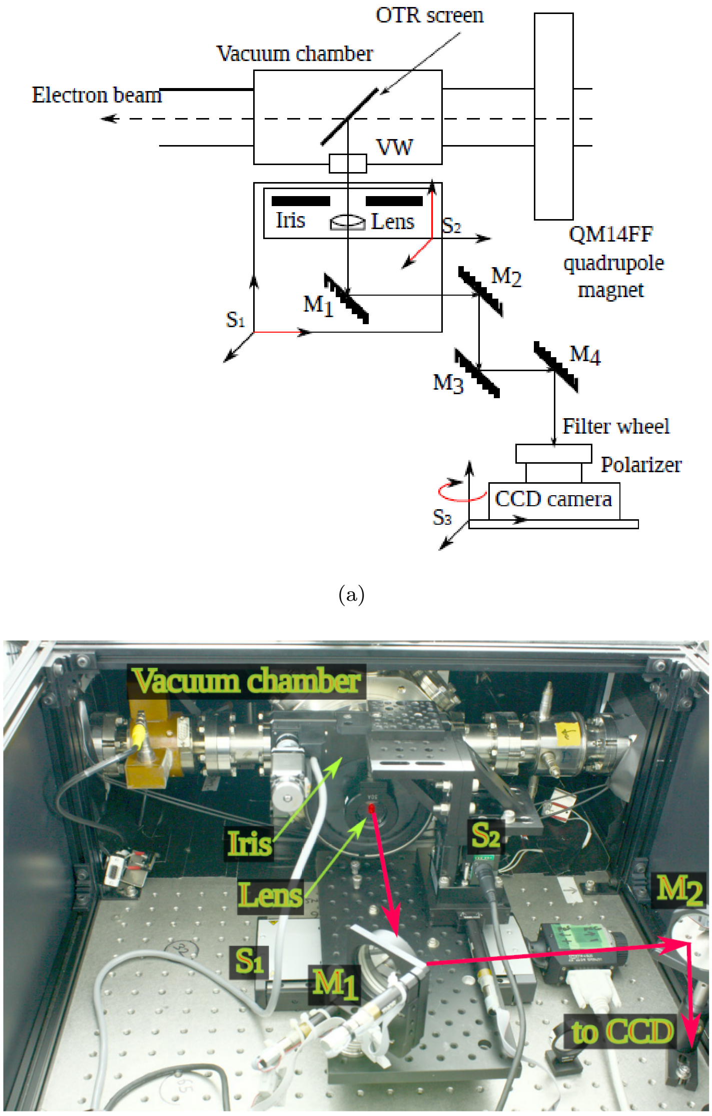

(a)

(b)

FIGURE 1.3: Schematic (a) and photograph (b) of the OTR bean profile monitor at ATF2 [5].

Figure 1.3 shows one of the most recent Optical Transition Radiation (OTR) monitors based at ATF2 in KEK. The charged particle beam passes through the target which is typically made from silicon with a reflective coating such as aluminium. The target is tilted at 45 degrees relative to the incident electron such that BTR is directed out of the beampipe through a viewport into the optical system for detection. OTR monitors are highly invasive and measurements performed with these devices may destroy the beam or the monitor itself. For these reasons, the use of OTR monitors in high intensity future accelerators is restricted to low current pilot beams to complement measurements acquired using laserwire scanners [5].

There was a concern that OTR monitors may not be suitable for measurements on future accelerators because the spatial resolution of the instrument decreases with increasing beam energy. The resolution of traditional OTR monitors is defined by the root-mean-square of the so-called Point Spread Function (PSF) [21]. In the optical spectral range, the PSF is defined as the OTR distribution generated by a single electron and propagated through the optical system to the detector. Predominantly at these wavelengths the resolution is limited due to broadening caused by diffraction and aberration effects of the optical system [22, 5]. A conventional OTR monitor at SLAC achieved the best resolution of a few micrometres [23].

Recently, the resolution of conventional OTR monitors has been significantly improved. The OTR PSF differs from the conventional PSF of an optical system [22]. The vertical polarisation component of the OTR PSF exhibits a two-lobe structure from which the visibility can be used to monitor the vertical beam size with sub-micrometre resolution. Furthermore, provided the beam is flat as is the case for linear colliders, the horizontal beam size may be directly obtained from the horizontal projection of the OTR distribution. Thus allowing two-dimensional transverse beam size measurement [5].

The use of OTR monitors in circular machines is complicated due to their invasive nature. However experiments have been performed on low energy circular machines such as at the Continuous Electron Beam Accelerator Facility (CEBAF) [24]. In this case a 100 μm beam size was measured using an aluminium foil target and 3.2 GeV beam energy, although the instrument was limited to low current operation only. Thus making it unsuitable for high charge, low emittance circular machines where significant damage to the target is likely to occur.

1.2.3 Synchrotron Radiation Monitors

In circular accelerators, principally for storage rings in the light source community, the synchrotron radiation (SR) emitted by electrons can be used for non-destructive beam diagnostics. Like CLIC, third generation and future light sources require low emittance beams of a few nm rad or less. Several methods have been established for transverse beam profiling and can be classed under the following three categories: direct imaging where the electron beam size information is encoded in the photon spot size; interferometry where the spatial coherence of SR is investigated by measuring the blurring of the interferogram produced using a double slit setup and finally the projection method where spatial beam properties are determined from the angular distribution of SR.

The most commonly used techniques are direct imaging using pinhole cameras (see Figure 1.4) and interferometry (see Figure 1.6) [25].

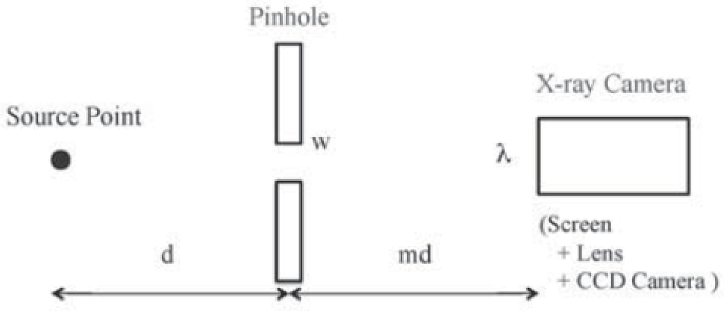

FIGURE 1.4: Schematic of a pinhole camera where d is the source-to-pinhole distance, md is the pinhole-to-detector distance, w is the pinhole aperture size and λ is the wavelength [26].

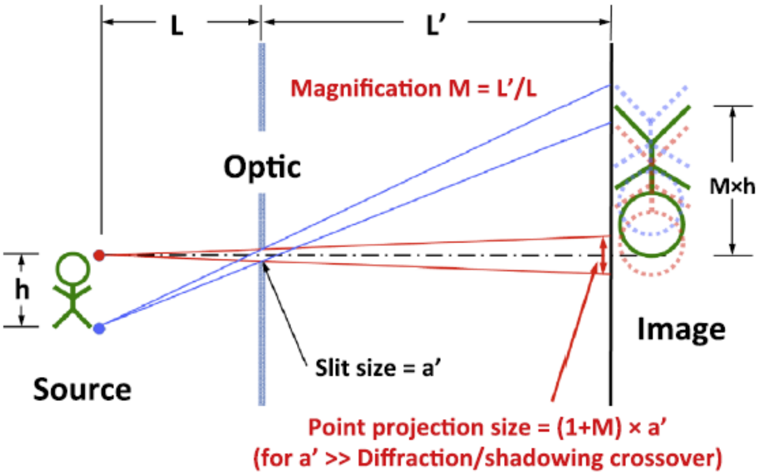

FIGURE 1.5: Imaging principle of a pinhole camera. In this example h is the object height i.e. the electron beam size, L is the object-to-pinhole distance, L' is the pinhole-to-image plane distance and a' is the pinhole size [9].

The measurement principle of the pinhole camera imaging system is shown in Figure 1.5. The object of the imaging system is the electron beam size. By choosing an appropriately small pinhole size, photons emitted from each transverse position h in the electron beam will propagate to a corresponding position on the image plane. The reader should note that due to the finite size of the pinhole, each position on object plane will emit a light cone and thus will have an associated point projection size.

For detection using low cost cameras a magnification greater than 1 is often chosen such that the beam size is resolvable given the pixel size among other parameters of the camera.

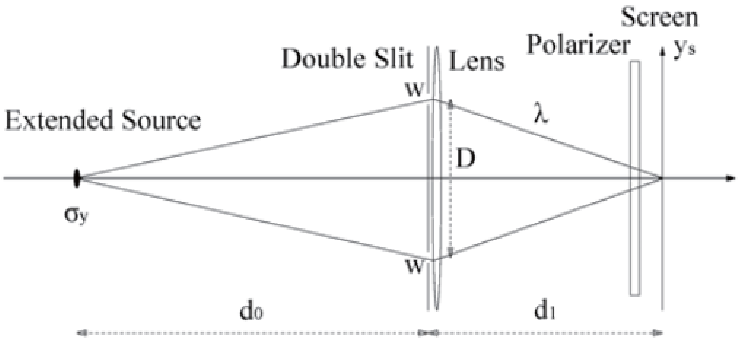

FIGURE 1.6: Schematic of a SR interferometer where d_0 is the source-to-double slit distance, d_1 is the double slit-to-detector distance, w is the slit aperture size, D is the interslit distance of the double slit screen and λ is the wavelength [26].

Pinhole cameras directly image SR emitted from bending magnets and undulators. The SR emitted has a broad spectral range from the Infrared (IR) to X-rays and is characterised by the critical frequency w_c^{SR} as

$$w_c^{SR} = \frac{3}{2}\frac{\gamma^3 c}{\rho}, \tag{1.2}$$

where γ is the Lorentz factor, c is the speed of light and ρ is the dipole bending radius [25]. Through the measurement of the SR photon spot size at the detector, the transverse size of the electron beam at the source can be determined. An emittance ε_i measurement can then be made using the measured transverse size of the electron beam combined with the optics of the machine using the relation

$$\varepsilon_i = \frac{\sigma_i^2 - (\sigma_E/E)^2\,\eta_i^2}{\beta_i}, \qquad i = x, y, \tag{1.3}$$

where σ_i is the beam size, σ_E/E is the relative energy spread, η_i is the slip factor which relates the fractional change in the orbit period to changes in energy and β_i is the beta function [26].

The spatial resolution of an X-ray pinhole camera $S_{Pinhole}$ is given by

$$S^2_{Pinhole} = S^2_{Diffraction} + S^2_{Aperture} \tag{1.4}$$

where $S_{Diffraction}$ and $S_{Aperture}$ are contributions from diffraction and the finite aperture size of the pinhole respectively [26]. The point spread function (PSF) of the pinhole system,

$$S_{PSF}^2 = S_{Pinhole}^2 + S_{Imaging}^2 \tag{1.5}$$

is a combination of the blurring caused by the pinhole $S_{Pinhole}$ and that by the imaging system $S_{Imaging}$ i.e. lens, scintillator and detector. In 2010 at MAX III using a UV-visible imaging system a vertical beam size of (28.9 ± 1.1) μm was measurable [10].

Generally, the resolution of beam size monitors using direct imaging techniques at optical wavelengths is diffraction limited. The spatial resolution is improved by operating at shorter wavelengths typically in the X-ray spectral-range. An optical system designed for the transportation of X-rays is often complex and expensive. The system may need to be under vacuum and require the conversion of X-rays to longer wavelengths for detection using readily available cameras.

To convert X-rays to photons in the UV and visible spectral range a scintillator screen is required. It should be noted that the choice of scintillator is very important in this conversion process: the material density, light yield and emission wavelength must be considered. Furthermore the use of a scintillator will contribute to the point spread function of the imaging system, in effect resulting in a reduction of the spatial resolution of the system. The PSF of the scintillator and imaging system from the scintillator screen to the camera may be measured by fitting an error function to a 1D slice of the image when a tungsten knife-edge is placed directly upstream of the scintillator screen.

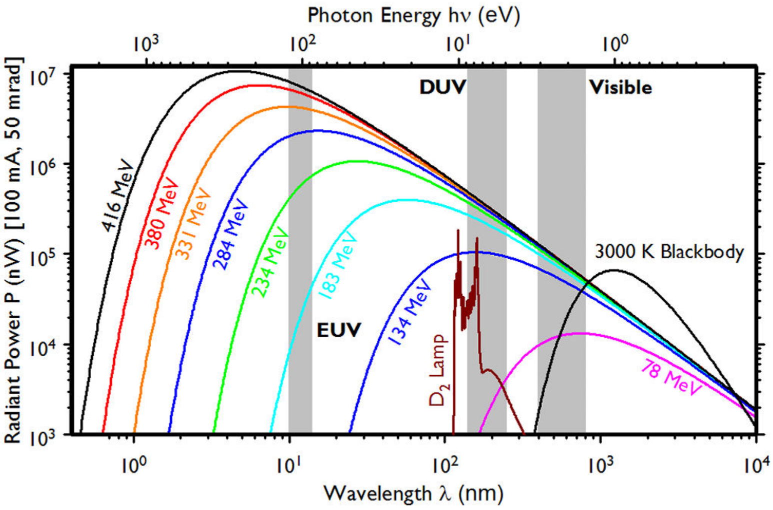

FIGURE 1.7: A plot of the SR power vs wavelength for different beam energies [27].

The main advantage of SR based monitors is that unlike other beam size monitors, as the beam energy increases the peak power of the SR emission spectrum is shifted to shorter wavelengths hence the spatial resolution increases. This property of SR is ideal for future high energy accelerators. To ensure a sufficient SR intensity the exposure time for images in storage rings is typically a few ms [10]. This is possible provided the beam is stable. At this point it should also be noted that the choice of SR wavelength not only dictates the optical system design but also the operation of the detection system. For linear accelerators with SR production locations, such as the turnarounds in CLIC, single-shot measurements are required. Therefore low SR light intensity could be another limitation in the application of SR based beam size monitors although the option of multi-turn measurements overcomes this problem.

It is evident that the application of SR monitors for beam size measurements is limited by the number of bending magnets and undulators in the machine. For linear accelerators such as CLIC there are few locations of SR production other than the damping rings and turnarounds. Furthermore, in a single shot it is very difficult to generate sufficient numbers of photons therefore images are typically acquired over multiple turns of a circular machine or for multiples bunches/trains.

1.2.4 Laser Wire Scanners

Laser wire scanners employ the inherently non-destructive process of inverse Compton scattering [28]. A laser is scanned in the transverse (horizontal or vertical) direction across the electron beam. At each laser position, photons of the laser are Compton scattered by the electrons of the beam. The rate of this interaction is low therefore this technique is naturally non-invasive. A detector is located downstream to count the number of Compton scattered photons at each position of the laser during the scan. The number of scattered photons at a given laser position is dependent on the number of electrons in the beam at that position. From this, the spatial distribution of the electron beam can be reconstructed [29].

A laser wire system, as shown in Figure 1.8, consists of several major components: a high power laser, optical transport and scanning system, vacuum interaction chamber, beam position monitor (BPM) and detection system. Laser pulses interact with electrons at the laser wire interaction point (LWIP). The LWIP is dependent on the electron beam orbit read out by neighbouring BPMs. The pulses are focussed to produce a diffraction limited laser waist at the LWIP. The detection system is located downstream of the LWIP. Between the LWIP and detection system a dipole magnet is used to separate the Compton scattered photons from the electron beam [17].

There are four main requirements on the laser for accurate measurement of the electron beam size. Firstly, the laser spot size must be smaller size than that of the electron beam.

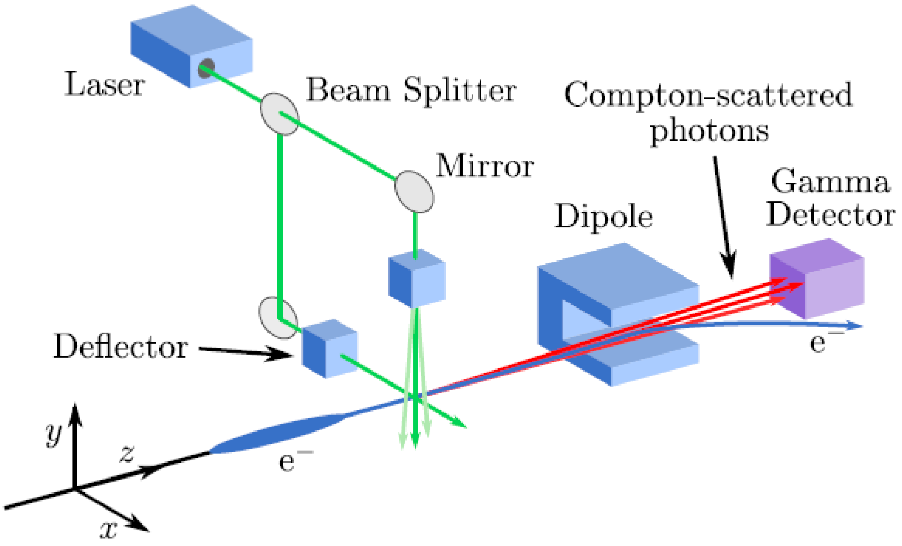

Figure 1.8: Laser wire schematic [17].

Secondly, it must be of sufficient intensity to produce a detectable number of Compton scattered photons relative to the detector background environment. Thirdly, to create the micron-scale focused spot-sizes needed for use in a laserwire at the International Linear Collider (ILC) or CLIC the laser must have an excellent spatial beam quality [17]. The laser duration must be shorter than the time separation between subsequent bunches to eliminate bunch-by-bunch instabilities.

The diffraction limit defines the smallest spot-size to which the laser may be focused which is approximately equal to the wavelength of the laser light. Therefore when considering the focused spot-size of the laser it is preferable to operate the laserwire at shorter wavelengths. However, for most optical materials strong absorption occurs for wavelengths shorter than 300 nm. For this reason when operating at shorter wavelengths, reflective rather than transmissive optics must be used [17] such as mirrors mounted on piezo-driven stages [28, 16]. At the Stanford Linear Collider, using a reflective focusing geometry an ultraviolet laser demonstrated scans with micrometer size and submicrometer resolution [30].

The primary disadvantage to incorporating a reflective focusing geometry is that it prevents direct measurement of the laser focus and therefore calibration. The system is also limited to a very short scanning range due to the optical aberrations when the focusing mirror is used off-axis e.g. when the laser or mirror is moved to scan the focused laser spot across the beam. A solution to this is to opt for transmissive optics which provide a greater scanning range and direct measurement of the focused spot-size [17]. Driven by these considerations, the optimal focusing system operates at visible wavelengths generated by frequency doubling a near infrared source. This compromise increases the resolution of the laserwire with the detriment of reducing the peak power [31].

Similarly to wire scanners, a disadvantage of laserwire scanners is that they cannot perform single-shot measurements. A scan, consisting of multiple passes of the electron bunch, is required for reconstruction of the electron beam profile. The rate of this scan is determined by the number of laser positions required, the speed of repositioning the optical components to change the laser position and the speed of data acquisition by the detector. This process is heavily dependent on the stability of the electron beam. Therefore this dependence on precise positioning and high stability of the charged particle beam is an additional complication in the operation of laserwire scanners.

Beam profile measurements using laserwire scanners have been conducted at the Positron-Electron Tandem Ring Accelerator (PETRA) at DESY. The PETRA accelerator bunch clock provided trigger signals to synchronise the laser pulses with the positron trains. Laser pulses were triggered to interact with the first bunch of the train. In 2004, a vertical beam size of $(68 \pm 3_{stat} \pm 14_{sys})$ μm was measured [16]. This system was later upgraded to provide two-dimensional beam profiles where beam dimensions of (46.5 ± 0.6) μm and (377.3 ± 3.0) μm were extracted in the vertical and horizontal directions respectively [28].

In recent years, at the Accelerator Test Facility (ATF2) at KEK laserwire scans have measured vertical beam sizes as small as (1.16 ± 0.06) μm [15]. This was achieved despite using a laser with a non-Gaussian profile and the large aspect ratio of the electron beam.

To measure beam sizes on the micron-scale, systematic effects of the laser wire must be considered. The resolution of the beam size measurement is determined by the beam waist of the laser. The width of the laser beam changes as a parabola along its beam axis. The measured width of a beam profile σ_{obs} is a convolution of the electron beam size and the laser beam size at the LWIP, which may be calculated as

$$\sigma_{obs} = \sqrt{\sigma_e^2 + \left(\frac{w_0}{2}\right)^2 \left(1 + \left(\frac{\lambda_{las} z_{las}}{\pi w_0^2}\right)^2\right)}, \tag{1.6}$$

where w_0 is the beam waist of the laser, z_{las} is the width of the laser beam, σ_e is the electron beam size and λ_{las} is the laser wavelength [32]. Various methods have been established to ensure the laser beam waist occurs at the LWIP [32] [15].

Laserwire scanners are the best candidate at future accelerators for non-invasive, high resolution transverse beam size measurement. However, it must be noted that they are still not the perfect instrument for the job and do have many disadvantageous aspects in their operation and maintenance such as the high stability requirements of the laser and electron beams, and the need of a team of highly trained operators. Furthermore, for future large-scale accelerators such as CLIC, the number of laserwire scanners required would be very expensive due to the complex design of the system and the quantity of high-power lasers. Therefore complementary, cheaper alternatives must be investigated.

1.3 Motivation for Diffraction Radiation Monitors

Diffraction radiation (DR) is the instantaneous emission of photons when a relativistic charged particle moves in the vicinity of a medium. The electric field of the charged particle polarizes the target atoms which then oscillate, emitting radiation with a very broad spectrum known as DR. It should be noted that no DR is produced by a charged particle moving along a continuous boundary, in this case, Cherenkov radiation may be emitted.

Much like TR, DR is also emitted in two directions from the target: in the direction of the moving charge known as Forward Diffraction Radiation (FDR) and in the direction of specular reflection known as Backward Diffraction Radiation (BDR). BDR is measured for non-invasive beam diagnostics since it is emitted away from the charged particle given a suitable target tilt angle. The spatial-spectral properties of DR are sensitive to a range of electron beam parameters. Furthermore, the energy loss due to DR is so small that the electron beam parameters are unchanged (i.e. remain nearly same as the initial parameters). Therefore DR can be used to develop non-invasive diagnostic tools.

In the optical wavelength range the use of diffraction radiation (ODR) as a high-resolution non-invasive diagnostic tool for transverse beam size measurement has been widely investigated; at the Accelerator Test Facility at KEK in Japan [33], at the FLASH light source at DESY [34] and at the Advanced Photon Source at Argonne, USA [14]. The visibility of the ODR pattern was measured at ATF, compared with the simulated data and the beam size was determined. At ATF the achieved beam size sensitivity was as small as 14 μm. The resolution of this system was limited by the diffraction limit, system configuration (e.g. precision of the slit geometry and alignment) and non-optimal measurement system, as well as by the residual contribution from SR [33].

All DR experiments to date have been conducted on linear accelerators. Therefore another area of investigation is to determine whether DR can become a limit of linacs. It is known that coherent DR in which all charged particles of a bunch react in the same way, is much stronger than incoherent DR i.e. there are significantly more photons produced via coherent DR. In theory, DR may be emitted whenever an electric field of a relativistic particle interacts with a medium. This case can arise through every section of a machine as the beam passes through irises. These photons may then react with matter producing secondary particles. It is possible that DR may impact the bunch itself. Therefore the impact of DR on beam quality (i.e. the presence of DR photons acting on a beam) should be investigated.

The aim of this project is to investigate the feasibility of DR monitors for transverse beam size measurement on circular machines. Ideally these measurements will be on the micron-scale using incoherent DR with the intention to investigate the applicability of DR monitors to the MB and DB of CLIC. A successful DR beam size monitor would be used alongside laserwire scanners of which there are more than 100 beam size monitors required from the exit of the Damping Ring to the Main Linac [3]. A simpler version of the monitor, requiring a more relaxed performance (see Table 1.1) could also be implemented on the DB complex.

In contrast to laser wire scanners, DR monitors have the capability of performing single-shot beam size measurements. For single-shot measurements the only limitation comes from the DR intensity. However through careful selection of the DR wavelength and the use of intensifiers in the detection system, the light intensity is not expected to be a limiting factor. Furthermore, the costly maintenance of the high power laser in the laser wire system is not applicable to DR monitors.

Unlike SR monitors, DR based instruments could be located throughout the machine preferably on linear sections. They also offer the capability of acquiring high resolution beam size measurements on the micron-scale.

Installing a DR monitor on a circular machine introduces further advantages and disadvantages not applicable to linacs. For use on the ring, the target must be redesigned such that it may be retracted for beam injection and aligned with the stored electron beam. A larger target aperture may be necessary for sufficient beam lifetime. Although this reduces the DR intensity this problem may be overcome by acquiring integrated images over multiple turns of the ring. A DR monitor on a ring also allows investigation of the wakefield effects caused by material in the vicinity of the beam and the effect on the betatron tune. Another important aspect is the understanding of the SR contribution and suppression in beam size measurements using DR.

The first phase of the DR monitor operates in the visible to UV spectral range. To achieve a resolution smaller than 10 μm, an upgrade of such a system should be followed up to measure DR at extreme UV (EUV) and X-ray wavelengths. The subject of this thesis is to study the spatial resolution limit of such a device for high-energy beams with specific attention to those in circular machines.

In this project we consider an electron beam passing through a slit target. It is expected that DR provides an alternative option for the development of non-invasive diagnostic devices. However, this non-invasiveness must be verified for both coherent and incoherent DR.

Chapter 2

Theoretical Background

For high charge-density beams invasive diagnostic systems such as OTR monitors [35, 22] and wire scanners [7] cannot be used without risking damage to the instrumentation. Laser-wire scanners [15, 16, 17] are the primary candidate for non-invasive, high resolution, transverse beam size measurements. However, for large-scale accelerators the quantity required could become costly and require extensive maintenance. For these reasons Diffraction Radiation (DR) monitors are being investigated as an alternative [36, 37].

2.1 Emission of Electromagnetic Radiation from Charged Particles

Electromagnetic radiation is produced when a charged particle undergoes a change in acceleration such as the case of synchrotron radiation whereby charged particles change direction as they pass through dipole magnets. In a similar way, bremsstrahlung, the so-called “breaking radiation”, is emitted when charged particles are decelerated as they pass through matter. Unlike synchrotron radiation where the bending force and acceleration are both normal to the particle trajectory, for bremsstrahlung the force is usually applied in opposition to the velocity vector [38].

2.2 Polarisation Radiation

Polarisation radiation occurs due to the dynamic polarisation of a medium. The electromagnetic field of the charged particle generates polarisation currents in the medium leading to the emission of photons. Maxwell's equations for the time Fourier transforms of fields and currents in a medium have the form

$$\nabla \times \mathbf{H}(\mathbf{r},\omega) = \frac{4\pi}{c}\mathbf{j}(\mathbf{r},\omega) - i\frac{\omega}{c}\varepsilon(\omega)\mathbf{E}(\mathbf{r},\omega), \tag{2.1a}$$

$$\varepsilon(\omega)\left(\nabla \cdot \mathbf{E}(\mathbf{r},\omega)\right) = 4\pi\rho(\mathbf{r},\omega), \tag{2.1b}$$

$$\nabla \times \mathbf{E}(\mathbf{r},\omega) = i\frac{\omega}{c}\mathbf{H}(\mathbf{r},\omega), \tag{2.1c}$$

$$\nabla \cdot \mathbf{H}(\mathbf{r},\omega) = 0, \tag{2.1d}$$

where $\mathbf{H}$ is the magnetic field, $\mathbf{E}$ is the electric field, $\varepsilon(\omega)$ is the relative permittivity, $\mathbf{j}$ and ρ are the current and charge densities respectively, that correspond to the motion of the charged particle [39].

Depending on the choice of target, polarisation radiation is observed via several different processes: Cherenkov radiation, transition radiation (TR), diffraction radiation (DR), Smith-Purcell radiation and parametric X-ray radiation in crystals. The source of diffraction radiation is the polarization current $\mathbf{j}$ that is generated by the field of the particle and whose time Fourier transform can be represented in the form

$$\mathbf{j}(\mathbf{r},\omega) = \frac{i\omega}{4\pi}\left\{1 - \varepsilon(\mathbf{r},\omega)\right\}\mathbf{E}(\mathbf{r},\omega) \equiv \sigma(\mathbf{r},\omega)\mathbf{E}(\mathbf{r},\omega), \tag{2.2}$$

where $\mathbf{E}$ is the electric field, $\varepsilon(\mathbf{r},\omega)$ is the relative permittivity and $\sigma(\mathbf{r},\omega)$ is the conductivity of the medium [39].

As described in Chapter 1, TR describes photons which are emitted when a charged particle crosses a medium boundary such as when passing through a screen in vacuum. This invasive interaction is used for beam size measurement in OTR monitors. DR may be considered as the non-invasive form of TR. In this case the screen is replaced by a target with an aperture. The charged particle beam passes through this aperture, whilst the electric field associated with the beam interacts with the target medium. For Smith-Purcell radiation the target is replaced by a grating [39]. The reader should be aware that the general mechanism underlying TR, DR and Smith-Purcell radiation is the same.

2.3 General Properties of Diffraction Radiation

When a charged particle moves in the vicinity of a medium the electric field of the charged particle excites atomic electrons of the medium. Polarisation currents are produced which are accompanied by the emission of electromagnetic waves i.e. the emission of photons [39]. Diffraction Radiation (DR) describes photons which are emitted when a charged particle passes through a target aperture. In this case the charged particle does not intersect the boundary of the medium but interacts with the medium via its electric field.

The DR spectral angular distribution can be calculated using

$$\frac{d^2W}{d\omega d\Omega} = 4\pi^2 k^2 \left(|E_x|^2 + |E_y|^2 \right), \tag{2.3}$$

where the wave number is defined as $k = 2\pi/\lambda$ and $E_{x,y}$ are the polarisation components of the radiation integrated over the target surface. The total field of the radiation is dependent on the incident charged particle field [11, 39].

The emission of DR is dependent on the distance between the charged particle trajectory and the medium. It is known that the field of a moving charge in vacuum with velocity $\mathbf{v}$, frequency ω and energy $E = \gamma mc^2$ where γ is the Lorentz factor, m is the rest mass of the charged particle and c is the speed of light decreases as $\exp(-h_d\omega/\gamma v)$ with distance h_d in the direction perpendicular to the charged particle velocity. Therefore, DR polarisation currents are located in the layer close to the surface and the properties of DR depend strongly on the properties of this layer. Furthermore, DR does not appear for a charged particle uniformly moving in parallel with an infinite plane surface of a homogeneous medium [39].

The impact parameter h defined as

$$h \leq \frac{\gamma\lambda}{2\pi}, \tag{2.4}$$

where γ is the Lorentz factor and λ is the wavelength, shown in Figure 2.1 describes the condition on the distance from the beam to the slit edge for the emission of DR. This condition is defined by the effective electric field radius of the charged particle $r_E = \gamma\lambda/2\pi$ [40].

As shown in Figure 2.1, DR is emitted in two directions. Forward Diffraction Radiation (FDR) is emitted in the direction of the charged particle trajectory. Backward Diffraction Radiation (BDR) is emitted in the direction of specular reflection relative from the target.

For high energy beams the emission of DR is considered to be non-invasive. The energy loss of the charged particles to DR is much less than the energy of the fast moving

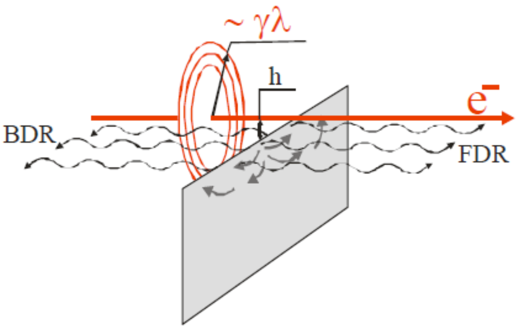

Figure 2.1: Schematic of DR emission from a particle moving in the vicinity of a medium [11]

charged particle. For this reason the particle velocity can be treated as constant to a good accuracy [39] and DR, particularly BDR, can be used for non-invasive beam diagnostics in low background conditions.

2.3.1 DR in the Far-Field (Wave Zone)

The far-field zone is the region at which the angular distribution of DR is observed. The distance from the target to the observation point is assumed to be so large that it is possible to introduce the DR field as a superposition of plane waves of different amplitude emitted by each elementary source of the target. In this case Fraunhofer diffraction theory can be used [40].

The wave zone is defined by the far-field condition of the form

$$\frac{L}{\gamma} \gg \frac{\gamma\lambda}{2\pi} \qquad \rightarrow \qquad L \gg \frac{\gamma^2\lambda}{2\pi}, \tag{2.5}$$

where L is the distance from the target to detector, γ is the Lorentz factor and λ is the DR wavelength [40]. From this condition it is seen that in the far-field the distance L/γ must be significantly greater than the electric field radius $r_E = \gamma\lambda/2\pi$.

The angular distribution of DR is emitted in a cone of order $\theta = \gamma^{-1}$ where $\theta^2 = \theta_x^2 + \theta_y^2$ is the polar observation angle as shown in Figure 2.2.

2.3.2 DR in the Near-Field (Prewave Zone)

The region where the far-field condition is not satisfied is called the “prewave zone”. In this case, the DR distribution observed is a spatial-spectral distribution; it not purely angular but includes a spatial contribution determined by the radiation source size.

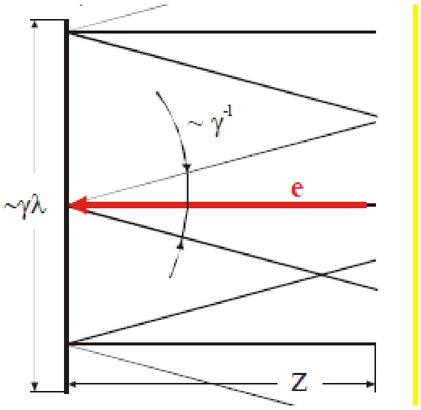

FIGURE 2.2: Schematic of the emission cone angle for TR (shown here) and DR for three elementary sources on the target within the electron effective field radius [11].

This radiation source size is equal to the electric field radius which can be treated as the effective radius $r_E = \gamma\lambda/2\pi$ as shown in Figure 2.1. For a detector located in the prewave zone, DR photons with different emission angles arrive at the same observation point on the detector plane [40].

The spatial distribution is transformed into the angular distribution in the far-field zone only [40]. As aforementioned, this can be achieved by satisfying the far-field condition for example by using a long-line optical system where the detector is located far away from the DR target.

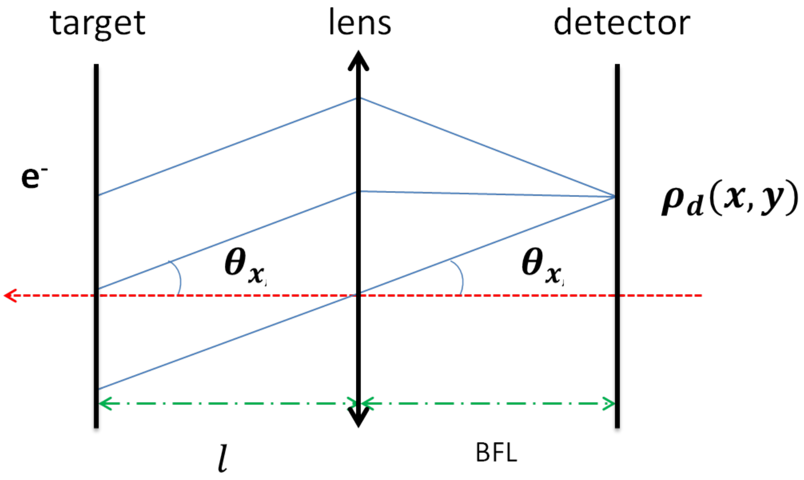

FIGURE 2.3: Geometry of photon propagation in the prewave zone suppression setup using a thin lens where l is the distance from the target to the lens, BFL is the back focal length of the lens and $\rho_d(x, y)$ is the position of emission angle $\theta_{x,y}$ on the detector plane.

If the far-field condition cannot be satisfied due to spatial constraints, the DR angular distribution may be obtained in the prewave zone through the use of a lens where the detector is positioned at the back focal plane. This setup can be considered as an alternative case of Fraunhofer diffraction as described in [41].

A detailed report on the methods of prewave zone suppression can be found in [40]. Here, the propagation of BDR through a thin lens is discussed since this setup was used for the experiment at CesrTA due to spatial constraints and the simplicity of installation and alignment in the machine.

In Figure 2.3 the geometry of the photon propagation in the prewave zone setup through a thin lens is illustrated. All parallel rays or photons with the same emission angle $\theta_{x,y}$ are focussed to a common point on the detector plane $\rho_d(x, y)$ provided the detector is positioned at the back focal plane of the lens. In this way, the DR source is effectively shifted to infinity and may be considered a point source such that the DR spot in the detector plane is the angular distribution [40].

To avoid distortions to the DR distribution the lens radius must be sufficiently large. Firstly, the lens must be larger than the radiation source size to ensure that distortions do not occur due to diffraction of the photons from the source tails. Secondly, each elementary source contributing to the radiation source spot size emits a cone with divergence of order γ^{-1}.

In order to suppress the prewave zone without producing distortions to the DR angular distribution the lens must be considered infinite by satisfying the condition,

$$R_l \gg \frac{l}{\gamma} + \frac{\gamma\lambda}{2\pi}, \tag{2.6}$$

where l is the distance from the target to the lens and R_l is the lens radius. In Equation 2.6 the first term describes the DR spot size increasing with distance from the target and the second term describes the radiation source spot size i.e. the effective electric field radius r_E [40].

2.4 DR from a Single-Edge Target

In Figure 2.4 the Cartesian and mirror reflection direction geometries of DR production from a half-plane target are shown. The mirror reflection geometry is now the convention used for a simpler understanding of DR emission where θ_x and θ_y are the radiation angles measured from the mirror reflection direction [11].

In most cases especially for electron beams, the opening angles of the DR $\Delta\theta_{x,y}$, given the ultra-relativistic approximation ($\gamma \gg 1$) [39] are on the order of

$$\Delta\theta_{x,y} \sim \gamma^{-1} \ll 1. \tag{2.7}$$

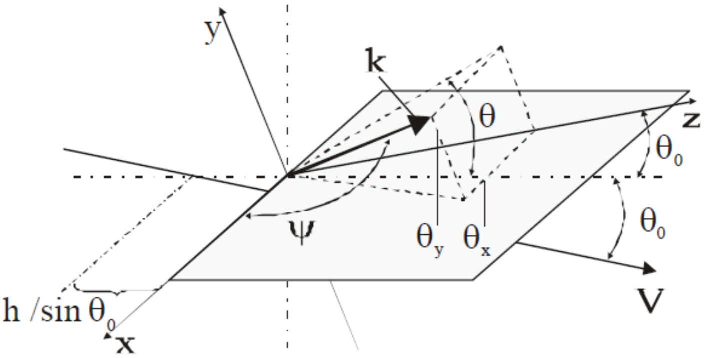

FIGURE 2.4: DR emission from a half-plane [11].

The DR angular distribution from a half-plane may then be written as

$$\frac{d^2W_{DR}(h)}{d\omega d\Omega} = \frac{\alpha}{4\pi^2}\exp\left(-\frac{\omega}{\omega_c}\sqrt{1+\gamma^2\theta_x^2}\right)\frac{\gamma^{-2}+2\theta_x^2}{(\gamma^{-2}+\theta_x^2)(\gamma^{-2}+\theta_x^2+\theta_y^2)}, \tag{2.8}$$

where $\alpha = e^2/(\hbar c) \sim 1/137$ is the fine structure constant, e is the elementary charge and $\hbar$ is the reduced Planck constant. The radiation frequency is $\omega = 2\pi/\lambda$ with characteristic frequency $\omega_c = \gamma/2h$ where h is the impact parameter [39].

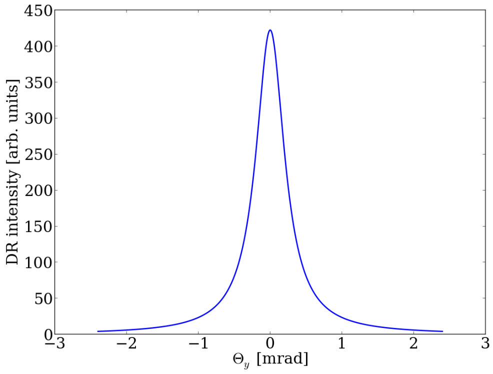

FIGURE 2.5: Diffraction radiation angular distribution calculated using Equation 2.8 where $\gamma = 4110$, $h = 0.26$ mm, $\theta_x = 0$ and $\lambda = 400$ nm.

In Figure 2.5 it is seen that for a half-plane target there is a single maximum in the DR angular distribution. This maximum occurs at $\theta_x = \theta_y = 0$ and has the characteristic angular width of order γ^{-1}[11]. In this case Equation 2.8 reduces to

$$\frac{d^2W_{DR}(h)}{d\omega d\Omega} = \frac{\gamma^2\alpha}{4\pi^2}\exp\left(-\frac{\omega}{\omega_c}\right). \tag{2.9}$$

2.5 DR from a slit

The spectral angular DR distribution for a single electron passing between two semi-planes is given by

$$\frac{d^2W_{DR}^{slit}}{d\omega d\Omega} = \frac{e^2\gamma^2}{2\pi^2}\frac{\exp\left(-\frac{2\pi a\sin\theta_0}{\gamma\lambda}\sqrt{1+t_x^2}\right)}{(1+t_x^2+t_y^2)(1+t_x^2)} \times \left[(1+2t_x^2)\cosh\left(\frac{4\pi a_x}{\gamma\lambda}\sqrt{1+t_x^2}\right) - \cos\left(\frac{2\pi a\sin\theta_0}{\gamma\lambda}t_y + 2\psi\right)\right], \qquad (2.10)$$

where a is the slit size, $-a/2 < a_x < a/2$ is the offset of the electron with respect to the slit centre in the plane perpendicular to the particle trajectory, θ_0 is the target tilt angle with respect to the incoming electron trajectory, e is the elementary charge constant, γ is the Lorentz factor and λ is the DR wavelength. In Eq.(2.10) new more convenient variables have also been introduced: $t_x = \gamma\theta_x$, $t_y = \gamma\theta_y$ and $\psi = \arctan\left(\frac{t_y}{\sqrt{1+t_x^2}}\right)$ where $\theta_{x,y}$ are the radiation angles measured from the mirror reflection direction [11].

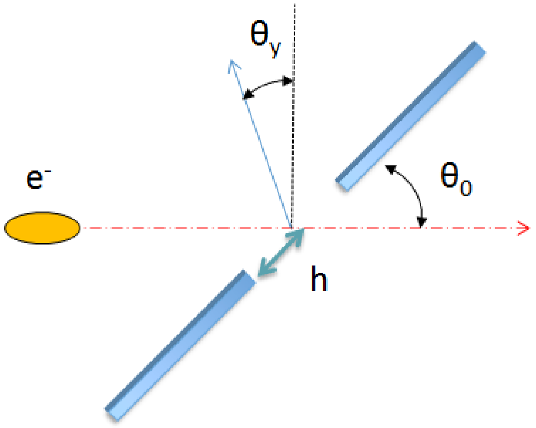

Figure 2.6: Schematic of DR from a slit.

In Figure 2.7 it is seen that the DR intensity reaches a maximum in the diffraction plane ($t_x = 0$) at $t_y \sim \pm 1$ [11].

Generally, DR intensity exponentially decreases as a function of aperture size. Reducing the target aperture size increases the number of atoms of the target material within the effective electric field radius r_E. This results in a higher yield of photons emitted and is one way in which the DR signal can be increased above background.

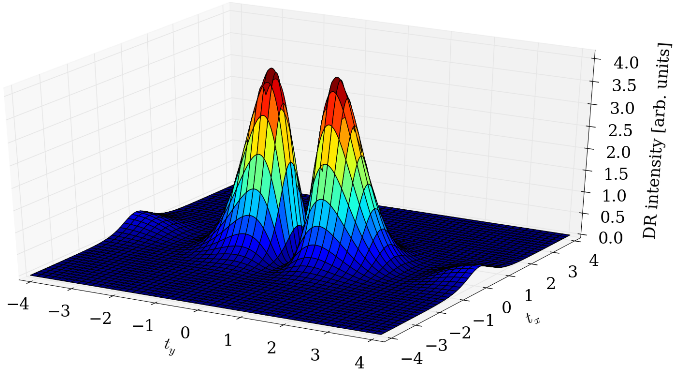

FIGURE 2.7: Diffraction radiation angular distribution calculated using Equation 2.10 where $\gamma = 4.11 \times 10^3$, $a = 0.5$ mm, $\lambda = 400$ nm and $a_x = 0$.

2.6 Optical Diffraction Radiation (ODR) model and the Beam Size Effect

The author of [36] has shown that the vertical polarisation component is sensitive to beam size. It is assumed that electron beam has a Gaussian distribution described by

$$G(\overline{a_x}, \sigma_y) = \frac{1}{\sqrt{2\pi\sigma_y^2}} \exp\left[-\frac{(\overline{a_x} - a_x)^2}{2\sigma_y^2}\right], \tag{2.11}$$

where σ_y is the rms vertical beam size, a is the target aperture size, $\overline{a_x}$ is the offset of the beam centre with respect to the slit centre and a_x is the offset of each electron of the beam with respect to the slit centre [11].

In [42], the expression for the ODR vertical polarisation component convoluted with a Gaussian distribution is

$$\begin{aligned}\frac{d^2W_y^{slit}}{d\omega d\Omega} = {} & \frac{\alpha\gamma^2}{2\pi^2} \frac{\exp\left(-\frac{2\pi a \sin\theta_0}{\gamma\lambda}\sqrt{1+t_x^2}\right)}{1+t_x^2+t_y^2} \\ & \times \left\{\exp\left[\frac{8\pi^2\sigma_y^2}{\lambda^2\gamma^2}(1+t_x^2)\right]\cosh\left[\frac{4\pi\overline{a_x}}{\gamma\lambda}\sqrt{1+t_x^2}\right]\right. \\ & \left. - \cos\left[\frac{2\pi a \sin\theta_0}{\gamma\lambda} t_y + 2\psi\right]\right\},\end{aligned} \tag{2.12}$$

where $t_{x,y} = \gamma\theta_{x,y}$ where $\theta_{x,y}$ are the radiation angles measured from the mirror reflection direction, σ_y is the rms vertical beam size, a is the target aperture size, $\overline{a_x}$ is the offset of the beam centre with respect to the slit centre and $\psi = \arctan\left[\frac{t_y}{\sqrt{1+t_x^2}}\right]$. This model is applicable when the TR contribution from the tails of the Gaussian distribution scraping the target is negligible i.e. approximately $a \geq 4\sigma_y$.

2.6.1 Projected Vertical Polarisation Component (PVPC)

The projected vertical polarisation component (PVPC) is a technique which takes the vertical (y) projection of the 3-dimensional (θ_x, θ_y, intensity) DR angular distribution. The y-projection is obtained by integrating over the horizontal angle θ_x as shown in plots (a) and (b) of Figure 2.8.

The visibility (I_{min}/I_{max}) of the y-projection is sensitive to the beam size of the electron beam and may be measured as shown in plot (b) of Figure 2.8 [42]. The maximum and minimum intensities of the DR angular distribution must be measured accurately. Measuring the maximum intensity (I_{max}) is straightforward ensuring the detector is not saturated, however the minimum intensity (I_{min} at $t_y = 0$) measurement may be limited by background photons. It is also necessary that I_{min} at $t_y = 0$ is above the camera noise.

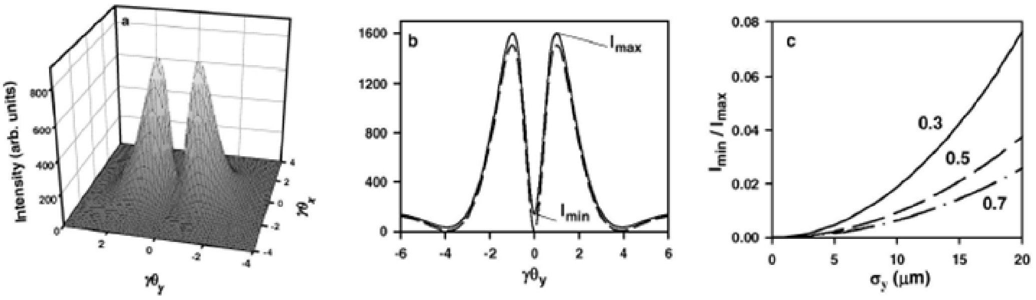

FIGURE 2.8: A summary of the steps performed in the PVPC technique for beam size measurement [33].

In Figure 2.8, plot (c) shows how the visibility curves at observation wavelengths of 0.3, 0.5 and 0.7 μm, may be obtained from multiple DR angular distribution images over a range of transverse beam sizes. Here is it seen that the sensitivity to beam size improves at shorter wavelengths as the change in visibility per micron change in beam size is greater i.e. the gradient of the visibility curve between different beam sizes is steeper.

Since the vertical projection is used rather that a single line profile, the PVPC method collects more DR photons emitted from the target. In turn this improves the sensitivity to beam size since the minimum intensity of the DR angular distribution is further displaced from zero above background.

2.6.2 ODR Model Analysis

Using Equation 2.12, the DR angular distributions with $t_x = 0$ at different wavelengths, target aperture sizes and beam sizes were obtained. In Figure 2.9 the DR angular distributions for 200 nm and 400 nm using a target aperture $a = 0.5$ mm and beam energy $E = 2.1$ GeV at beam sizes of $\sigma_y = 0\ \mu$m and 50 μm are shown. From these line profiles it is seen that for a given target aperture of 0.5 mm the number of fringes is approximately doubled at $\lambda = 200$ nm compared with $\lambda = 400$ nm. Although it should be noted that there is not a significant change in the separation distance between the central two lobes.

The overall DR intensity is dependent on the chosen observation wavelength. In Figure 2.9 the DR intensity at $\lambda = 400$ nm is approximately three times greater than that at 200 nm. It should be noted here that although the DR intensity in these simulations is measured in arbitrary units, the same scale is used for both plots in Figure 2.9 therefore the intensities may be compared. This intensity dependence on wavelength is in agreement with that predicted by the impact parameter given in Equation 2.4. In this case the characteristic DR intensity is expected at $\lambda = 382$ nm given $h = 0.25$ mm and $\gamma = 4110$.

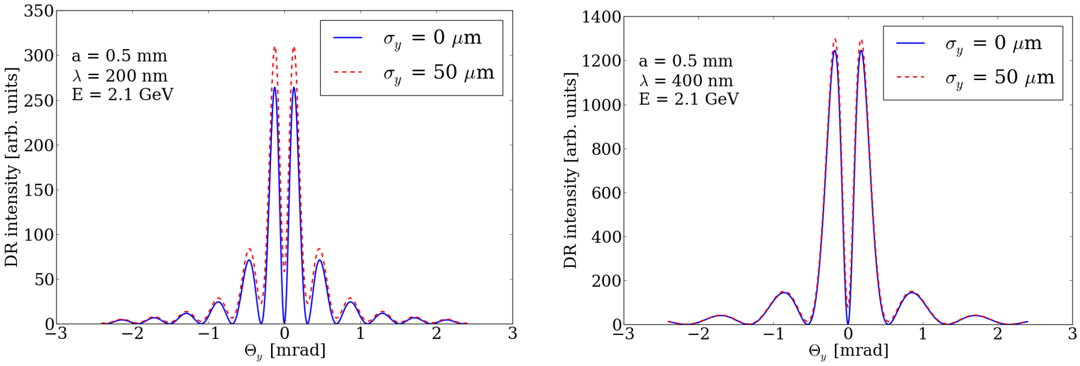

(a) (b)

Figure 2.9: DR angular distributions at $t_x = 0$ for $a = 0.5$ mm and $E = 2.1$ GeV: (a) comparison of $\sigma_y = 0\ \mu$m and 50 μm at 200 nm and (b) comparison of $\sigma_y = 0\ \mu$m and 50 μm at 400 nm.

In Figure 2.10 a comparison of the DR angular distributions for different target aperture sizes is presented. Here it is seen that the DR intensity scales inversely with aperture size. This is expected since using a smaller target aperture, more atoms of the target are polarised and hence emit DR for a given area around the passing electron. It is also observed that the number of fringes for the $a = 1.0$ mm target aperture is double that of the $a = 0.5$ mm given a 400 nm wavelength.

The visibility curves using the PVPC technique at different wavelengths are shown in Figure 2.11. It is observed that at shorter wavelengths, the gradient of the visibility

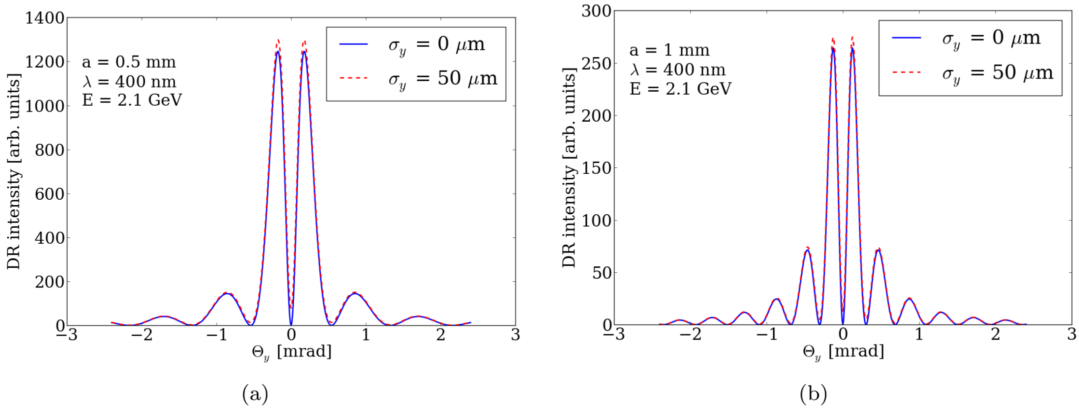

Figure 2.10: DR angular distributions at $t_x = 0$ for $\lambda = 400$ nm and $E = 2.1$ GeV: (a) comparison of $\sigma_y = 0$ μm and 50 μm at $a = 0.5$ m and (b) Comparison of $\sigma_y = 0$ μm and 50 μm at $a = 1.0$ mm.

curve is larger and therefore the sensitivity to beam size is greater. However there are additional complications in opting to use short wavelengths in the EUV or soft X-ray range. A more complicated optical system may be required. It may be necessary to keep the optical system under vacuum to prevent light absorption in air and also to carefully choose the materials of the various optical components.

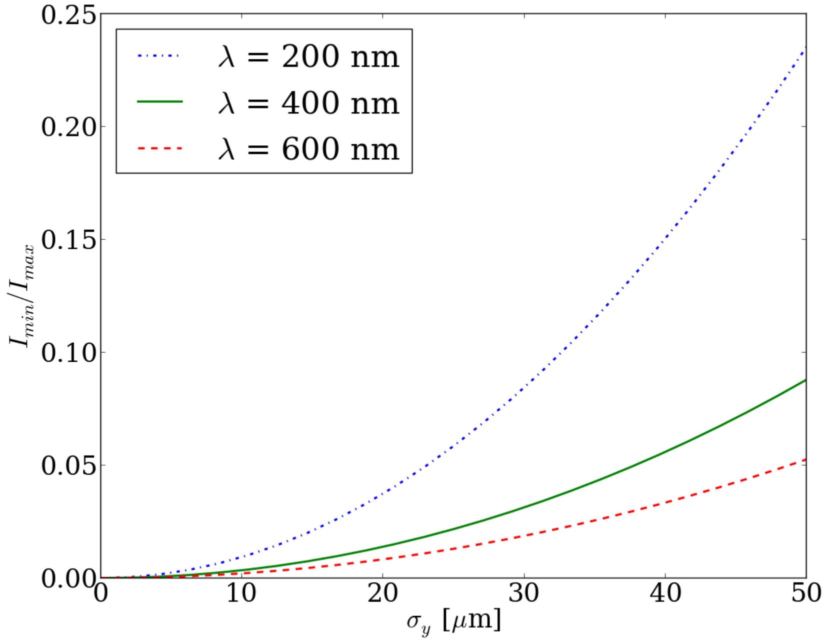

Figure 2.11: Visibility curves showing the increased beam size sensitivity at shorter wavelengths using a 2.1 GeV beam energy and 0.5 mm target aperture.

Increasing the beam energy increases the peak light intensity of the DR angular distribution. In Figure 2.12 it is seen that the sensitivity to beam size decreases with increasing beam energy. To compensate for the loss of beam size sensitivity at high energies, the monitor would need to operate at shorter wavelengths.

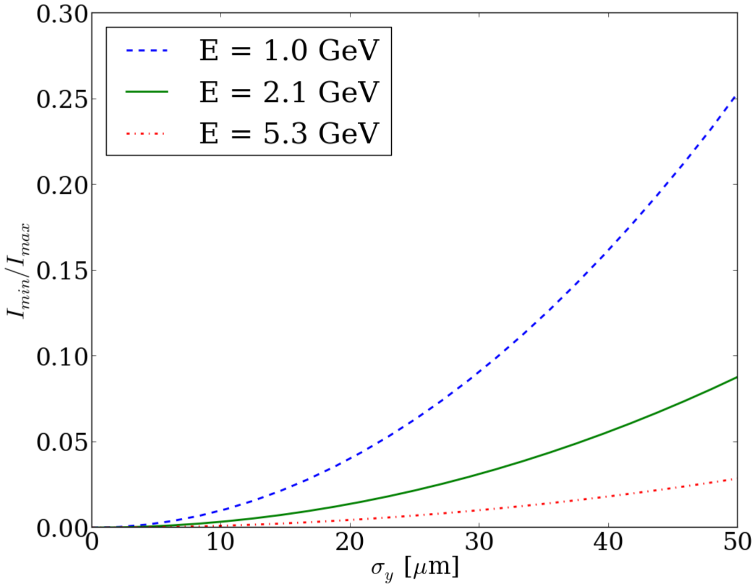

FIGURE 2.12: Visibility curves for beam size measurement using 400 nm wavelength and 0.5 mm target aperture for different beam energies.

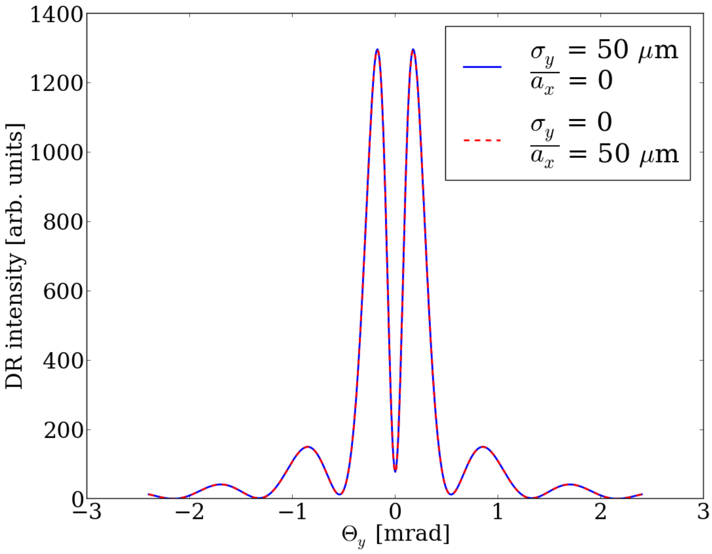

FIGURE 2.13: Angular distributions to show the ambiguity between beam size and beam offset with respect to the target centre.

One limitation of the ODR model and PVPC technique is the ambiguity in the angular distribution between vertical beam size and vertical beam offset with respect to the slit centre. In Figure 2.13 the angular distributions using Equation 2.12 are shown for the case of zero beam offset with 50 μm beam size and zero beam size with 50 μm beam offset. It is evident that these two cases produce the same DR angular distribution and cannot be distinguished. The other parameters in Figure 2.13 are $\lambda = 400$ nm, $\gamma = 4110$, $\theta_0 = 70°$, $\theta_x = 0$ and $a = 0.5$ mm.

Due to the ambiguity between beam size and beam position in the target aperture the beam position should ideally be simultaneously monitored using an independent BPM. This BPM would need submicron accuracy. Cavity BPMs could be employed for this purpose [43]. Imaging the ODR light intensity from both slit edges could be used to align the beam in the slit aperture. The position resolution of this measurement will increase with decreasing wavelength.

2.7 Optical Diffraction Radiation Interference (ODRI) model

Generally in DR experiments a two-slit setup is implemented where a mask is positioned upstream of the target to reduced unwanted background due to SR. However it must not be overlooked that the mask is in effect a secondary target and will also emit DR as the beam passes through the aperture. It is known that FDR produced by the mask interferes with BDR emitted by the target. Interference occurs between DR emitted by the mask and target because the separation between the mask and target is less than the coherence length.

The radiation formation length L_f or coherence length is defined as the region of the charged particle trajectory where interference between emitted DR photons will occur and may be represented by

$$L_f = \frac{\lambda}{\pi} \frac{1}{(\gamma^{-2} + \theta_x^2 + \theta_y^2)}, \tag{2.13}$$

where γ is the Lorentz factor, λ is the wavelength and $\theta_{x,y}$ are the observation angles [39]. For example, if an electron emits two photons at a distance comparable to or smaller than the radiation formation length, those two photons interfere. The photon and electron fields will only be completely separated when the distance along the electron trajectory from the radiation source (target) to the electron is much greater than the radiation formation length [40].

The reader should make note that although the radiation formation length and the far-field condition are described by similar relations they determine completely different physical parameters [11].

The ODR model only considers DR emitted from the target. This model is reasonable provided the interference between the mask and target is very small. When this condition is not satisfied, the FDR from the mask must not be ignored and the Optical Diffraction Radiation Interference (ODRI) model should be applied [12]. The reader should note that here for consistency to the papers referenced the nomenclature by the authors of [12] is given.

Similarly to the ODR model, the first step of the ODRI model considers the field component at the target only. The electric field component with polarisation normal to the slit edge is taken as the vertical polarisation field component. The vertical polarisation field component for a single charged particle passing through a slit is represented in the form

$$E_y = \frac{ie}{4\pi^2 c}\left\{\frac{\exp[-(\frac{a}{2}+a_x)(f-ik_y)]}{f-ik_y} - \frac{\exp[-(\frac{a}{2}-a_x)(f+ik_y)]}{f+ik_y}\right\}, \tag{2.14}$$

with parameters:

$$\begin{aligned} k &= \tfrac{2\pi}{\lambda}, \\ k_x &= k\sin\theta\cos\phi \approx k\theta_x, \\ k_y &= k\sin\theta\sin\phi \approx k\theta_y, \\ \eta &= \tfrac{k}{\beta\gamma}, \\ f &= \sqrt{k_x^2+\eta^2}. \end{aligned}$$

where γ is the Lorentz factor, λ is the wavelength, $\theta_{x,y}$ are the observation angles, e is the elementary charge, c is the speed of light constant, a is the target aperture size, a_x is the position of the charged particle in the aperture and $k_{x,y}$ are the components of the wavenumber k [12]. The DR intensity is obtained from the field component using the relation in Equation 2.3 where for simplicity the constants have been omitted.

The polar angles θ and ϕ are defined in Figure 2.14. To observe the vertical angular distribution $\phi = \pi/2$ and a range of θ is chosen. Since the vertical angular distribution in then obtained, the observation angle *theta* may be replaced by θ_y.

In the two-slit setup, Equation 2.14 must be modified to include the phase difference between the FDR and BDR amplitudes due to the difference in speed between the charged particle and radiation. This results in an emission delay of BDR at the second target with respect to the FDR wave front emitted at the mask. Including these effects and neglecting the constant coefficient the resulting vertical electric field component produced by two perfectly centred slits is given by

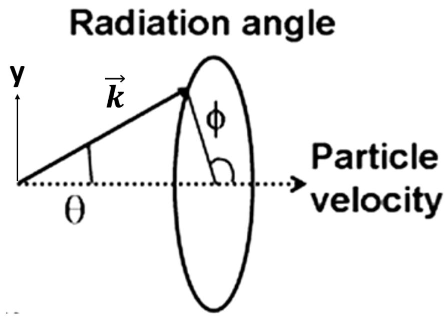

FIGURE 2.14: Definition of the coordinate system used in the ODRI model- modified from [12].

$$E_y = \frac{ie}{4\pi^2 c}\left[\left\{\frac{\exp[-(\frac{a_1}{2}+a_x)(f-ik_y)]}{f-ik_y} - \frac{\exp[-(\frac{a_1}{2}-a_x)(f+ik_y)]}{f+ik_y}\right\}\right.$$
$$\left. - \exp(i\Phi_0)\left\{\frac{\exp[-(\frac{a_2}{2}+a_x)(f-ik_y)]}{f-ik_y} - \frac{\exp[-(\frac{a_2}{2}-a_x)(f+ik_y)]}{f+ik_y}\right\}\right], \quad (2.15)$$

where $\Phi_0 = \frac{2\pi d}{\beta\lambda}(1-\beta\cos\theta)$, a_1 is the mask aperture size, a_2 is the target aperture size and d is the distance between the mask and target [12].

For a realistic BDR model, one must also take into account the non-coplanarity between the half-planes of the target slit. A non-coplanarity of a few tens of nanometres can produce a significant variation in the DR angular distribution. Therefore the phase difference $\Phi_1 = \frac{4\sqrt{2}\pi\Delta}{\lambda}$ is introduced as shown in

$$E_y = \frac{ie}{4\pi^2 c}\left\{\left[\frac{\exp[-(\frac{a_1}{2}+a_x-\delta)(f-ik_y)]}{f-ik_y} - \exp(i\Phi_1)\frac{\exp[-(\frac{a_1}{2}-a_x+\delta)(f+ik_y)]}{f+ik_y}\right]\right.$$
$$\left. - \exp(i\Phi_0)\left[\frac{\exp[-(\frac{a_2}{2}+a_x)(f-ik_y)]}{f-ik_y} - \exp(i\Phi_1)\frac{\exp[-(\frac{a_2}{2}-a_x)(f+ik_y)]}{f+ik_y}\right]\right\}, \quad (2.16)$$

where Δ is the coplanarity of the target tines in the longitudinal direction as shown in Figure 2.15 [12].

In Figure 2.16 the angular distributions for different non-coplanarities between the upper and lower semi-planes of the target are shown. To prevent significant distortion of the DR angular distribution the non-coplanarity must less than a fraction of the observation wavelength i.e. $\Delta < 0.1\lambda$.

To fit real data an additional parameter δ is included in Equation 2.16 to account for the small vertical offset between the slit centres of the mask and target. This misalignment parameter is often referred to as the non-linearity of the slits [12]. By introducing an

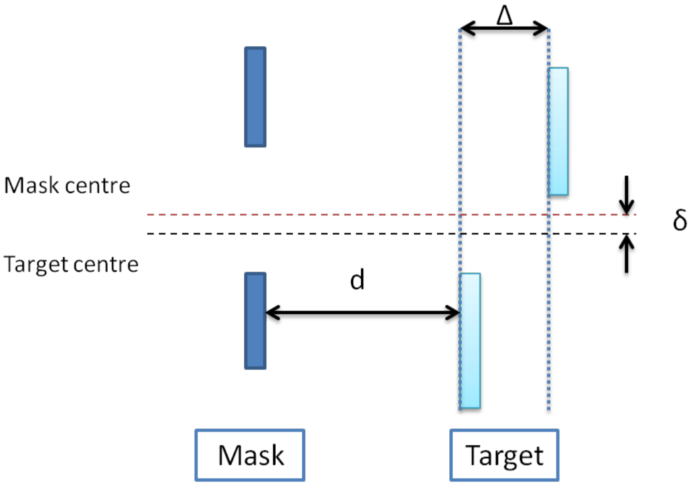

Figure 2.15: A schematic illustrating the additional parameters of the ODRI model: coplanarity Δ, mask and target non-linearity δ and distance between the mask and target d.

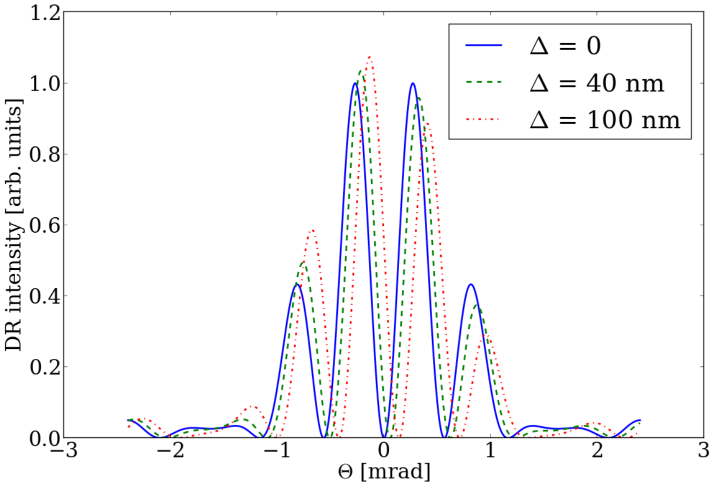

Figure 2.16: The effect of target coplanarity on the DR angular distribution for a single electron passing through the target centre where $a_2 = 1.0$ mm, $\lambda = 400$ nm and $E = 2.1$ GeV.

offset between the mask and target centres, the cancellation of the overall DR intensity due to interference can be suppressed.

The ODRI model with vertical field given in Equation 2.16 makes the assumption that all FDR emitted from the mask is completely reflected by the target. In reality, this is not the case since the target is not a screen but has an aperture through which some FDR photons must pass through. Therefore part of the FDR distribution will be diffracted through the target slits. However, provided the mask is larger than the target aperture this effect will be small.

When the distance between the mask and target is much shorter than the coherence length L_f, the forward and backward DR amplitudes sum up with opposite sign. If the mask and target have the same aperture size this will result in an almost complete cancellation of the total intensity due to the intrinsic phase difference of π between FDR and BDR [12].

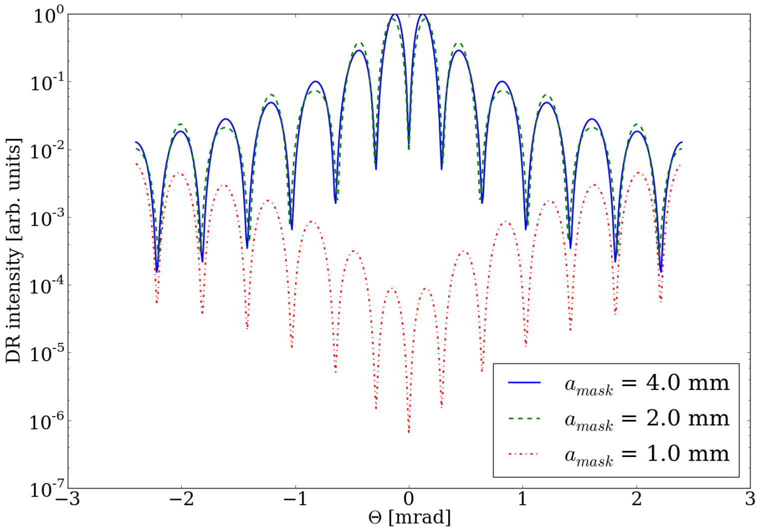

FIGURE 2.17: Comparison of the interference effect given a 1.0 mm target aperture for 1.0, 2.0 and 4.0 mm mask apertures for 400 nm wavelength, 2.1 GeV beam energy and 25 μm beam size. The 2.0 and 4.0 mm mask aperture distributions are overlaid with one another showing very little difference. However a significant difference is observed between the 1.0 and 2.0 mm mask aperture distributions.

In Figure 2.17 the significance of the destructive interference effect is compared for different mask sizes. It is seen that the angular distributions corresponding to the 2.0 and 4.0 mm mask apertures are overlaid with one another. Therefore roughly the same level of interference is observed when using a 2.0 mm mask paired with 1.0 mm target or alternatively using a 4.0 mm mask paired with 1.0 mm target. A significant reduction in intensity is observed when the target and mask are the same size. This is clear when comparing the angular distributions corresponding to 1.0 and 4.0 mm mask apertures given a 1.0 mm target aperture size.

Here for simplicity we summarise the degree of interference expected given the target a_2 and mask a_1 apertures:

- $a_1 \geq 4a_2$ negligible interference i.e. the ODR model would still be applicable.
- $2a_2 \leq a_1 < 4a_2$ substantial interference i.e. the ODR model is no longer suitable.
- $a_1 \approx a_2$ complete destructive interference i.e. zero light intensity.

Typically the characteristic features of the angular distribution indicating non-negligible interference effects are observed as a reduction of the peak intensity of the central lobes and enhancement of the adjacent side fringes. Using Equation 2.15 these features are illustrated in Figure 2.18 where the ODR and ODRI conditions are compared.

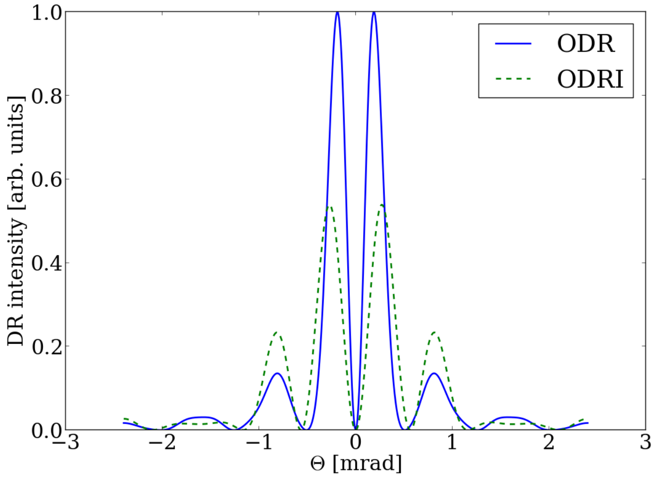

FIGURE 2.18: Comparison of ODR and ODRI for a 0.5 mm target aperture: 400 nm wavelength, 2.1 GeV, $a_2 = 0.5$ mm and $a_1 = 2.0$ and 1.0 mm for the ODR and ODRI cases respectively..

In Figure 2.18 it is seen that the peak intensity of the central lobes for the ODR distribution is approximately double that of the central lobes of the ODRI distribution. Conversely, comparison of the side fringes show that the peak intensity of the ODRI distribution is twice that of the ODR distribution. It is also seen that the central minimum of the ODR and ODRI distributions are aligned, however the other minima are slightly offset. All of the above differences are due to the interference effect, the reader should refer to [12] for further understanding.

From these observations, it is found that the interference effect can be useful since using a smaller mask aperture reduces the contribution of SR to the measurements and the increased visibility of the side peaks provides more data points for the fitting procedure [12].

The Equations 2.14, 2.15 and 2.16 only consider the DR angular distribution produced for a single charged particle traversing a single slit or multiple slits. To obtain the DR angular distribution for a real beam using this model, the effect of the vertical angular spread and the vertical beam size are included by using a Monte Carlo approach. The summation of intensity distributions given by each electron at a specified position and divergence in the target aperture obeying a Gaussian distributed beam profile is calculated. The divergence is included in Equation 2.16 using the modification $\theta \to (\theta + \delta\theta)$.

Unlike the ambiguity between beam size and beam offset in the single-slit ODR scenario, in the case of ODRI these two parameters can be simultaneously determined provided the slit centres of the mask and target are misaligned by a non-linearity offset. In Figure 2.19 the breaking of the ambiguity between beam size and beam offset in the target aperture is demonstrated using Equation 2.16 and a non-linearity offset of 0.1 mm between the mask and target. Angular distributions are shown for the case of zero beam offset

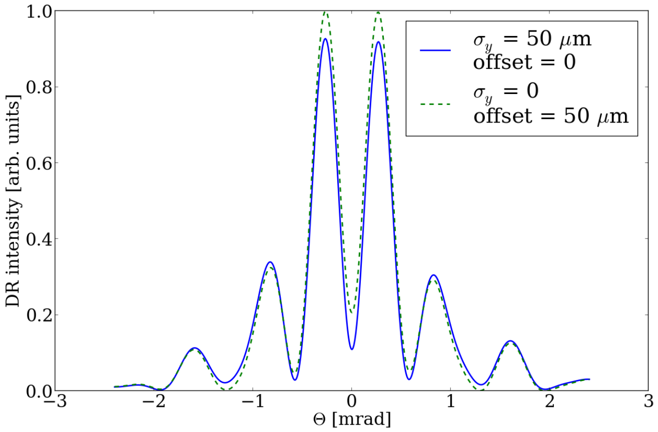

FIGURE 2.19: Breaking the ambiguity in the angular distributions by using a 0.1 mm misalignment between the target and mask aperture centres for the case of zero beam offset with 50 μm beam size and zero beam size with 50 μm beam offset where $\lambda =$ 400 nm, $E = 2.1$ GeV, $a_2 = 0.5$ mm and $a_1 = 1.0$ mm.

with 50 μm beam size and zero beam size with 50 μm beam offset where $\lambda = 400$ nm, $E = 2.1$ GeV, $a_2 = 0.5$ mm and $a_1 = 1.0$ mm. Due to the misalignment of the mask and target slit centres, the angular distributions are no longer overlaid with one another which would be the case if the ambiguity between beam size and beam offset was still present. Instead it is seen that the central lobes and visibilities for the beam size and beam offset cases are different and can therefore be identified.

2.8 Target Imaging

As described in the previous section, the transverse beam size measurement is determined from the angular distribution of DR. However, the strengths and weaknesses of the various models should be considered.

The ODR model where only the DR emitted from the target is considered does not include interference effects between forward and backward DR from the mask and target respectively. Therefore this approach should only be used for data analysis when the mask aperture is considerably greater than the target aperture. In this case the interference effects are negligible.

The main drawback of this and other similar models is that both the beam size and beam divergence contribute ambiguously to the visibility (I_{min}/I_{max}) of the angular distribution that is observed. On linear machines this drawback can more easily be avoided. However on a circular machine, the location of the DR monitor should avoid the beam waists if this model is to be employed effectively for beam size measurement.

The ambiguities between beam size, beam divergence and beam offset can be broken by consideration of the interference effects as in the case of the ODRI model. Thus solving the main drawback of beam size determination through angular distribution analysis. However it should be noted that, both the ODR and ODRI models make the assumption of a Gaussian distribution for the electron beam profile and hence only predict the rms beam size instead of the detailed beam profile which may be obtained by direct imaging [44].

The theory and feasibility of direct imaging of the target surface to obtain more detailed beam profiles is investigated in [44]. The fields in the image plane for DR generated by a single electron passing through a rectangular slit target is given in Equation 2.17a (horizontal component) and Equation 2.17b (vertical component).

$$\begin{aligned}
E^i_{x_i} = {}& \frac{ie}{2\pi\lambda M v}\int \mathrm{d}\theta \mathrm{d}\phi_l \frac{\theta^2\cos\phi_l}{\sqrt{(\theta\cos\phi_l)^2+\gamma^{-2}}}\exp\left[-ik\frac{x_i\theta\cos\phi_l+y_i\theta\sin\phi_l}{M}\right] \\
&\times\left[\frac{e^{-kt_1(\sqrt{(\theta\cos\phi_l)^2+\gamma^{-2}}-i\theta\sin\phi_l)}}{\sqrt{(\theta\cos\phi_l)^2+\gamma^{-2}}-i\theta\sin\phi_l}+\frac{e^{-kt_2(\sqrt{(\theta\cos\phi_l)^2+\gamma^{-2}}+i\theta\sin\phi_l)}}{\sqrt{(\theta\cos\phi_l)^2+\gamma^{-2}}+i\theta\sin\phi_l}\right] \qquad \text{(2.17a)} \\
E^i_{y_i} = {}& \frac{ie}{2\pi\lambda M v}\int \mathrm{d}\theta \mathrm{d}\phi_l \theta\exp\left[-ik\frac{x_i\theta\cos\phi_l+y_i\theta\sin\phi_l}{M}\right] \\
&\times\left[\frac{e^{-kt_1(\sqrt{(\theta\cos\phi_l)^2+\gamma^{-2}}-i\theta\sin\phi_l)}}{\sqrt{(\theta\cos\phi_l)^2+\gamma^{-2}}-i\theta\sin\phi_l}-\frac{e^{-kt_2(\sqrt{(\theta\cos\phi_l)^2+\gamma^{-2}}+i\theta\sin\phi_l)}}{\sqrt{(\theta\cos\phi_l)^2+\gamma^{-2}}+i\theta\sin\phi_l}\right] \qquad \text{(2.17b)}
\end{aligned}$$

where M is the magnification factor, R_l is the lens radius, $D_{1,2}$ are the source-to-lens and lens-to-detector distances respectively, $\theta = R_l/D_1$ over the range $[0, \theta_m]$, θ_m is the maximum acceptance angle of the lens, x_i, y_i are the transverse positions on the detector plane, $v = c\sqrt{1-\gamma^2}$ is the electron velocity, c is the speed of light, γ is the Lorentz factor, λ is the wavelength, $k = 2\pi/\lambda$ is the wavenumber, ϕ_l is the polar angle in the lens plane and $t_{1,2}$ is the distance of the electron from the slit edges 1 and 2 respectively.

The subscripts s, l and i denote the source, lens and image planes as shown by the geometry in Figure 2.20.

In Figure 2.21, the point spread function (PSF) for the vertically polarised DR is shown with parameters: $\theta_m = 0.0636$, $k = 10.5 \times 10^6$ m^{-1}, $x_i = 0$, $M = -0.611$, $\gamma = 4110$, $\lambda = 600$ nm and $t_1 = t_2 = 0.25$ mm. For DR the PSF is the distribution emitted by a single electron. The intensity distribution is obtained using Equation 2.3, the constant term may be neglected since the intensity amplitude is in arbitrary units.

In order to model a beam rather than a single electron, a Monte Carlo approach can be used whereby the DR imaging distribution of the electron beam is the sum of the intensity distributions of each electron in the Gaussian-distributed beam. This method of modelling the Gaussian distributed beam is accurate but time-consuming when running code. An example of a Gaussian distributed beam profile using 10^5 electrons and 25 bins is shown in Figure 2.22(a).

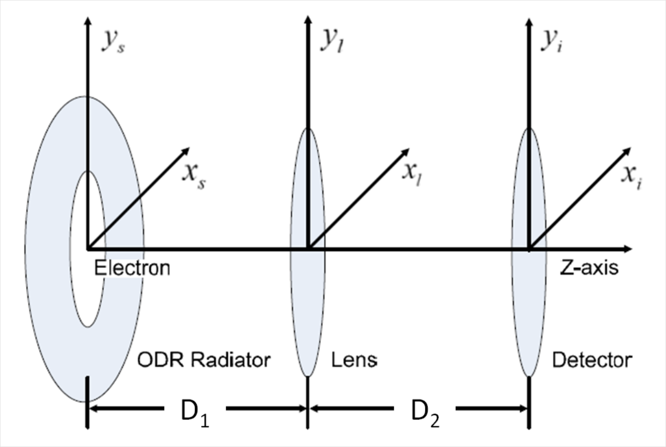

FIGURE 2.20: Geometry for imaging with DR from a circular aperture presented here to show the subscript notation for the source, lens and detector plans [44].

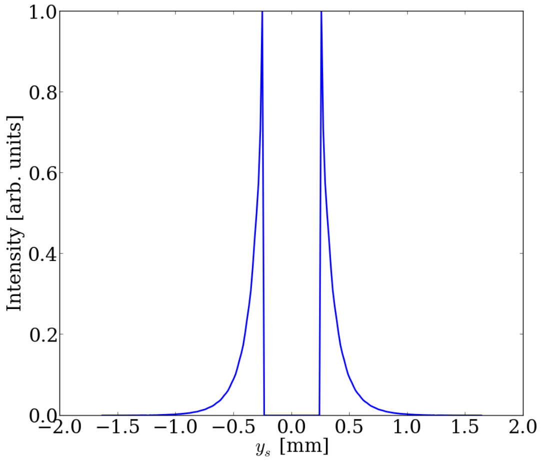

FIGURE 2.21: Target imaging point spread function (PSF) at $x_i = 0$ for a single electron with parameters: $\gamma = 4110$, $t_1 = t_2 = 0.25$ mm, $\lambda = 600$ nm, $\theta_m = 0.0636$, $k = 10.5 \times 10^6$ m^{-1} and $M = -0.611$.

Within the target imaging model the position of the slit edges variable relative to the fixed beam position according to $t_{1,2}$. Therefore for each bin position y_s, a shift term must be included such that a common coordinate system is used where the electron position is changed relative to the fixed slit edges. This is crucial for the intensity summation over the beam profile and errors will arise if care is not taken.

Although the Monte Carlo approach is time-consuming, unlike the angular distribution models it does allow for non-Gaussian electron beam profiles and poor beam quality. To reduce the runtime an approximation may be made by taking the sum of intensity distributions from a smaller sample of electrons and weighting them accordingly.

The target image line profile at $x_i = 0$ for the Gaussian distributed beam is shown in Figure 2.22 with parameters: $\theta_m = 0.0636$, $k = 10.5 \times 10^6$ m^{-1}, $x_i = 0$, $M = -0.611$, $\gamma = 4110$, $\lambda = 600$ nm and $t_1 = t_2 = 0.25$ mm. In this case the electron beam is centred in the target aperture $y_s = 0$ with rms beam size $\sigma_y = 17.6$ μm.

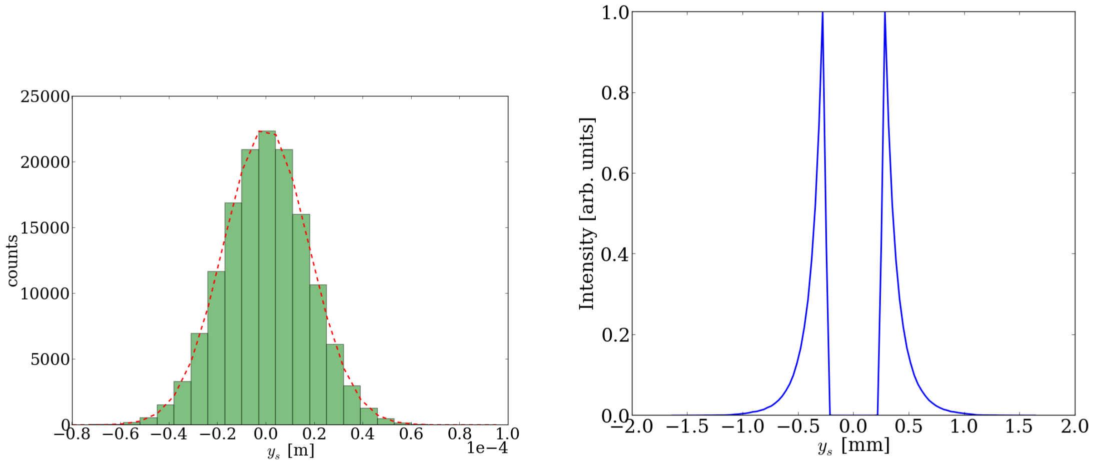

(a)

(b)

FIGURE 2.22: Gaussian distributed beam profile (a) and DR distribution on the target surface (b) using the Monte Carlo approach (green histogram) with the normal probability density function (dashed red line) for $\sigma_y = 17.6$ μm.

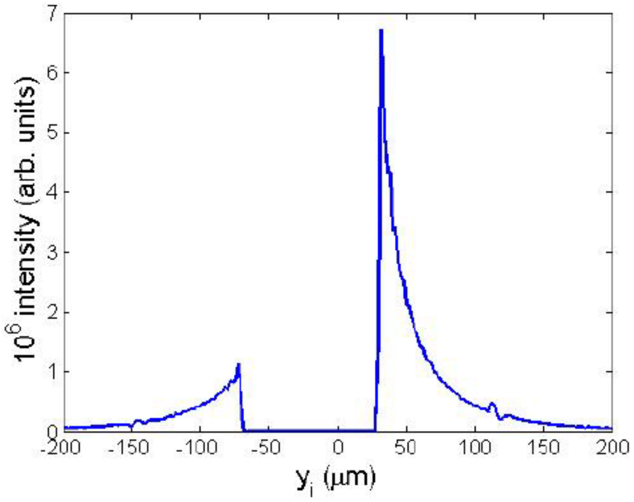

FIGURE 2.23: PSF at $x_i = 0$ for a single electron passing through a rectangular slit with 20 μm vertical offset relative to the slit centre with parameters: $t = 100$ μm, $t_1 = 30$ μm and $t_2 = 70$ μm [44].

In Figure 2.21 and Figure 2.22(b) it is seen that the DR signal decays exponentially from the target edge. This feature may be used to distinguish DR signal from background in target imaging. The intensity scales have been normalised in this case however as expected, the intensity distribution for a beam is much larger than that for a single electron.

The intensity distribution for a centred single electron or Gaussian beam is symmetric. An asymmetry of the shape and peak intensity on each slit edge indicates that the beam is not centred in the target aperture as shown in Figure 2.23. Therefore this property may be used as a diagnostic tool to monitor the beam position in the direction perpendicular to the slit edge i.e. to align the beam with the centre of the target aperture [44].

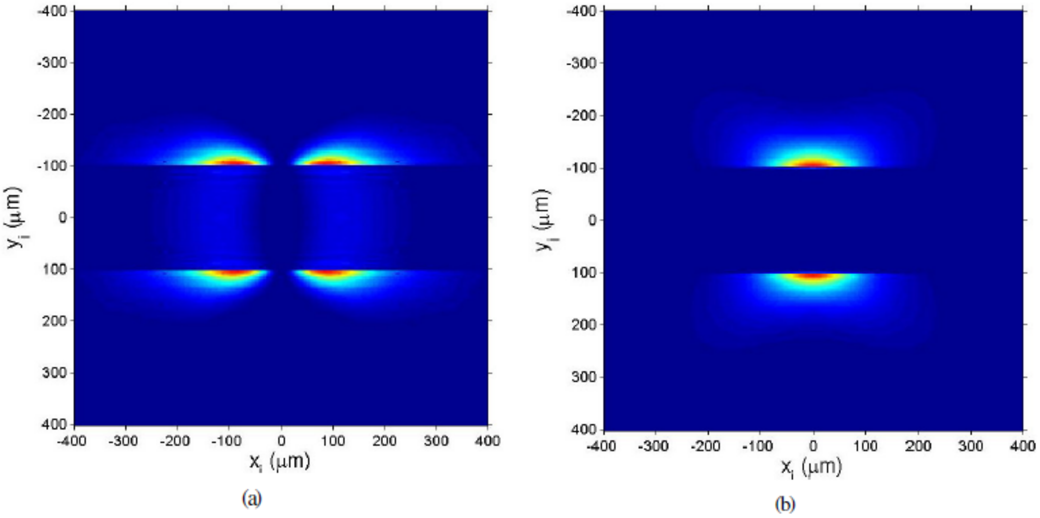

FIGURE 2.24: PSF of the DR from a rectangular slit for the horizontal (a) and vertical (b) components [44].

From [44] the horizontally and vertically polarised PSF are shown in Figure 2.24 for DR emitted from a rectangular slit. The intensity scales in these figures have been normalised to their maximum intensities respectively and are not scaled relative to each other.

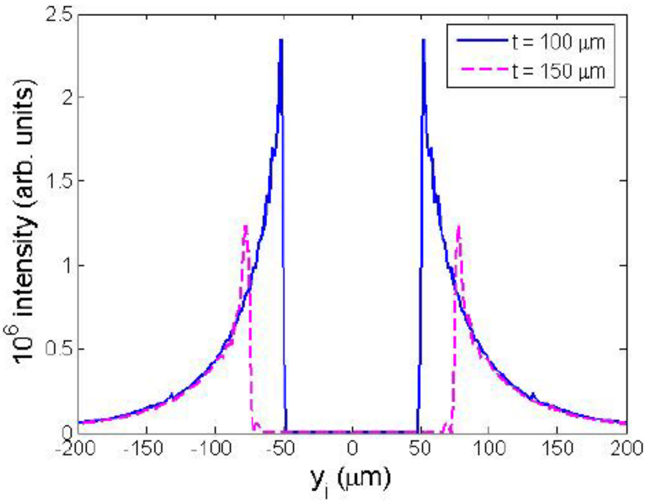

FIGURE 2.25: PSF at $x_i = 0$ for a single electron passing through a rectangular slit with 20 μm vertical offset relative to the slit centre [44].

The peak intensity of the vertical component is approximately 7 times greater than that of the horizontal component. Due to the orientation of the slit aperture, a greater proportion of the vertically polarised lobes is incident on the target surface in comparison to the horizontal polarisation field lobes. Generally for a given slit width, the ratio of the peak vertical component intensity to the peak horizontal intensity increases with the effective field radius $\gamma\lambda$ of the electron [44].

In Figure 2.25 the line profile at $x_i = 0$ for a single electron passing through various slit widths is presented. As the slit width is reduced, the DR image intensity increases. This property can be used to increase the DR signal relative to background. However on a circular machine a compromise must be made between DR signal optimisation, beam lifetime and the contribution of SR background.

Chapter 3

Experimental Setup

3.1 CesrTA

The Cornell Electron Storage Ring (CESR) was originally an electron-positron collider. In 2008 the central components of the of the CLEO detector and the superconducting low beta quadrupoles were removed from the CESR L0 straight [45]. The storage ring with beam parameters as shown in Table 3.1 was primarily reconfigured as a test accelerator (CesrTA [45]) for the investigation of beam physics for the International Linear Collider [46] damping rings. The CesrTA parameters of particular interest are summarised Table 3.2 and compared to those of CLIC.

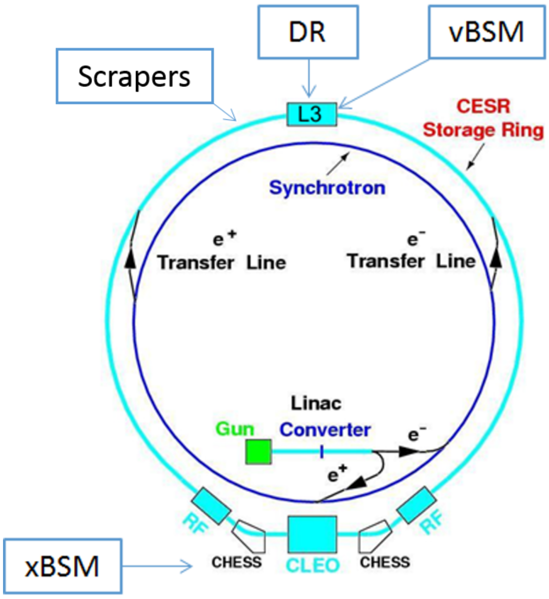

Figure 3.1: A modified figure showing the layout of CESR from [47].

The layout of CesrTA is shown in Figure 3.1. Electrons emitted from a heated filament are accelerated in a 30 m long linac. Positrons are produced by accelerating electrons

Table 3.1: Parameters of the Cornell Electron Storage Ring Test Accelerator (CESRTA) [9].

Parameter	**Value**
Circumference	768.4 m
Circulation time	2.563 μs
Circulation frequency	390.1 kHz
Beam energy	2.085 (1.5 - 5.3) GeV
Species	e^+ or e^-
RF frequency	500 MHz
Harmonic number	1281
Bunch spacing	≤ 4 ns
Bunch population	$0.1 - 10 \times 10^{10}$
Number of bunches/turn	≤ 45
Horizontal emittance	2.6 nm
Vertical emittance	≤ 10 pm
Longitudinal bunch size (rms)	10 - 15 mm
Horizontal bunch size (rms)	170 - 300 μm
Vertical bunch size (rms)	10 - 100 μm

Table 3.2: Phase 1 Experiment parameters for CesrTA (courtesy of M. Billing) and comparison with the CLIC damping ring complex [3].

	E (GeV)	σ_H **(μm)**	σ_V **(μm)**
CesrTA	2.1	320	$\sim$9.2
	5.3	2500	$\sim$65
CLIC	2.86	10-100	1-50

up to 140 MeV and colliding them with a tungsten plate at an intermediate point of the linac. A spray of electrons, positrons and X-rays emerge from this collision whereby the positrons are selected, focused, accelerated in the remaining length of the linac up to the 200 MeV final energy, and injected into the synchrotron [48].

The synchrotron accepts electrons (at 300 MeV) or positrons (150 to 200 MeV) from the linac. The circulating beams are accelerated to higher energies by cavities. After approximately 4000 turns around the ring (0.01 seconds), the beam reaches its maximum energy and is injected into the storage ring [48].

The storage ring CesrTA, with a circumference of 768 m, provides high energy $1.5 - 5.3$ GeV electron and positron beams. Here, the DR monitor can be baselined to measure a vertical beam size on the order of 10 μm. A circular machine allows the study of wakefields and synchrotron radiation (SR) associated with DR monitors. The applicability of DR monitors for machines other than CLIC such as the LHC which has a comparable Lorentz factor can also be investigated.

The DR experiment is located in the L3 straight section of the storage ring. This location was chosen to reduce the SR background from bending magnets upstream. Due to the access walkway along the beamline, it was necessary to position the DR instrumentation on the radial outside of the storage ring. An X-ray beam size monitor (xBSM) [49] is used to measure the vertical beam size σ_y and is located at the Cornell High Energy Synchrotron Source (CHESS) station. The visible beam size monitor (vBSM) [50] is used to measure the horizontal beam size σ_x and is located in the L3 straight section approximately 10 m upstream of the DR target. For beam size measurements at the DR target location, measurements from the xBSM and vBSM are scaled using the Beta function.

3.1.1 X-ray Beam Size Monitor (xBSM)

The X-ray Beam Size Monitor (xBSM) is a SR based instrument that provides high resolution vertical beam size measurements. This instrument is capable of measuring individual bunches on the order of 10 μm [51] on a turn-by-turn. At each of the two CHESS experimental areas labelled in Figure 3.1 an xBSM has been installed allowing measurements for both electron and positron beams [49].

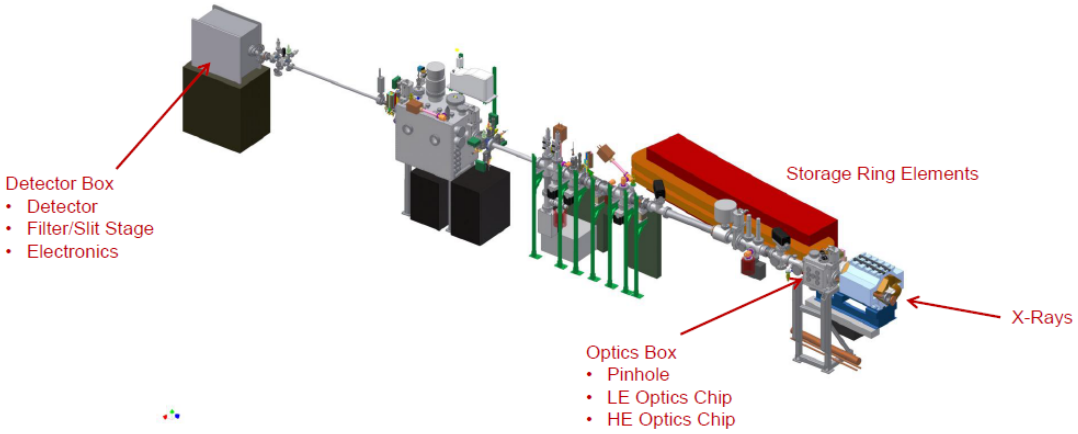

FIGURE 3.2: Layout of the xBSM [49].

As shown in Figure 3.2 each xBSM setup has its own SR source, in-vacuum optical system and detector and data acquisition system. The x-ray source is a dipole magnet in the storage ring. This hard-bend magnet at the xBSM source point has a bending radius $\rho = 31.65$ m. For CesrTA operations at 2.1 GeV beam energy, the critical energy of the SR is 0.634 keV [49, 9].

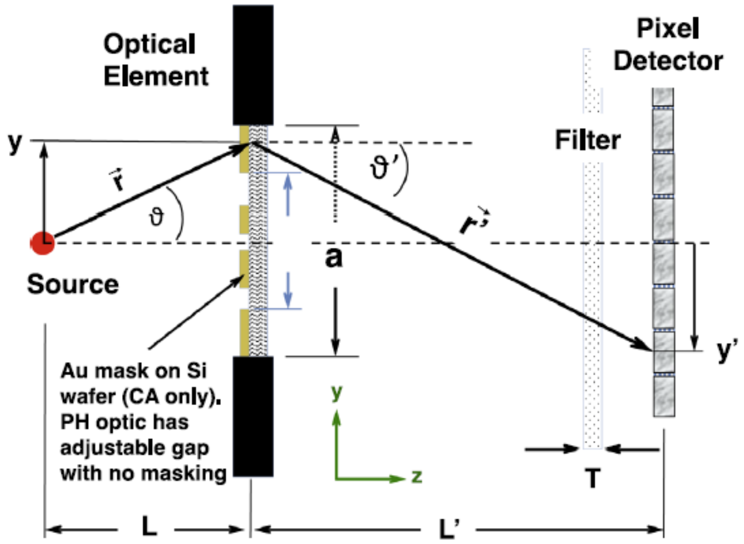

FIGURE 3.3: Simplified schematic of the xBSM layout where a is the total vertical extent of partial transmission through the mask material, a' is the vertical extent of slits in the mask, L is the source to optical element distance and L' is the optical element to detector distance. for general operation a pinhole optical element is used [9].

TABLE 3.3: Geometrical parameters defining the CesrTA xBSM beamlines [9].

Parameter	**e$^-$ beamline**	**e$^+$ beamline**
L	4356.5 ± 3.9 mm	4485.2 ± 4.0 mm
L'	10621.1 ± 1.0 mm	10011.7 ± 1.0 mm
$M = L'/L$	2.4380 ± 0.0022	2.2322 ± 0.0020
a'	$\approx$ 50 - 300 μm	Same as e$^-$
a	$\approx$ 50 - 1000 μm	Same as e$^-$
$2\sigma_{max} = a'/L$	11 - 69 μrad	11 - 67 μrad

An in-vacuum optical system is implemented by installing all of the optical components inside a continuous vacuum vessel from the x-ray source to the detector. This establishes a "windowless" transmission path which reduces losses to the photon yield through x-ray absorption. The geometry of the xBSM optics is shown in Figure 3.3 with parameters summarised in Table 3.3. The length of the electron line from source to detector is approximately 15 m resulting in an optical magnification of 2.23 [51].

During the testing of the DR monitor at 2 GeV beam energies the xBSM is operated as a pinhole camera. A vertically limiting slit consisting of a set of tungsten blades is inserted in the optical path. The opaque blades of the slit are adjustable such that the slit height can be optimised for different particle beam energies.

X-ray photons are detected by a vertical linear array of 32 InGaAs diodes. The diodes have a pitch of 50 μm and horizontal width of 400 μm. The thickness of the InGaAS layer is 3.5 μm and absorbs 73% of photons at 2.5 keV.

Each of the 32 diodes has its own independent data acquisition channel which is synchronised to the storage ring using a 24 MHz instrumentation clock. The clock comes from the CESR master oscillator and includes the triggers and turn markers. Turn-by-turn, individual bunch images can be acquired by the sub-nanosecond detector response time.

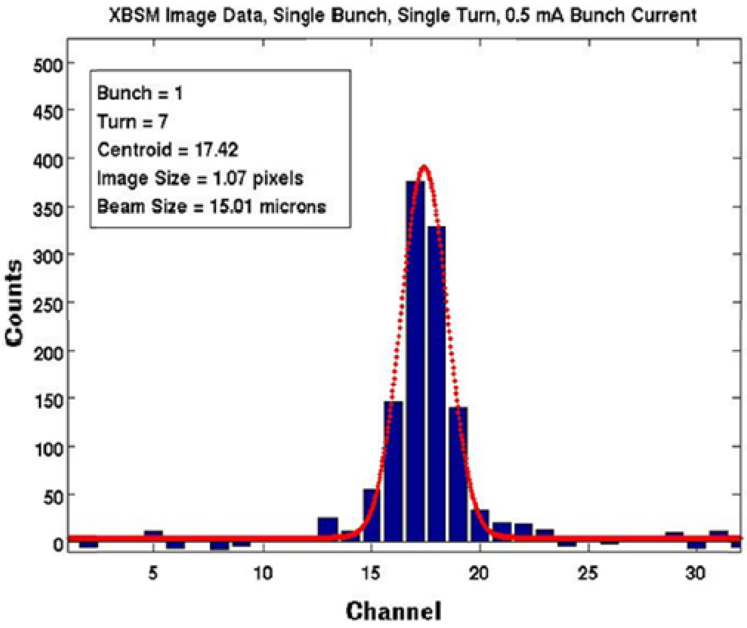

FIGURE 3.4: Pinhole detector histogram with fit using the pinhole (vertical slit) xBSM setup [49].

Due to the broad energy spectrum and associated smoothing of the outer diffraction features it is possible to fit the detector images using an approximate function. The approximate function is the sum of two Gaussians plus a flat background [49]. A pinhole detector beam size measurement with fit is shown in Figure 3.4.

The xBSM can also be used in an interferometer setup using either a Fresnel Zone Plate or coded apertures depending on the particle beam energy. For low beam energies ($E < 2.5$ GeV) a Fresnel zone plate or low energy coded aperture may be used. For beam energies greater than 4 GeV a high power coded aperture is available [49].

3.1.2 Visible Beam Size Monitor (vBSM)

Synchrotron Radiation in the visible spectral range has been widely used for transverse and longitudinal beam profiling. At CesrTA the Visible Beam Size Monitor (vBSM) shown in Figure 3.5 is primarily used for horizontal beam size measurement.

There are two vBSMs located at the East and West ends of the L3 straight section in the North area of the storage ring. The two instruments can measure the counter rotating

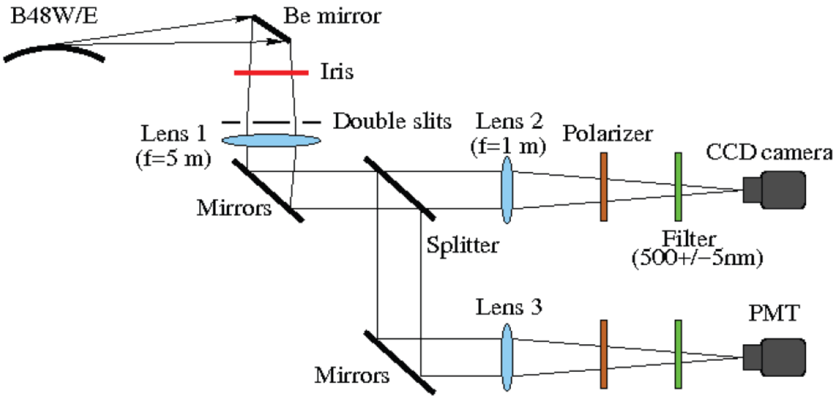

FIGURE 3.5: Layout of vBSM optics [52].

electron and positron beams. The vBSM for the electron beam is 13 m upstream of the DR target apparatus.

For each vBSM setup a soft bending magnet (140 m bending radius) provides the visible SR source. The visible SR is reflected by a water-cooled Beryllium (Be) mirror in the vacuum chamber. The dimensions of this mirror are 22 mm × 12.6 mm (H × V). The resulting angular acceptance is 2.5 mrad × 2.2 mrad (H × V). The visible SR then passes from the vacuum chamber to the optics box through a quartz vacuum window.

Inside the optics box is an adjustable iris, a selection of slits, a lens with 5 m focal length and the next mirror in the optical path. After the optics box a system of mirrors transmits the visible SR from the the accelerator tunnel to an optical table in the experimental hall.

On arrival to the optical table the visible SR is split into two beams using a beam splitter. This allows the simultaneous measurement of the transverse size and bunch length of the charged particle beam by directing the incident SR onto CCD and streak cameras respectively. After the beam splitter, each beam passes through a second focussing lens and bandpass filter [50].

For transverse beam size measurements a wavelength of 500 ± 5 nm is selected. The vBSM can be set up for direct imaging of the SR source to obtain the beam profile or as an interferometer by inserting a double-slit into the optical path as shown in Figure 3.6.

Different slit separations are available and can be remotely inserted into the optical path. All of the slits have a width of 0.5 mm [50]. The slit separations are 2.0, 2.5 and 3.0 mm for horizontal beam size measurement and 3.0, 5.0 and 8.0 mm for vertical beam size measurement, respectively [50].

The visibility of the horizontal polarisation component of the interference pattern is sensitive to the horizontal beam size. Horizontal beam sizes ranging from 50 to 500 μm can be measured with a resolution of approximately 5 μm [53].

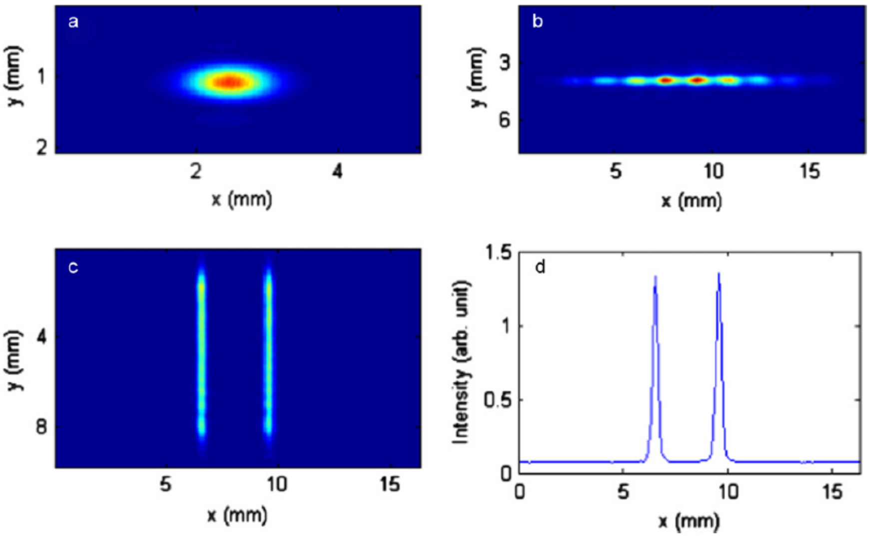

FIGURE 3.6: Typical CCD images recorded by the vBSM at two different image planes: (a) direct image and (b) interferometer image are at the image plane of the source point, (c) is at the image plane of the double slits and (d) is the integrated horizontal intensity profile of (c) [50].

Due to the low intensity of the visible SR the vBSM acquires multi-turn images. The typical exposure time of the CCD camera is 0.5 to 50 ms which given the storage ring revolution period of 2.56 μs equates to around 200 to 20,000 turns [50].

3.2 DR Vacuum Chamber Assembly

3.2.1 Concept of the Vacuum Hardware

An overview of the DR tank is shown in Figure 3.7. The DR tank is about 300 mm long with respect to the electron beam orbit and is predominantly made of stainless steel. The design of the DR tank had to incorporate the DR instrumentation used during CesrTA runs and also a replacement chamber for high current CHESS operation. The DR tank is located on an access walkway of the storage ring in the L3 straight section. Therefore the vacuum chamber is mounted to girders from above ensuring the area below remained free for personnel access.

The replacement chamber is a section of beam pipe mounted on a DC translation mechanism. During DR experimental sessions the replacement chamber is retracted from the electron beam so that the target may be moved into the path of the electron orbit. The replacement chamber is inserted during high current operations, such as CHESS, to minimize the higher order mode loss for the stored beams as they pass through the relatively large vacuum chamber cavity. Figure 3.8 shows the design of the replacement chamber.

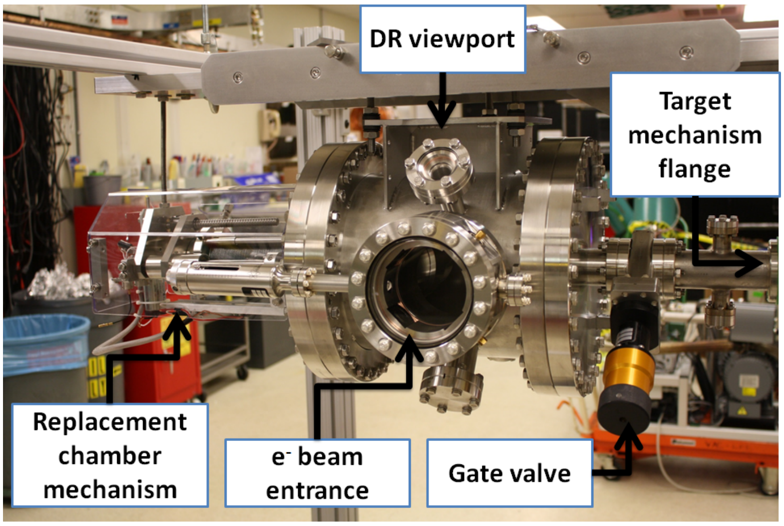

FIGURE 3.7: Overview of the DR vacuum tank.

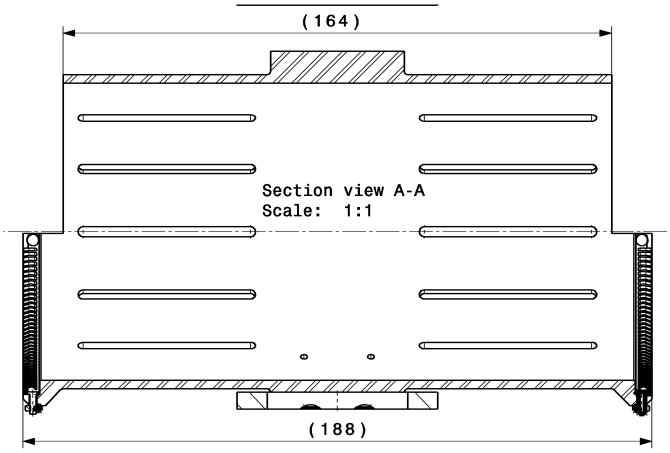

FIGURE 3.8: Technical drawing of the replacement chamber (by N. Chritin and J. Conway).

The diameter of the replacement chamber is 94 mm. The piece is made from Aluminium due to the load restriction of the mechanism and the machining required for the pumping ports. To prevent discontinuities between the storage ring beam pipe and the replacement chamber, springs fixed around the circumference which compress on contact with the storage ring beam pipe were installed. Limit switches were positioned to stop the replacement chamber at the desired contact position inside the DR vacuum tank. The replacement chamber is shown in Figure 3.9.

On the opposite side of the DR tank is the target mechanism. This mechanism has two degrees of freedom: translation IN/OUT and rotation about this axis. Translation is required to insert and retract the target from the beam. Rotation is required to align the BDR with the axis of optical system. The ultra-high vacuum ZTR3070W translator from VG Scienta was chosen. This translator is a stepper motor driven with 300 mm motion range and can be mounted in any orientation. It is bakeable to 230°C. For the

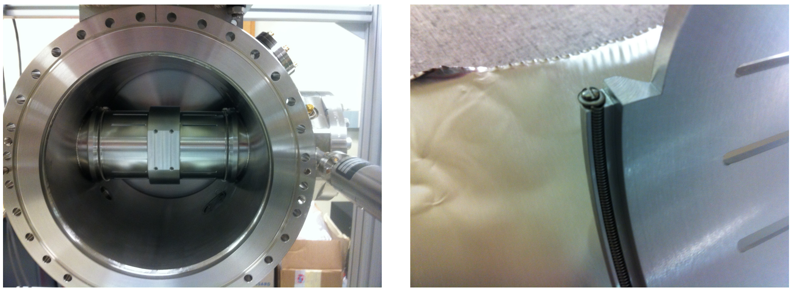

(a) Replacement chamber inserted in the DR tank.
(b) RF contact between the replacement chamber and the beam pipe storage ring.

FIGURE 3.9: Photographs of the replacement chamber (courtesy of J. Conway).

DR experiment the translator was mounted horizontally therefore the ZTRST support tube was included to increase the stability of the sample and prevent sagging of the bellows. The ZTRRB rotary drive accessory was included to support the rotary drive shafts over the travel range.

Between the DR tank and the target mechanism is a manual gate valve and holding chamber. Without compromising the CESR vacuum from the target and mask assembly can be retracted and replaced.

Three viewports have been incorporated in the design of the DR tank. The viewport labelled at the top of the DR tank in Figure 3.7 allows the BDR from the target to enter the optical system for detection. Directly opposite this viewport beneath the chamber is another viewport for visual checks of the target condition and alignment. It should also be noted that this viewport could be used for BDR observation using the counter rotating positron beam. A third flange is available for an additional viewport however this was not necessary. Instead RF probes were connected to measure the efficiency of the replacement chamber.

For the DR window at the top of the DR tank an Excimer UV grade fused silica viewport (Vaqtec part number CF40 3-FS-0116) with a view diameter of 36 mm was chosen. Figure 3.10 shows the spectral transmission efficiency of the viewport. A transmission $> 85\%$ is obtained for wavelengths from 200 nm to 1 μm. A Deep UV grade fused silica viewport (3-FS-0108) with reduced transmission at shorter wavelengths was chosen for the second viewport. Transmission at UV wavelengths for this viewport was not required since this location is primarily used for visual hardware checks.

Two beam position monitors (BPMs) are in close proximity to the DR target location. Directly attached to the DR vacuum tank approximately 30 cm upstream of the DR target is a 4-button beam position monitor (BPM). This BPM is readout continuously during the DR experiment and is labelled “B48AW” in the CESRTA database. Another BPM is located 30 cm downstream of the DR target in the electron beam direction

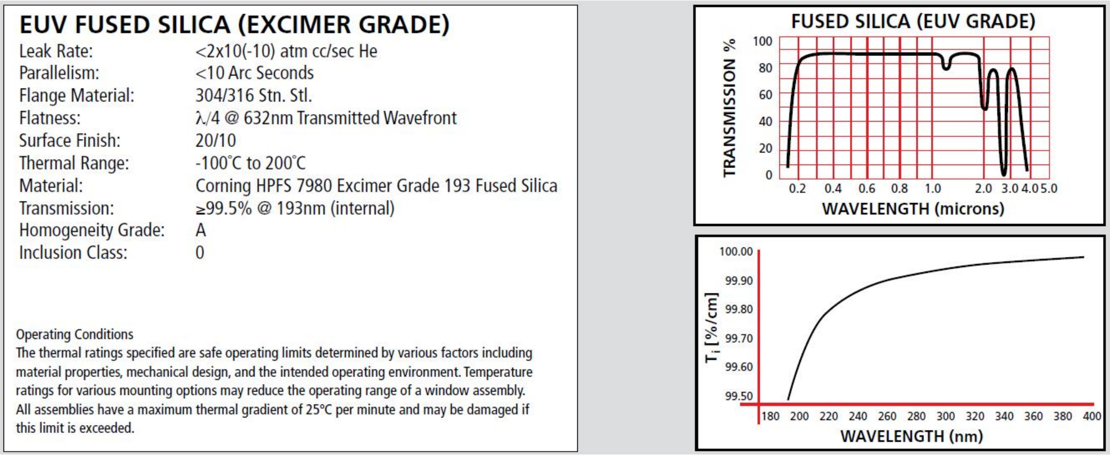

EUV FUSED SILICA (EXCIMER GRADE)

Leak Rate:	<2x10(-10) atm cc/sec He
Parallelism:	<10 Arc Seconds
Flange Material:	304/316 Stn. Stl.
Flatness:	λ/4 @ 632nm Transmitted Wavefront
Surface Finish:	20/10
Thermal Range:	-100˚C to 200˚C
Material:	Corning HPFS 7980 Excimer Grade 193 Fused Silica
Transmission:	≥99.5% @ 193nm (internal)
Homogeneity Grade:	A
Inclusion Class:	0

Operating Conditions
The thermal ratings specified are safe operating limits determined by various factors including material properties, mechanical design, and the intended operating environment. Temperature ratings for various mounting options may reduce the operating range of a window assembly. All assemblies have a maximum thermal gradient of 25°C per minute and may be damaged if this limit is exceeded.

Figure 3.10: DR viewport specification (courtesy of Vaqtec SRL).

labelled “B48W”. This BPM is a member of the CESR beam position monitor (cBPM) system and is triggered to acquire turn-by-turn beam orbits.

3.3 Target and mask

All previous DR experiments were installed on linear machines. A typical target in these tests consisted of a screen similar to those used for OTR with the modification of a circular or rectangular hole. On circular machines, the target must be retracted during injection of the beam to the storage ring and then inserted to the stable beam. Therefore the targets used on circular machines must be modified further to have a fork-like shape. Two fabrication techniques have been used for the targets: chemical etching and molecular adhesion. For all targets the roughness, aperture size and coplanarity must be controlled during fabrication to avoid distortions in the DR angular distribution.

3.3.1 Dummy Target

For the commissioning of the DR instrumentation a dummy target was installed as shown in Figure 3.11. The dummy target was machined from unpolished stainless steel with aperture sizes of 1.0 and 0.5 mm. The apertures were etched such that given a target tilt angle $\theta_0 = 70°$ the effective aperture size to the beam would not be significantly reduced by the thickness of the target. The reflectivity of this target was relatively poor therefore beam size measurements were not viable. However, with this dummy target all of the instrumentation could be tested, a method of beam alignment to pass through the apertures was established and the beam lifetime in the aperture was observed.

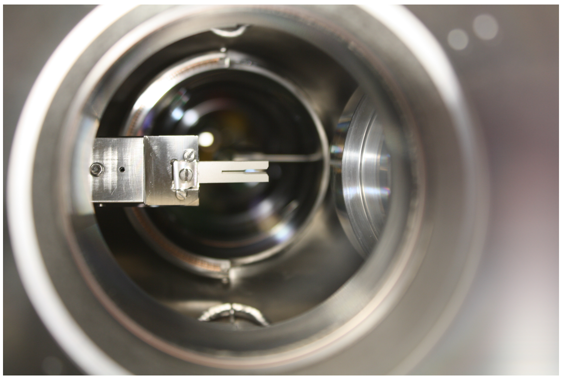

FIGURE 3.11: Dummy target in the vacuum chamber viewed from the downstream direction (courtesy of Y. Li).

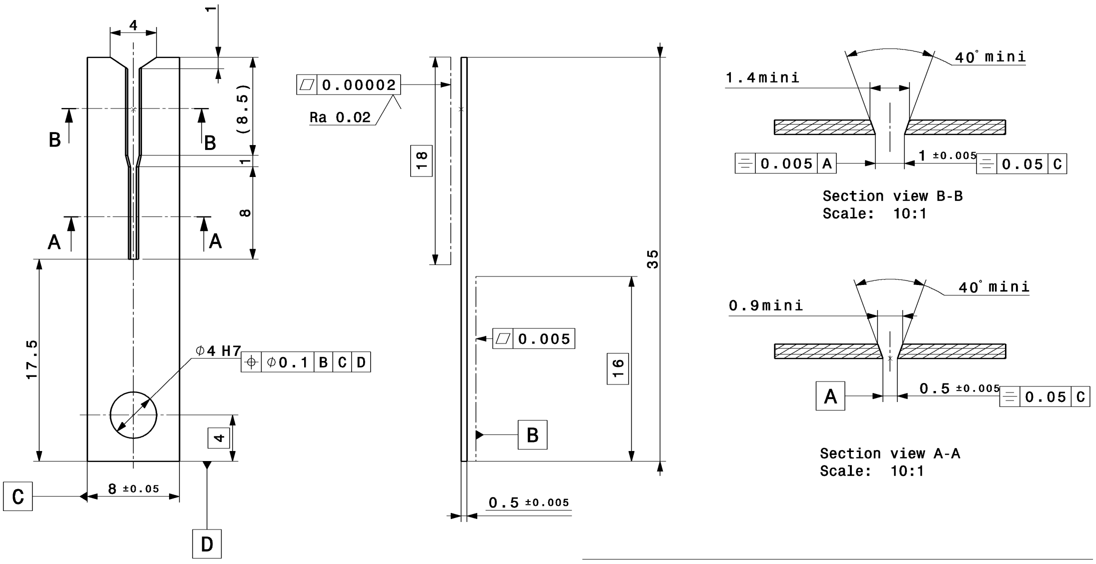

FIGURE 3.12: Technical drawing of the chemically etched target (by N. Chritin).

3.3.2 Chemically Etched Target

Initially the targets were made of polished silicon. In addition to the aperture size, another crucial property of these targets is the coplanarity between the upper and lower tines. The coplanarity δ should be within a fraction of the wavelength λ at which DR is observed to prevent distortions in the DR angular distribution i.e. $\delta = 0.1\lambda$. For $\lambda = 500$ nm, the coplanarity should be ≤ 50 nm [12]. The tines of these targets were etched.

Chemical etching is a process where silicon wafers are dipped into an etchant which is traditionally an acidic mixture [55]. The technical drawing of the chemically etched target is shown in Figure 3.12. A photograph of this target is shown in Figure 3.13. Although the apertures could be fabricated within tolerance, the coplanarity of the tines could not be guaranteed. Therefore an alternative fabrication technique was also investigated.

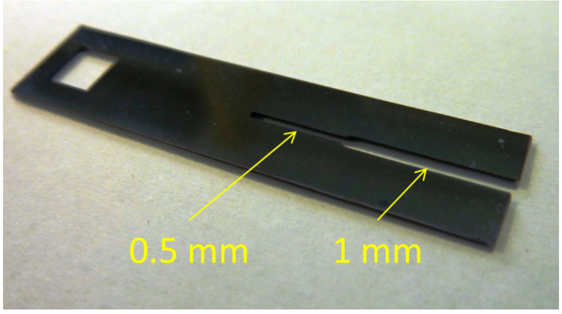

FIGURE 3.13: Combined 0.5 and 1.0 mm aperture chemically etched target [54].

Metrology was conducted at CERN to measure the properties of the chemically etched targets. The roughness parameters are defined, using Figure 3.14, as follows [54]:

Maximum profile peak height $Rp = \max(Z(x))$

Largest profile peak height within a sample length.

Maximum profile valley depth $Rv = \min(Z(x))$

Largest profile valley depth Rv within sampling length.

Total height of profile $Rt = \max(Zp_i) + \max(Zv_i)$

Sum of the height of the largest profile peak height Zp and the largest profile valley depth Zv within the evaluation length. The evaluation length is greater than the sampling length.

Arithmetical mean deviation of the assessed profile $Ra = \frac{1}{l}\int\limits_0^l |Z(x)|\,\mathrm{d}x$

Arithmetic mean of the absolute values $Z(x)$ within a sampling length.

Root mean square deviation of the assessed profile $Rq = \sqrt{\frac{1}{l}\int\limits_0^l |Z^2(x)|\,\mathrm{d}x}$

Root mean square value of the values $Z(x)$ within the sampling length.

Table 3.4 shows the conditions for each measurement type. All measurements were performed at room temperature (20 ± 1° C). The VEECO-NT 3300 instrument is a non-contact, optical profiler used to measure roughness and flatness of samples by interferometry. The MAHR Wegu OMS 600 is a 3D optical coordinate measurement machine using multisensor technology [54].

Four chemically etched targets were measured, these were split into two sets denoted “7V” and “2V”. Each set contains a combined 0.5 and 1.0 mm aperture target and a 1 mm target.

The surface roughness of the target determines the quality of specular reflection of the incident rays. A rough surface causes incident photons to be scattered in all directions resulting on a diffuse reflection. This is undesirable since photons may be scattered

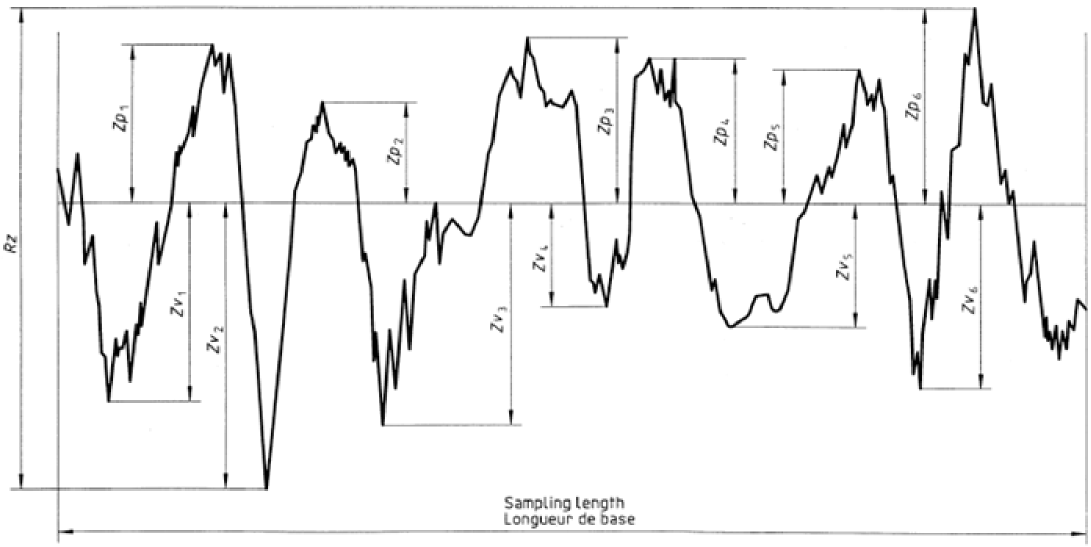

FIGURE 3.14: Definitions of roughness measurement where peaks and valleys are labelled Zp_i and Zv_i respectively over the sampling length l [54].

	Roughness	**Flatness**	**Distance**
Instrument	Roughness tester VEECO-NT 3300	Roughness tester VEECO-NT 3300	MAHR Wegu OMS 600
Optical Zoom	×20	×2.5	×40
Optical lens	×1	×0.5	-
Estimated uncertainty	10%	10%	±2 μm

TABLE 3.4: Conditions of measurement for the masks and chemically etched targets [54].

outside of the acceptance aperture of the optical system leading to a reduced light intensity and distorted angular distribution. For DR measurements this is problematic because beam size measurements are taken from the angular distribution of the reflected rays.

The roughness results for the chemically etched targets are summarised in Table 3.5. The average roughness was < 2.5 nm. Specular reflection will occur provided the surface roughness is small compared to the wavelength of the incident rays i.e. the wavelets will only interfere constructively in one direction. Based on these results, a high reflectivity was expected at visible - UV wavelengths.

The aperture size of each target was also measured and compared to the specification value (see Table 3.6). It was found that the average difference between the specification value and measured value was 3.03 μm.

Another important parameter of the targets is the flatness. A non-zero coplanarity between the tines of the target causes a phase shift of the DR photons emitted in the

	Set 7V			
	0.5 − 1.0 mm **target**		1.0 mm **target**	
Roughness parameter	**Mean**	**Std Dev**	**Mean**	**Std Dev**
Rq [nm]	4.412	1.334	1.797	0.594
Ra [nm]	2.353	0.439	1.217	0.190
Rt [nm]	60.493	23.023	19.790	13.166
Rp [nm]	39.524	20.573	8.804	7.706
Rv [nm]	-20.969	8.660	-10.986	9.020
	Set 2V			
Rq [nm]	3.571	1.737	3.331	1.161
Ra [nm]	1.917	0.448	1.801	0.343
Rt [nm]	49.328	32.167	47.253	21.663
Rp [nm]	33.038	29.166	28.946	17.863
Rv [nm]	-16.290	6.587	-18.306	8.375

Table 3.5: Roughness results for the chemically etched targets [54].

Set	**Specification** [mm]	**Average value** [μm]	**Std Dev** [μm]	**No. values**
7V	0.5	501.9	7.0	5
	1.0	1003.7	8.5	9
	1.0	1002.7	6.7	16
2V	0.5	498.9	7.3	5
	1.0	997.7	7.6	9
	1.0	993.5	7.7	16

Table 3.6: Aperture size measurement of the chemically etched targets [54].

backwards direction relative to the electron beam. The presence of this phase difference is observed as an asymmetry in the angular distribution of DR (see Chapter 2). The visibility, which is the ratio of the maximum and central minimum intensities of the angular distribution is sensitive to beam size. Therefore the asymmetry caused by non-coplanar tines introduces a systematic error in the vertical beam size measurement.

	Set 7V			
	0.5 − 1.0 mm **target**		1.0 mm **target**	
	Loc. 1	**Loc. 2**	**Loc. 1**	**Loc. 2**
Max-to-min [μm]	2.74	9.66	0.90	2.34
Tilt in x-direction [μrad]	0.0	587.8	0.0	114.1
Tilt in y-direction [μrad]	0.0	−8.9	0.0	−6.2
	Set 2V			
Max-to-min [μm]	0.64	0.62	1.12	4.58
Tilt in x-direction [μrad]	0.0	−17.6	0.0	229.1
Tilt in y-direction [μrad]	0.0	37.9	0.0	−2.7

Table 3.7: Summary of flatness measurements for the chemically etched targets [54].

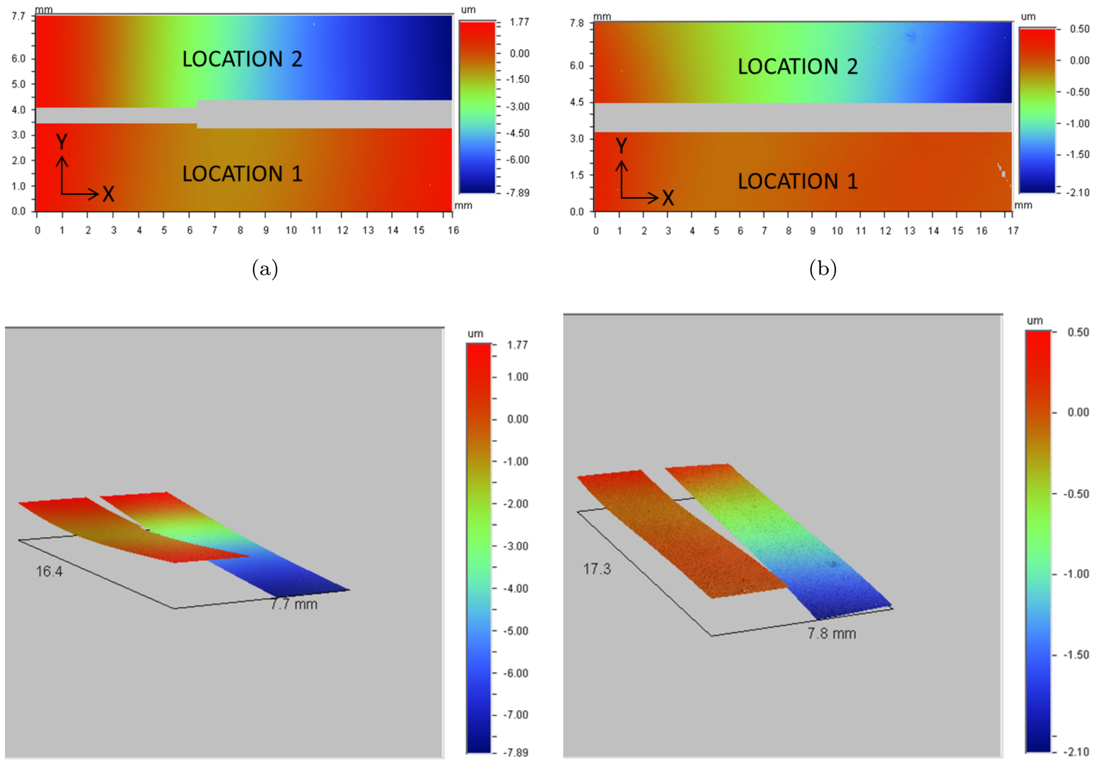

(a) (b)

(c) (d)

FIGURE 3.15: Measurements of the flatness across the set 7V targets: (a, c) combined 0.5/1.0 mm target and (b, d) 1.0 mm target [54].

In Figure 3.15 and Figure 3.16 the spatial distributions of the flatness across the targets is illustrated. The flatness results over the tines of the chemically etched targets are summarised in Table 3.7. A variation up to 10 μm was observed. From the spatial distributions of the flatness across the targets it was observed that the coplanarity worsens moving from the innermost slit position to the ends of the tines of the target in the x-direction. The coplanarity of the four chemically etched targets showed a wide variation from < 0.1 μm to 10 μm. Based on the flatness measurements the best chemically etched target was identified to be the 2V 0.5/1.0 mm target. Therefore this target was mounted and installed in the DR monitor. The coplanarity of this target ranged from < 0.1 μm at the innermost (0.5 mm) part of the aperture to 0.75 μm at the ends of the tines [54].

3.3.3 Molecular Adhesion Targets

Bonding by molecular adhesion is a technique that enables two substrates having polished surfaces to adhere to one another, without the application of adhesive [56]. The upper and lower tines of the target are machined separately in sets. The tines are then paired together in all variations to identify which upper/lower pairs result in the best

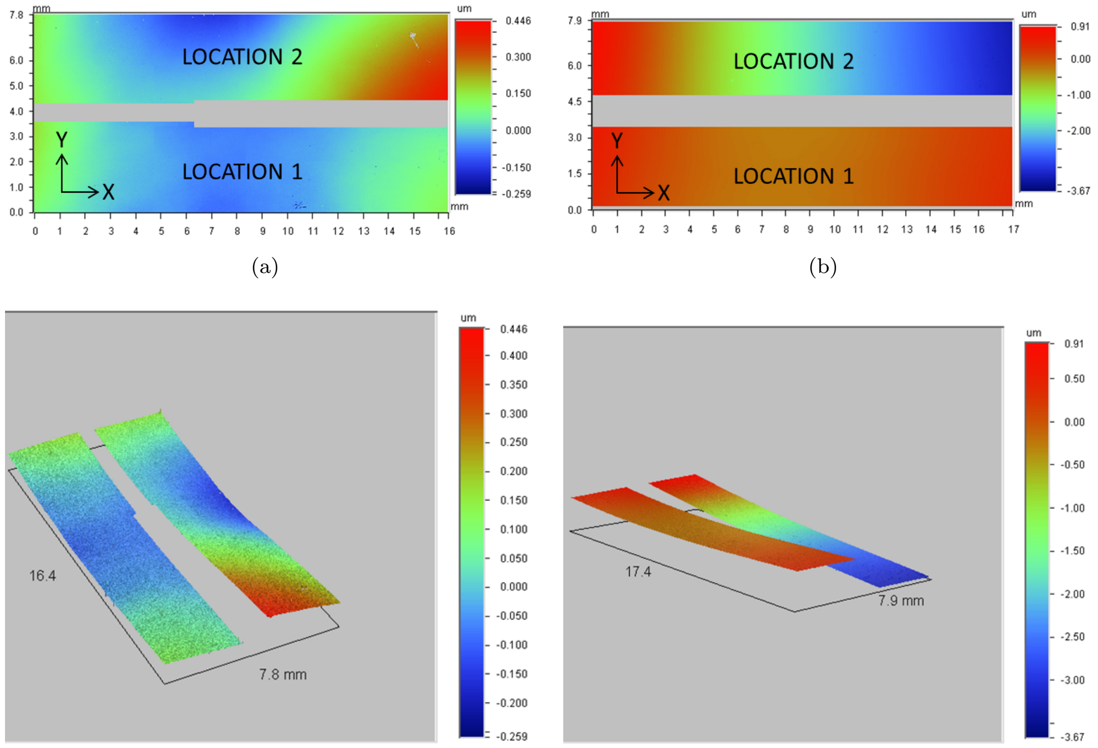

(a) (b)

(c) (d)

FIGURE 3.16: Measurements of the flatness across the set 2V targets: (a, c) combined 0.5/1.0 mm target and (b, d) 1.0 mm target [54].

coplanarity and attached to a flat mounting block. In effect, the molecular adhesion target consists of three individually machined pieces: two tines and the mounting block.

FIGURE 3.17: Photograph of the 2 mm Silicon molecular adhesion target.

Two sets of molecular adhesion targets were manufactured. The first set were made of polished Silicon (Si). The second set were made of Suprasil fused Silica (SiO_2) glass with an Aluminium (Al) and Chromium (Cr) coating to enhance the reflectivity at visible and UV wavelengths. The coating was adjusted from pure Al to an Al-Cr alloy to increase the tensile strength and maintain the high spectral reflectance.

Whilst chemically etched components have been widely used in physics applications, molecular adhesion is a relatively new technique and as such, is not currently well understood. Considerations had to be made regarding the expected lifetime and fragility of the molecular adhesion targets in an irradiated environment. One concern was whether thermal heating due to scattered electrons impacting the target would break the molecular adhesion bond. As a consequence, a mounting clamp surrounds the target assembly as a precaution that should the molecular adhesion bonds break, then the individual pieces remain mounted to the target holder and cannot fall into the DR vacuum tank.

The polished Si and Al/Cr coated Silica molecular adhesion targets were measured during manufacture. Reports were provided by Winlight Optics. Metrology was not practical at CERN due to the fragility of the unmounted targets.

The technical drawing of the 1 mm Al/Cr coated Silica molecular adhesion target is shown in Figure 3.18. The dimensions of the target tines and mounting block are labelled. The area used for metrology is marked “zone utile”. The area of molecular adhesion between the mounting block and the tines is also labelled. Akin to the chemically etched targets, the tines were etched at an angle $> 20°$ to ensure that given the tilt angle $\theta = 70°$, the effective aperture was not reduced. The thickness of the molecular adhesion targets is 1 mm larger than that of the chemically etched targets. Therefore etching of the molecular adhesion targets had to meet the specification value.

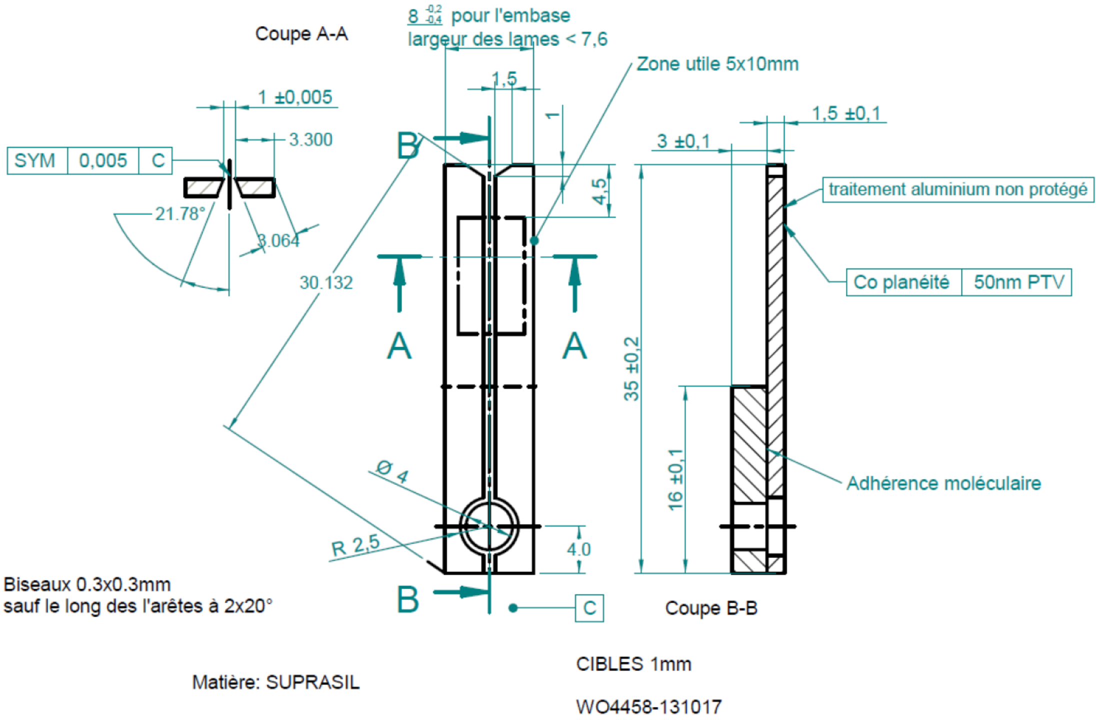

Figure 3.18: Technical drawing of the 1.0 mm Al/Cr coated Silica molecular adhesion target (courtesy of Winlight Optics).

The specification and measured values for the mounting block, tines and assembled 1 mm and 0.5 mm Al/Cr coated Silica molecular adhesion targets are shown in Tables 3.8 - 3.13. All of the measured parameters were within the tolerances of the specification. The coating of the targets was modified. Instead of Aluminium only the targets were coated using a combination of Chromium and Aluminium.

Parameter	**Specification**	**Result**
Material	Silica	Suprisal fused Silica
Thickness	3 ± 0.1 mm	3.08 mm
Dimensions	$16 \pm 0.1 \times 8\ -0.2/-0.4$ mm	16.064 mm × 7.75 mm
Mounting hole	$\varnothing 4 \pm 0.2$ mm	$\varnothing$4.08 mm
Hole position	4 ± 0.1 mm $\times$ 3.85 ± 0.1 mm	4.03 mm × 3.87 mm
Flatness	$<$ 50 nm PTV	56 nm PTV (total) 35 nm PTV (adhered)

Table 3.8: Comparison of the specification and measured values of the block for the 1 mm Al/Cr coated Silica molecular adhesion target (courtesy of Winlight Optics).

Parameter	**Specification**	**Left Tine Result**	**Right Tine Result**
Material	Silica	Suprisal 2B fused Silica	
Thickness	1.5 ± 0.1 mm	1.571 mm	
Dimensions	35 ± 0.2 mm $\times$ $<$ 3.3 mm	35.109 mm × 3.300 mm	
Mounting hole	$R2.5 \pm 0.1$ mm	2.53 mm	
Hole position	4 ± 0.1 mm $\times$ 4 ± 0.1 mm	4.00 mm × 4.03 mm	
Etch angle	$>$ 20°	21.78°	
Flatness	$<$ 50 nm PTV	21 nm PTV	

Table 3.9: Comparison of the specification and measured values of the tines for the 1 mm Al/Cr coated Silica molecular adhesion target (courtesy of Winlight Optics).

Parameter	**Specification**	**Result**
Aperture	1.0 ± 0.005 mm	1.003 mm (at 4.5 mm) 1.005 mm (at 14.5 mm)
Length	35 ± 0.2 mm	35.1 mm
Coplanarity	$<$ 50 nm PTV	31 nm PTV
Coating	Aluminium	Aluminium + Chromium

Table 3.10: Metrology results of the assembled 1 mm Al/Cr coated Silica molecular adhesion target (courtesy of Winlight Optics). The positions of 4.5 mm and 14.5 mm correspond to the start and end points of the “zone utile” area.

Fabrication using molecular adhesion produced similar results to chemical etching for the aperture size of the target. In Table 3.10 the average difference between the specification and measured aperture size was 4 μm.

Generally the coplanarity of the molecular adhesion targets was an order of magnitude smaller than the chemically etched targets. The fabricated molecular adhesion targets also met the experimental requirement that the coplanarity is a fraction of the wavelength in the UV-Visible spectral range ($\delta = 0.1\lambda$). The overall flatness of the assembled molecular adhesion target is determined by the flatness of the three individual components. For the 1 mm Al/Cr coated Silica molecular adhesion target, from Tables 3.8

Parameter	**Specification**	**Result**
Material	Silica	Suprisal fused Silica
Thickness	3 ± 0.1 mm	3.08 mm
Dimensions	$16 \pm 0.1 \times 8\ -0.2/-0.4$ mm	16.064 mm × 7.75 mm
Mounting hole	$\varnothing 4 \pm 0.2$ mm	$\varnothing 4.08$ mm
Hole position	4 ± 0.1 mm $\times$ 3.85 ± 0.1 mm	4.03 mm × 3.87 mm
Flatness	< 50 nm PTV	84 nm PTV (total) 40 nm PTV (adhered)

Table 3.11: Comparison of the specification and measured values of the block for the 0.5 mm Al/Cr coated Silica molecular adhesion target (courtesy of Winlight Optics).

Parameter	**Specification**	**Left Tine Result**	**Right Tine Result**
Material	Silica	Suprisal 2B fused Silica	
Thickness	1.5 ± 0.1 mm	1.571 mm	
Dimensions	35 ± 0.2 mm $\times\ < 3.3$ mm	35.109 mm × 3.300 mm	
Mounting hole	$R2.5 \pm 0.1$ mm	2.53 mm	
Hole position	4 ± 0.1 mm $\times$ 4 ± 0.1 mm	4.00 mm × 4.03 mm	
Etch angle	$> 20°$	21.78°	
Flatness	< 50 nm PTV	20 nm PTV	

Table 3.12: Comparison of the specification and measured values of the tines for the 0.5 mm Al/Cr coated Silica molecular adhesion target (courtesy of Winlight Optics).

Parameter	**Specification**	**Result**
Aperture	0.5 ± 0.005 mm	0.503 mm (at 4.5 mm) 0.503 mm (at 14.5 mm)
Length	35 ± 0.2 mm	35.1 mm
Coplanarity	< 50 nm PTV	45 nm PTV
Coating	Aluminium	Aluminium + Chromium

Table 3.13: Metrology results of the assembled 0.5 mm Al/Cr coated Silica molecular adhesion target (courtesy of Winlight Optics). The positions of 4.5 mm and 14.5 mm correspond to the start and end points of the "zone utile" area.

and 3.9 the flatness of the adhesive area of the mounting block and tines was 35 nm and 21 nm respectively. The resulting coplanarity of the assembled target was 31 nm. To appreciate the scale at which the coplanarity is evaluated, the diameter of a human hair is approximately 100,000 nm. For the 0.5 mm Si molecular adhesion target the measured coplanarity was 56.486 ± 10.677 nm. Figure 3.19 shows the metrology results for the 1.0 mm Si molecular adhesion target where the measured coplanarity was 68.479 ± 13.909 nm. In contrast to the chemically etched targets, a trend was not observed between the position along the target and the coplanarity.

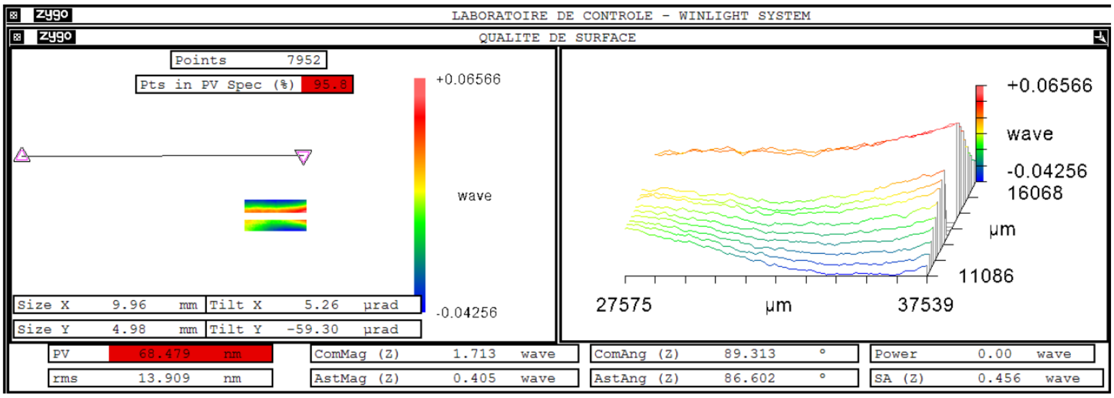

Points 7952
Pts in PV Spec (%) 95.8
Size X 9.96 mm
Tilt X 5.26 µrad
Size Y 4.98 mm
Tilt Y -59.30 µrad
PV 68.479 nm
rms 13.909 nm
ComMag (Z) 1.713 wave
AstMag (Z) 0.405 wave
ComAng (Z) 89.313 °
AstAng (Z) 86.602 °
Power 0.00 wave
SA (Z) 0.456 wave

FIGURE 3.19: Flatness measurements for the 1.0 mm Si molecular adhesion target (courtesy of Winlight Optics).

3.3.4 Target Reflectance

The intensity of BDR scales with the reflectivity of the target surface. It is assumed that photons travel from vacuum and are incident on an absorbing material. In order to plot the spectral curves for different elements, the intensity reflection coefficients, R_S and R_p, must be calculated where the subscripts s and p denote the horizontal and vertical polarisation components. The method of effective indexes combined with Berning's system of equations is applied. For further detail on these methods the reader is should refer to [57].

Considering an on-axis electron beam as shown in Figure 3.20 where $\hat{n}$ is the unit vector normal to the target surface, the angle of incidence

$$\theta_i = \frac{\pi}{2} - \theta_0, \tag{3.1}$$

is given by the target tilt angle θ_0 in radians. Here a screen used for TR has been considered for simplicity however the results are also applicable for DR. The s and p polarisation components of the electric field are perpendicular and in the plane of the paper respectively in Figure 3.20.

The vacuum is assumed to be non-absorbing and is denoted by the subscript 0 with refractive index $n_0 = 1$. The effective indexes,

$$\eta_{0s} = n_0 \cos\theta_i \tag{3.2}$$

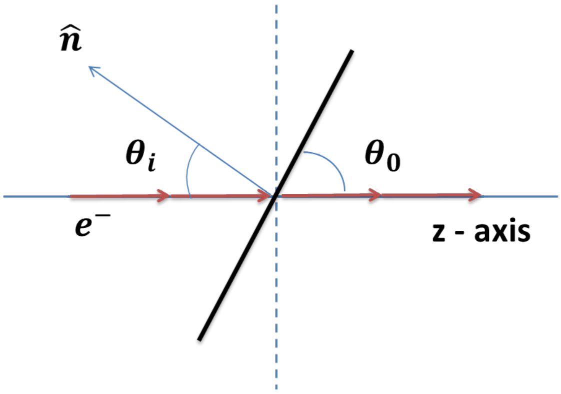

FIGURE 3.20: Schematic of the reflection geometry of the target.

$$\eta_{0p} = \frac{n_0}{\cos\theta_i} \tag{3.3}$$

which are used for convenience, scale the refractive index n_0 by the cosine of the angle of incidence θ_i.

The absorbing material is denoted by the subscript 1. The optical constants n_1 and k_1 for various materials can be found in [58]. The complex effective indexes [57] in the absorbing material are

$$\bar{\eta}_{1s} = \bar{n}_1 \cos\Theta_1 \tag{3.4}$$

and

$$\bar{\eta}_{1p} = \frac{\bar{n}_1}{\cos\Theta_1}, \tag{3.5}$$

where $\bar{n}_1 = n_1 - ik_1$ is the complex refractive index in the material and

$$\cos\Theta_1 = \left[\frac{(\alpha_1^2+\beta_1^2)^{1/2}+\alpha_1}{2}\right]^{1/2} - i\left[\frac{(\alpha_1^2+\beta_1^2)^{1/2}-\alpha_1}{2}\right]^{1/2}, \tag{3.6}$$

given the parameters

$$\alpha_1 = 1 + \left(\frac{n_0 \sin\theta_i}{n_1^2 + k_1^2}\right)^2 (k_1^2 - n_1^2) \tag{3.7}$$

and

$$\beta_1 = -2n_1k_1 \left(\frac{n_0 \sin\theta_i}{n_1^2 + k_1^2}\right)^2. \tag{3.8}$$

The amplitude reflection coefficients, r_s and r_p, are given by

$$r_s = \frac{\eta_{0s} - \eta_{1s}}{\eta_{0s} + \eta_{1s}} \tag{3.9}$$

and

$$r_p = \frac{\eta_{1p} - \eta_{0p}}{\eta_{1p} + \eta_{0p}}. \tag{3.10}$$

The intensity reflection coefficients [57], R_s and R_p, corresponding to the horizontal and vertical directions of the target coordinate system respectively are given by

$$R_{s,p} = r_{s,p} r_{s,p}^*. \tag{3.11}$$

Assuming an on-axis electron beam at normal incidence ($\theta_i = 0$), the intensity reflection coefficients of the s and p polarisation components are equal [57] as shown in

$$R_s = R_p = \frac{(n_0 - n_1)^2 + k_1^2}{(n_0 + n_1)^2 + k_1^2}. \tag{3.12}$$

The intensity transmission coefficients [57], T_s and T_p, may be obtained using

$$T_{s,p} = 1 - R_{s,p}. \tag{3.13}$$

The target surface materials were chosen for their high reflectivity. In Figure 3.21 the polarisation reflectance curves for different materials are shown. It is seen that aluminium has the highest reflectivity over the 200 to 600 nm wavelength range.

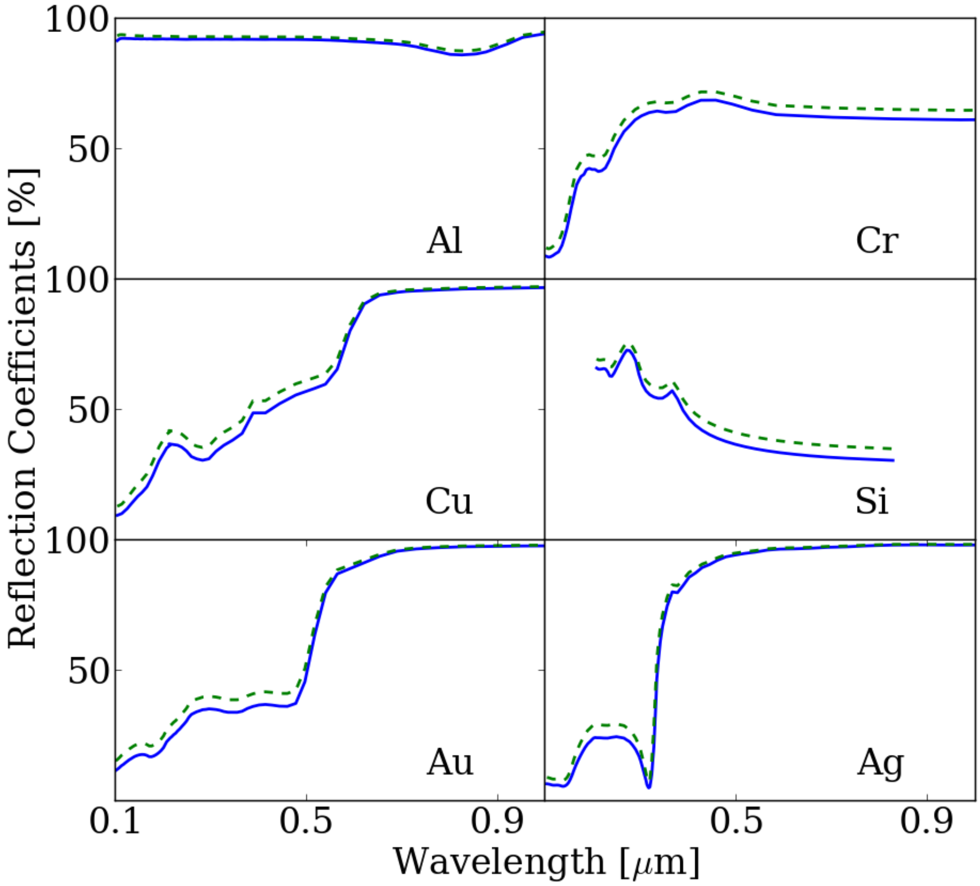

FIGURE 3.21: Reflectance curves for different materials at target tilt angle $\theta_0 = 70°$: the "solid line" denotes the vertical polarisation component R_p and the "dashed line" denotes the horizontal polarisation component R_s.

3.3.5 Mask

A Silicon Carbide mask was used to reduce the contribution of SR to background and was mounted upstream of the target as shown in Figure 3.22. The mask was not etched since it is orientated perpendicular to the incident electron beam. Typically the mask aperture was four times larger than the target aperture to minimise interference effects. For the molecular adhesion targets a stepped mask was used with aperture sizes a factor of four and two larger than the target aperture to allow the observation without and with interference effects between FDR from the mask and BDR from the target respectively. Table 3.14 shows a list of the different masks for 0.5 and 1.0 mm target apertures.

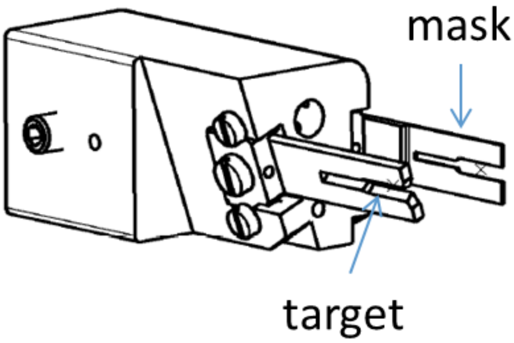

FIGURE 3.22: Target holder with mask and target mounted (by N. Chritin).

Mask	**Apertures** [mm]	**Quantity**
E	1.0, 2.0	2
H	2.0, 4.0	2

TABLE 3.14: Mask aperture sizes.

The masks were also sent for metrology to verify the aperture size and compare the results obtained from laser machining of the masks to the target fabrication techniques. It was expected that laser machining would produce significantly worse flatness results due to warping by thermal heating of the material. The masks were also unpolished, therefore the surface roughness is large. For completeness the roughness results are included in Table 3.15. The measurement conditions were the same as those for the chemically etched targets detailed in Table 3.4.

	Mask E1		**Mask E2**	
Roughness parameter	**Mean**	**Std Dev**	**Mean**	**Std Dev**
Rq [nm]	235.779	49.924	231.447	57.691
Ra [nm]	166.630	35.261	160.847	41.858
Rt [nm]	1876.287	492.751	1887.376	491.109
Rp [nm]	644.567	136.817	626.531	160.049
Rv [nm]	-1231.720	427.411	-1260.845	405.579
	Mask H1		**-**	
Rq [nm]	294.649	42.290		
Ra [nm]	215.725	21.505		
Rt [nm]	2310.384	809.142		
Rp [nm]	846.953	608.186		
Rv [nm]	-1463.432	437.658		

TABLE 3.15: Roughness results for the masks [54].

The aperture size of the masks were also measured and compared to the specification values (see Table 3.16). On average the difference between the specification and measured aperture size was 64.2 μm. This difference may cause a small modification to the expected DR angular distribution using the specification values.

Mask	**Spec.** [mm]	**Average value** [μm]	**Std Dev** [μm]	**No. values**
E1	1.0	1073.3	2.3	8
	2.0	2067.3	2.2	8
E2	1.0	1080.4	2.6	8
	2.0	2058.1	2.2	8
H1	2.0	2059.7	5.5	8
	4.0	4046.1	1.4	8

TABLE 3.16: Aperture size measurement of the masks [54].

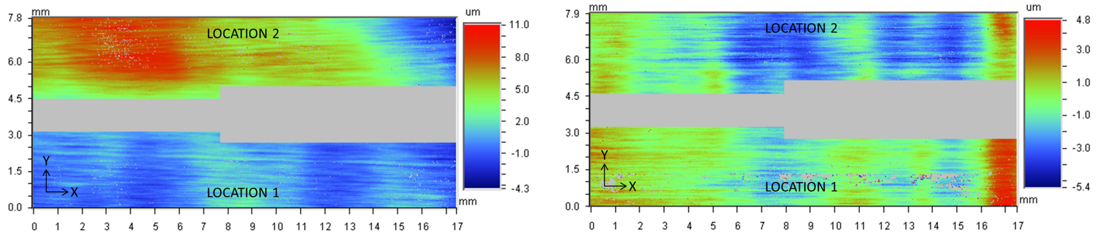

(a) caption (b) caption

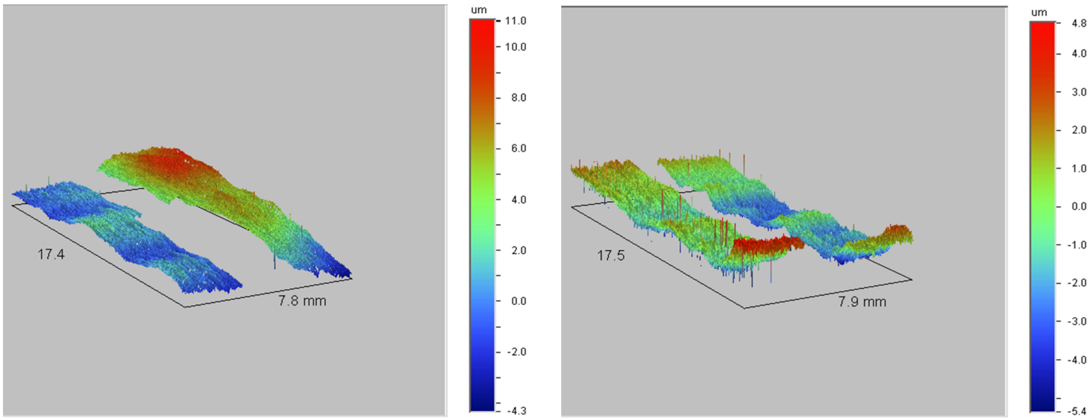

(c) caption (d) caption

FIGURE 3.23: Measurements of the flatness across masks E: (a, c) Mask E1 and (b, d) Mask E2 [54].

The flatness results for masks E and H are shown in Figure 3.23 and Figure 3.24. Only one mask H was available for metrology. It was seen that there was a large coplanarity offset on the order of tens of microns for all of the masks measured. Table 3.17 shows the measured flatness across each tine of the masks. No trend was observed in the spatial distribution of the flatness versus position along the tines in the x-direction. It should be noted that for interference measurements the coplanarity of the mask does not affect the FDR emitted. A max-to-min variation of the flatness across each tine up to 100 μm was observed.

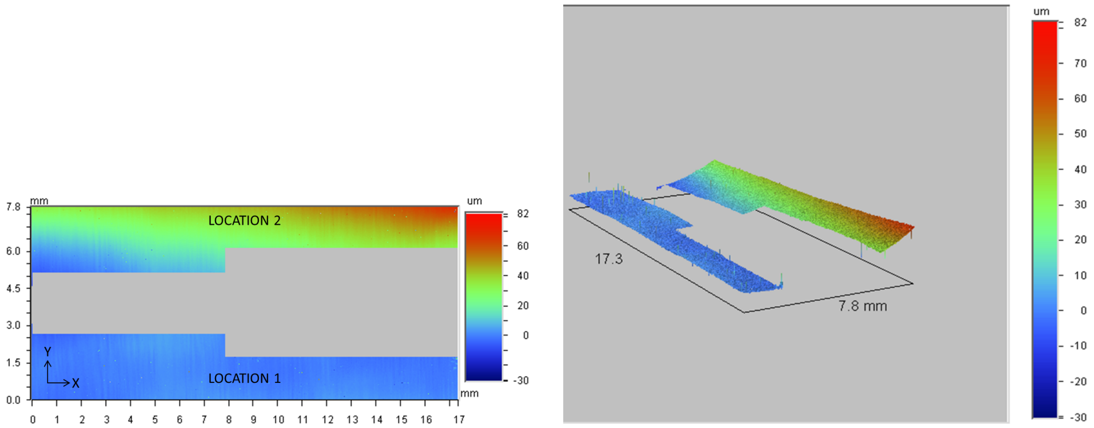

(a) caption (b) caption

FIGURE 3.24: Measurements of the flatness across Masks H [54].

	Mask E1		Mask E2	
	Loc. 1	**Loc. 2**	**Loc. 1**	**Loc. 2**
Max-to-min [μm]	≈ 8	≈ 15	≈ 7	≈ 9
Tilt in x-direction [μrad]	-	395	-	61
Tilt in y-direction [μrad]	-	-172	-	120
	Mask H1		**-**	
Max-to-min [μm]	≈ 10	≈ 80		
Tilt in x-direction [μrad]	-	-1897		
Tilt in y-direction [μrad]	-	-13913		

TABLE 3.17: Flatness measurements across each tine for the masks [54].

3.4 Optical System

Figure 3.25 shows the main components of the optical system. Overviews of the optical system are shown in Figure 3.26. Figure 3.26(a) shows a photograph of the DR tank and optical system assembled in the vacuum laboratory before installation in CESR. Here the scale of the compact optical system relative to the DR vacuum tank can be seen. A compact design was chosen for simpler alignment and installation in the beamline. The length of the optical system (mirror to detector) is < 1 m. Considerations were made into the positioning and radiation hardness of the camera due to the close proximity to the beam pipe. The optical system is raised above the radial plane of the storage ring such that the secondary emissions due to SR incident on the camera were reduced. In Figure 3.27 a technical drawing illustrating the order and positions of the optical components is presented.

Directly after the DR viewport is a mirror. The Deep UV Aluminium mirror (DUVA-PM-2037-UV) from CVI Melles Griot was chosen. The mirror is mounted in a remotely controlled motorised Zaber mirror mount (ZABT-MM2-KT04).

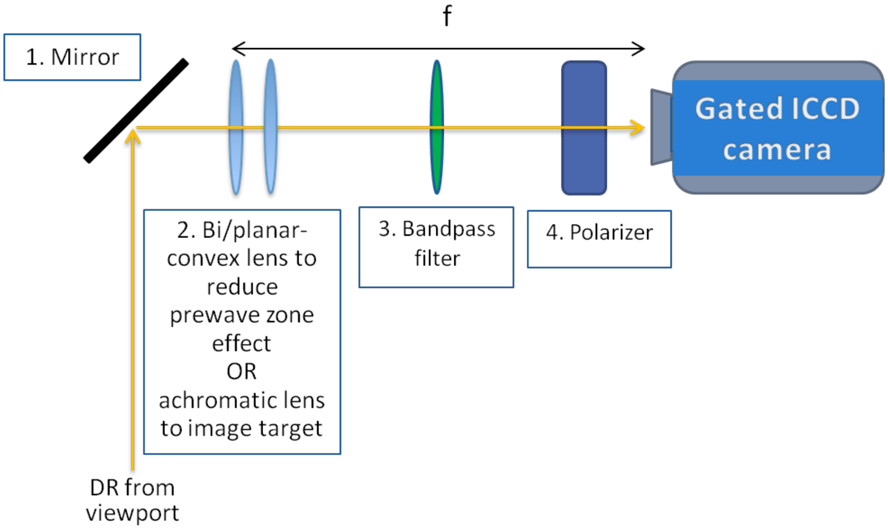

FIGURE 3.25: Optical system schematic showing the main components.

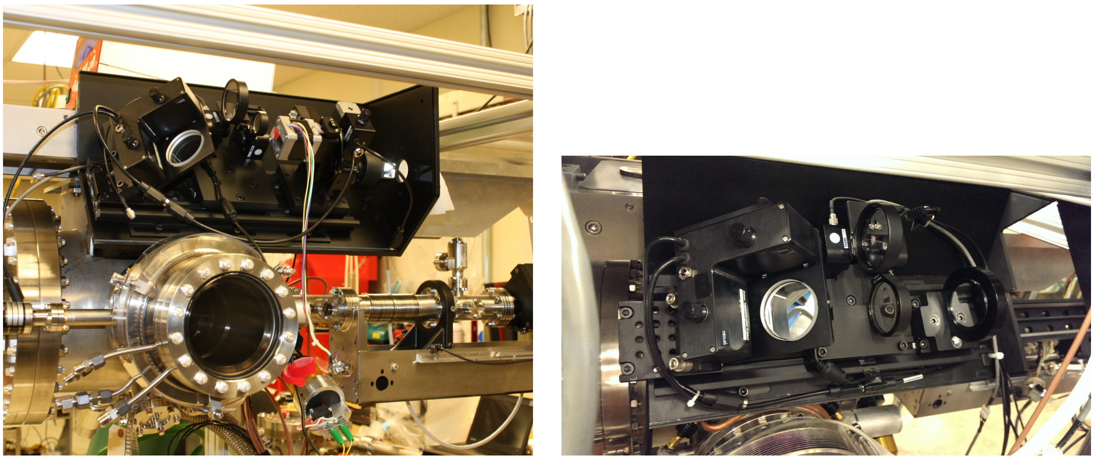

(a)

(b)

FIGURE 3.26: Photographs of the optical system: (a) in December 2013 before installation and (b) in December 2014 in the accelerator tunnel.

The DR monitor requires a dual purpose optical system. Direct imaging of the target surface is used for alignment of the electron beam in the target aperture. The AC508-150-A achromat doublet provided by Thorlabs was chosen. This lens has a focal length of 150 mm, $\varnothing 2''$ clear aperture and is suitable for the 400 nm to 700 nm spectral range. Imaging of the DR angular distribution is required for vertical beam size measurement. Due to its compact length the optical system is within the prewave zone. To obtain the angular distribution within the prewave zone a lens is required with the camera positioned in the back focal plane [40]. For this purpose the LA4782 plano-convex lens from Thorlabs was selected. This has a focal length of 500 mm, $\varnothing 2''$ clear aperture and is suitable for the 185 nm to 2.1 μm spectral range. The lenses are mounted on Thorlabs flip mounted so that they can be inserted and removed from the optical path remotely.

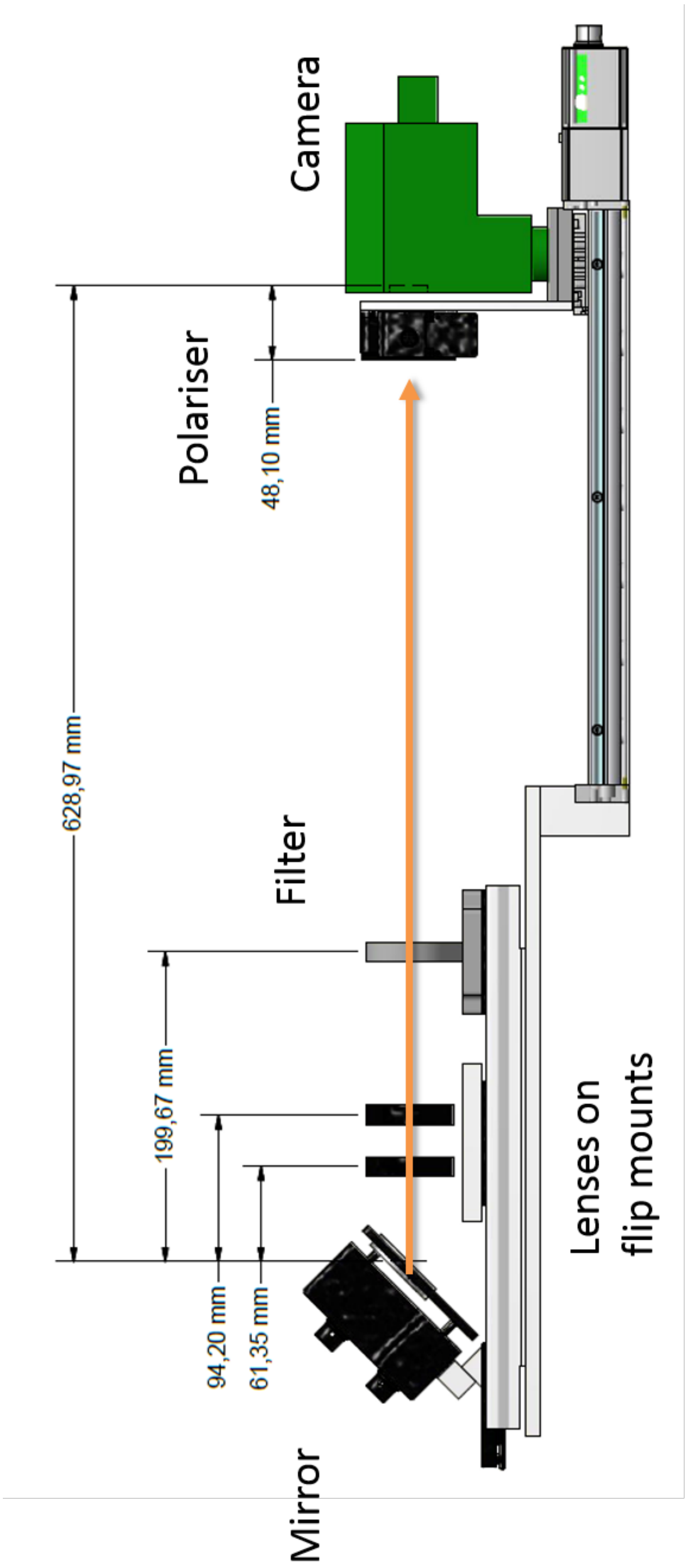

FIGURE 3.27: Technical drawing of the optical components positions (by J. Conway).

Bandpass filters select the wavelengths of interest. Initially, as shown in Figure 3.26(a) a filter wheel was included in the optical system. This allowed the filter in the optical path to be changed via remote control. An OWIS (FRM 40-4-D25-HSM) Filter wheel with ⌀1″ was chosen due to its compact size and the spatial constraints of the optical system. The filter wheel was later replaced by a ⌀2″ fixed mount seen in Figure 3.26(b). Narrowband filters with (10 ± 2) nm bandwidth from Andover Corporation were chosen at the wavelengths: 232 nm, 400 nm and 600 nm.

The vertical beam size information is encoded to the vertically polarised photons. Therefore a polariser must be included in the optical system. Two polarisers have been tested: a Glan-laser prism (440-2020-M2P) by Eksma Optics and a linear polariser (LPVISE100-A) from Thorlabs. The Glan-laser polariser is made of natural calcite with an operating wavelength range of 220 nm to 2.3 μm. The extinction ratio is $1 : 10^{-5}$. The linear polariser operates over the 400 nm to 700 nm wavelength range with an extinction ratio of $1 : 10^{-3}$.

The detector of the optical system is a gated intensified CCD (ICCD) camera ProxiKit Package by Proxivision. The Proxikit Package is a modular setup where each module is chosen to meet the experiment specification. The modules selected for the DR detector are as follows with specification values courtesy of Proxivision:

Multi Channel Plate (MCP) Image Intensifier (ProxiKit MOD M2562, M2582)

Due to an initial problem the M2562 was upgraded in Feb 2013 to the M2582 for which the specification is listed below. The purpose of the intensifier is to amplify low intensity signals. For the DR experiment weak signals are expected when the beam current is low. The spectral sensitivity of the image intensifier is shown in Figure 3.28.

Serial number: 22671
Input diameter: 25 mm
Type: MCP-PROXIFIER®with integrated power supply
Photocathode: Bialkali on quartz
Phosphor screen: P 43 on fibre optic
Gateability: 100 ns
Gain at 480 nm: 8080 W/W
Limiting resolution: 43 lp/mm

Pulse Generator (ProxiKit MOD μG 100 N)

The micro-pulse generator (μG) which is controlled by the μDCU operates the image intensifier with gateable photocathodes down to 100 ns. The gating unit operates using internal preset gating times or using an external Transistor-Transistor

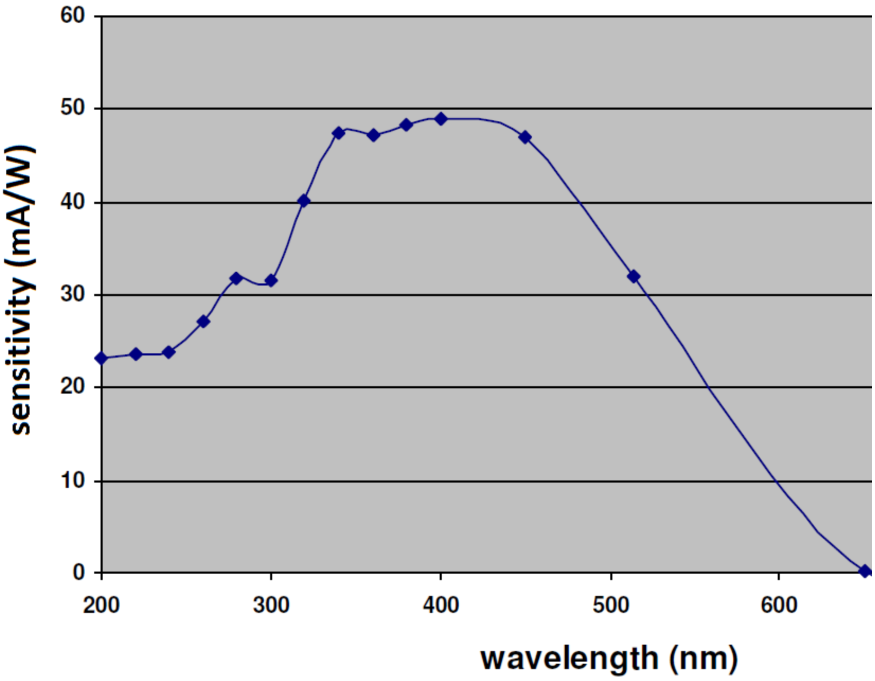

FIGURE 3.28: Spectral sensitivity of the M2582 intensifier (courtesy of Proxivision).

Logic (TTL) pulse where the gating time is defined by the pulse width. The gate can be configured to open on the positive or negative edge of the TTL trigger. The delay times for internal and external gate modes are 103.0 ns and 40.8 ns respectively. The external mode delay was measured by S. Mazzoni to be 49 ns. The maximum trigger frequency of the gating is 10 kHz.

Micro Digital Control Unit (ProxiKit MOD μDCU)

The μDCU controls the trigger mode setup of the μG and the gain adjustment of the intensifier via a system cable. The μDCU was originally designed for local operation only, where cables were pulled from the μG in the accelerator tunnel to the experimental area in the L3 spur. The system was later upgraded to allow remote control via an Ethernet interface box also provided by Proxivision.

CCD Camera Module, GigE (ProxiKit MOD C285FC GigE)

Figure 3.29 shows a block diagram of the camera module. To obtain beam size measurements using the angular distribution of DR the visibility (I_{min}/I_{max}) must be accurately measured. Therefore images must have a high spatial resolution and also a large dynamic range to identify the minimum and maximum intensities of the distribution. From previous DR experiments the dynamic range threshold was found to be $\geq$ 10 bit [11].

Type: AVT Manta G-145B; SN: 503328586
Fibre taper: 18 : 11
ADC: 14 bit
Pixel format: Mono12

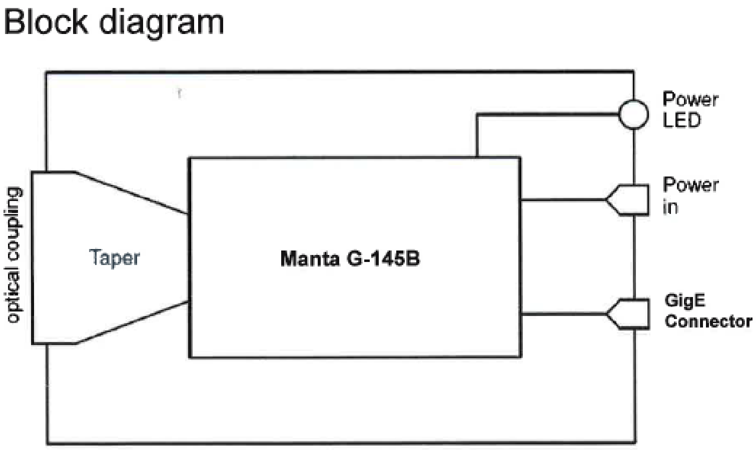

Figure 3.29: Block digram of the camera module (courtesy of Proxivision).

GigE Interface MAC: 000F314C78E6
Monochrome
1388 (H) × 1038 (V) active pixels
6.45 μm square pixels
16 frames/second triggered and continuous operation with full resolution
Programmable exposure from 33.4 μs to 60 s

The power supply of the camera was also modified to enable external triggering. This allows simultaneous triggering of the camera and intensifier for single-turn image acquisition.

The dimensions of the acquired images were in pixels determined by the size of the CCD sensor. For the angular distribution images it was necessary to know the conversion from pixels to mrad. The dimensions of a CCD pixel was 6.45 μm (horiz) × 6.45 μm (vert). An 18 : 11 fiber taper connected the intensifier window to the CCD sensor. Therefore the effective pixel size at the intensifier was 10.55 μm (h) × 10.55 μm (v). The angular resolution was calculated using

$$\Delta\theta = \frac{L}{d}, \tag{3.14}$$

where $L = 10.55$ μm is the effective pixel size and $d = 500$ mm is the distance from the planar (or bi-) convex lens to the intensifier i.e. the back focal plane distance. The resulting angular resolution per pixel $\Delta\theta$ was 0.0211 mrad.

3.5 Zemax

The Zemax Optical Design Program is a readily available commercial package which integrates all the features required to conceptualise, design, optimise, analyse and tolerance virtually any optical system. Zemax makes use of diffraction calculations to propagate a wavefront through an optical system surface by surface. In this way the wave-like nature of light is fully accounted for [59].

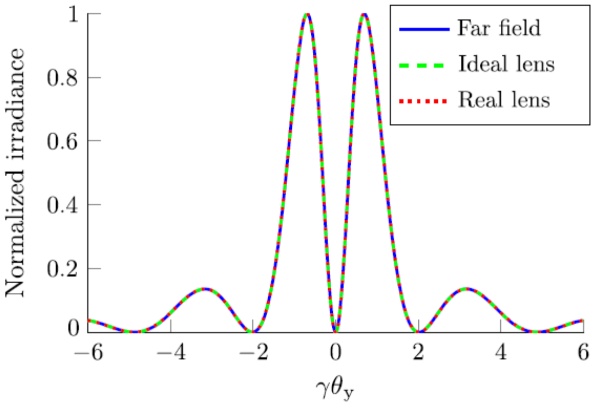

FIGURE 3.30: Comparison of the DR angular distribution in the far-field, in the back focal plane of an ideal lens and in the back focal plane of the plano-convex lens ($\lambda = 400$ nm, $\gamma = 4110$, $\theta_x = 0$, $a = \frac{\gamma\lambda}{2\pi}$) [59].

In this project, simulations from Zemax alongside those from the theoretical models were used to obtain predictions of the observations likely to be acquired with the given experimental setup. Initially the output from Zemax was checked against results from the ODR model. In Figure 3.30 an excellent agreement between the Zemax results from ideal and real lenses with the distribution from ODR model is seen.

The performance of the optical system could be evaluated. These simulations included both the spatial distributions of DR on the target surface and the angular distributions in the far-field as shown in Figure 3.31.

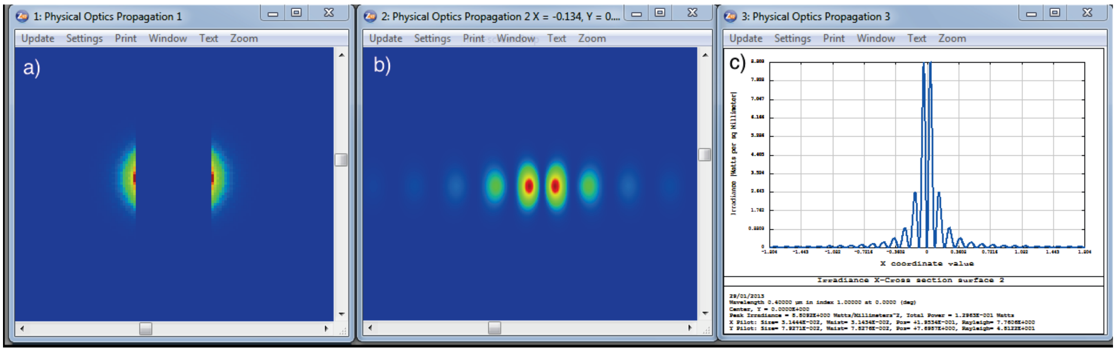

```
Irradiance X-Cross section surface 2

29/01/2013
Wavelength 0.40000 µm in index 1.00000 at 0.0000 (deg)
Center, Y = 0.0000E+000
Peak Irradiance = 8.8092E+000 Watts/Millimeters^2, Total Power = 1.2963E-001 Watts
X Pilot: Size= 3.1446E-002, Waist= 3.1436E-002, Pos= +1.9534E-001, Rayleigh= 7.7606E+000
Y Pilot: Size= 7.9271E-002, Waist= 7.5276E-002, Pos= +7.6957E+000, Rayleigh= 4.5122E+001
```

FIGURE 3.31: Zemax output: (a) source, (b) detector plane and (c) horizontal cross-section of the detector plane [60].

Using Zemax it was also verified that a compact optical system with the detector positioned in the prewave zone could acquire "far-field" angular distributions provided the detector was located in the back focal plane of the lens. In Figure 3.32 the far-field condition was established where a biconvex lens was used to remove all spatial information and transform the distribution at the detector plane into a purely angular one.

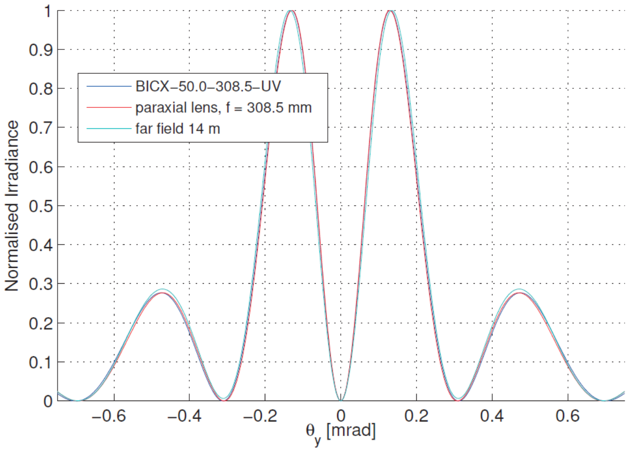

FIGURE 3.32: Comparison of the angular distribution in far-field condition, in the near-field using an ideal and also a real biconvex lens [60].

From the theoretical models Zemax provides the next step to linking theory with real observations from an optical system. By enabling a user defined DR source, the resulting angular distribution obtained after passing through the real optical system could be obtained. This not only provides more realistic expected results of the optical system but also provides a tool for relatively quick problem solving should the real data significantly deviate from those expected from simulations.

Chapter 4

Analysis of Experimental Conditions

The experimental conditions in a circular machine are significantly different to those on a linac. Due to the presence of bending magnets around the ring, the design of the DR monitor must aim to reduce the contribution of SR to beam size measurements. Furthermore, the beam must pass through the target with each revolution of the storage ring. Therefore the beam alignment and lifetime must also be carefully monitored.

4.1 Synchrotron Radiation Background

Synchrotron radiation is the name given to the electromagnetic radiation emitted when charged particles are radially accelerated. In storage rings SR is produced predominantly by bending magnets, undulators and wigglers.

The power radiated by an electron is given by

$$P_\gamma = \frac{1}{6\pi\epsilon_0}\frac{e^2 c}{\rho^2}\cdot\gamma^4, \tag{4.1}$$

where ϵ_0 is the permittivity of free space, e is the elementary charge, c is the speed of light, ρ in the bending radius and γ is the Lorentz factor. The mass of the electron is roughly 2000 times smaller than that of the proton and, therefore, for the same energy the electron has a γ that is approximately 2000 times larger. In Equation 4.1 it is found that the emission of SR depends on γ^4 such that the power radiated by an electron is roughly 16×10^{12} greater than that of a proton. In this equation it is also seen that the radiated power scales with radius of curvature ρ [38].

Substituting $\gamma^2 = E^2/m_0^2c^4$ in Equation 4.1 and given the classical electron radius defined as

$$r_e = \frac{e^2}{4\pi\epsilon_0 m_0 c^2} = 2.8179 \times 10^{-15} \text{ m}, \tag{4.2}$$

the radiated power may be expressed in terms of beam energy E as

$$P_\gamma = \frac{2}{3}\frac{r_e c}{(m_0c^2)^3}\frac{E^4}{\rho^2}. \tag{4.3}$$

This formula applies to an electron circulating in a synchronous orbit and shows how the power varies among synchrotrons of different energies and radii assuming that the electron is centred in the vacuum chamber [38].

The constant field formula describes the radiation of electrons of different energies E given a mean radius and field of the synchrotron. In this case the magnetic field B is constant and the bending radius ρ is a function of momentum given by

$$\frac{1}{\rho^2} = \frac{B^2e^2}{p^2} = \frac{B^2e^2c^2}{(pc)^2} \approx \frac{B^2e^2c^2}{E^2}. \tag{4.4}$$

Substituting Equation 4.4 into Equation 4.3, one obtains the result

$$P_\gamma = \frac{2}{3}\frac{r_e e^2}{(m_0c)^3}E^2B^2, \tag{4.5}$$

which shows the radiated power is proportional to the square of the particle energy and square of the magnetic field [38].

The Synchrotron Radiation Workshop (SRW) [61] program developed at the ESRF which runs in the IGOR interactive software environment was used to perform simulations of the SR incident on the target. SR is problematic in DR experiments because it is the main contributor to background. Since SR and DR are emitted from the same electrons, interference can occur. Depending on the intensity of SR incident on the target, thermal heating may lead to target deformation.

The SR background can be reduced by using a SR mask positioned upstream of the target. The choice of aperture size of the SR mask is a compromise between being small enough to effectively block the incident SR and also greater than the target slit size to avoid total destructive interference as discussed in Chapter 3 [12].

Element	Start location [m]	End location [m]	Bending radius [m]
B48W	372.247	376.234	140.63
Q48W	378.633	379.233	-
ODR detector	380.233 ± 0.1	-	-
Q49W	383.738	384.688	-
Q48E	389.219	389.819	-
B48E	393.191	396.136	140.63

Table 4.1: L3 straight section lattice components ordered in positron direction convention (reverse order for electrons).

Table 4.1 shows the beam line optics around the DR experiment location. The distance from the end of the soft bend magnet (B48E) to the DR target is approximately 13 m. Further upstream of the soft bend is the hard bend magnet. SR from the hard bend is not directly incident on the target but may be reflected by the beam pipe. A local bump can be used to steer SR from the hard bend magnet.

In SRW, the SR source was defined as a filament electron beam i.e. as a single electron with a user-defined beam current. The source was defined with coordinates as

$$\begin{pmatrix} x_0 \\ x'_0 \\ y_0 \\ y'_0 \\ E_0 \\ I_0 \\ s_0 \end{pmatrix} = \begin{pmatrix} 0 \\ 0 \\ 0 \\ 0 \\ 2.1 \\ 0.0011 \\ -3.0 \end{pmatrix} \tag{4.6}$$

where (x_0, x'_0, y_0, y'_0) are the transverse coordinates (position [mm] and divergence [mrad]) in phase space at the longitudinal position s_0 in metres, E_0 is the particle energy in GeV and I_0 is the current in A attributed to the single particle i.e. to model a single electron bunch.

The bending radius and magnet start/end locations in Table 4.1 were used to calculate the magnetic field strength and dipole length for the soft bend magnet B48E. Using the beam lattice information, SRW propagates the filament beam from the source to the observation plane. For simulations of the DR experimental setup the observation window was set to the target dimensions. It should be noted that the observation plane must be perpendicular to the incoming beam.

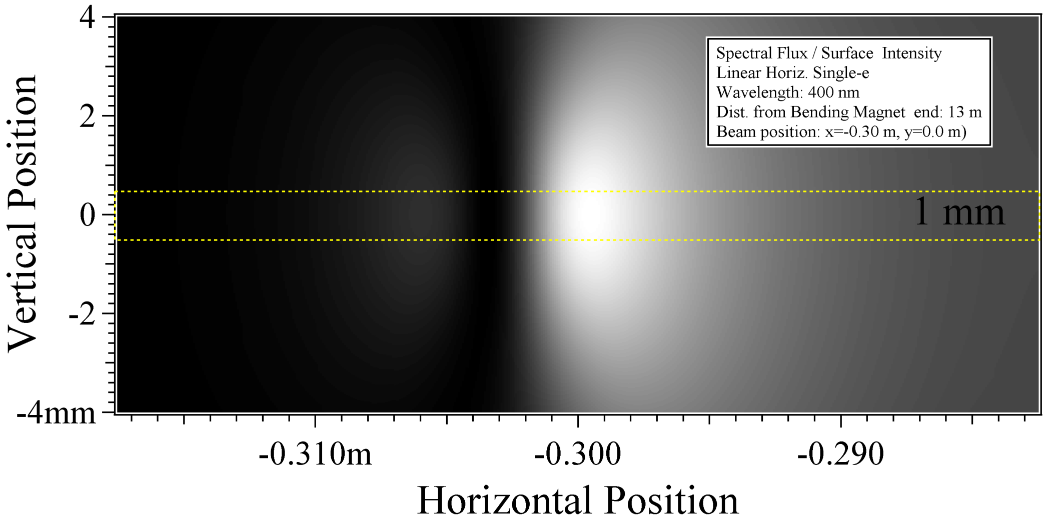

FIGURE 4.1: Horizontally polarised irradiance plot of synchrotron radiation on the target surface from the simulations in SRW.

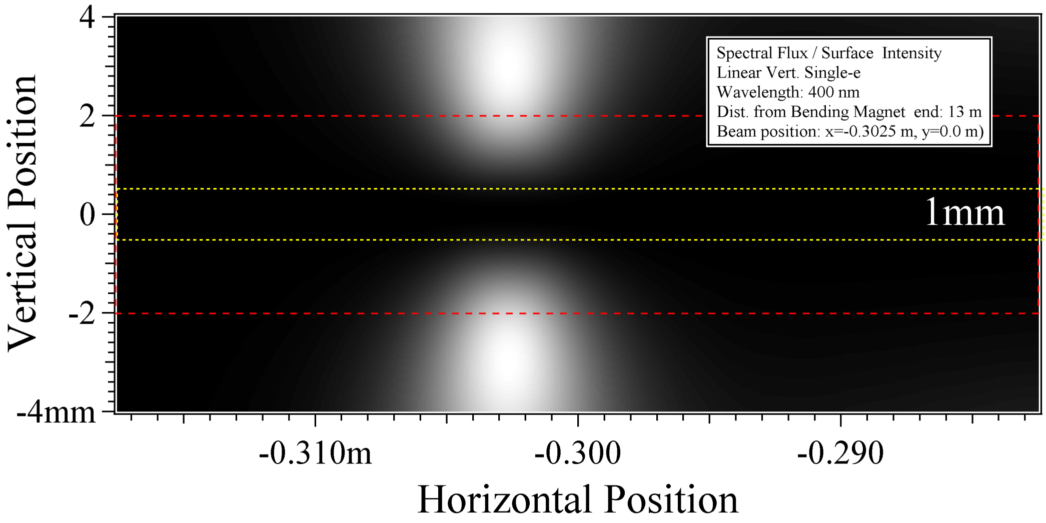

FIGURE 4.2: Vertically polarised irradiance plot of synchrotron radiation on the target surface from the simulations in SRW.

Figures 4.1 and 4.2 show the surface intensities at the DR target for polarised SR with 400 nm wavelength and 10% bandwidth. The yellow and red dashed lines indicate the positions of the 1 mm target and 4 mm mask apertures respectively. The filament beam position on the observation plane is $(x, y) = (-0.3025, 0.0)$ m. The spatial distribution of vertically polarised SR on the target surface is significantly different to that of DR.

In contrast to DR which decays exponentially from the target edge the intensity of SR increases with distance from the target edge as shown in Figure 4.3(b). Therefore in images of the target surface, DR can be identified from vertically polarised SR background. Furthermore these results show that a mask aperture size of 4 mm for a beam centred in the target aperture will block the majority of SR incident on the target surface.

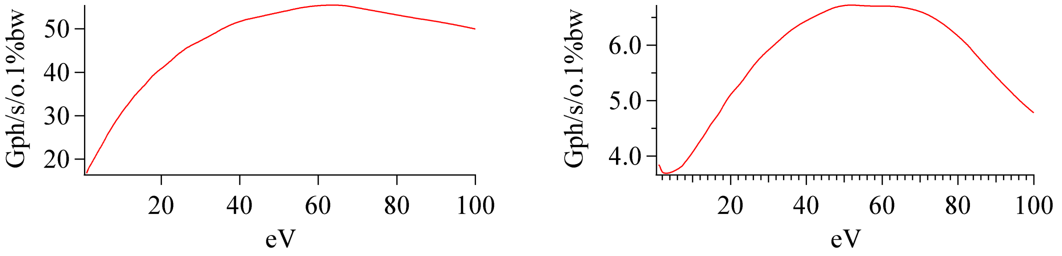

(a) Horizontal polarisation with 2.30315E10 photons/sec total intensity.

(b) Vertical polarisation with 4.31643E9 photons/sec total intensity.

FIGURE 4.3: SR spectra output from SRW for the horizontal and vertical polarisation components.

The energy spectra of the emitted SR was plotted in SRW for each polarisation component as shown in Figure 4.3. As expected from SR theory the total number of horizontally polarised photons is an order of magnitude greater than the vertical polarisation component. Therefore the inclusion of the vertically orientated polariser in the optical system will block a considerable amount of the SR background.

It is also observed that the peak energy is approximately 50 eV which is in the extreme UV spectral range. The corresponding wavelength of the peak energy is 25 nm. The remaining SR is further reduced by the narrow bandpass filters in the optical system. Furthermore the intensity of SR decreases with increasing wavelength. Thus the contribution of SR to the acquired images from the camera in the optical system is orders of magnitude lower than the amount incident on the DR target.

4.2 Commissioning using the Dummy Target

Commissioning of the DR monitor was done using a 1 mm dummy target. The dummy target did not have a mask positioned upstream nor an optically reflective finish to allow for beam size measurement using DR. The aim at this stage was to test all of the mechanisms, vacuum chamber and optical system that had been installed. Using the dummy target an alignment procedure for inserting the target around the beam trajectory was established. Furthermore direct images of the target surface provided information on the signal (DR) to noise (SR) ratio in the DR monitor location of the storage ring.

In Figure 4.4 the surface of the dummy target is shown. The image of the target was rotated with respect to the CCD sensor in the camera due to the mounting orientation of the optical system. For simplicity this was later modified such that the horizontal and vertical directions of the target were parallel with the dimensions of the CCD sensor. The incident SR was scattered across the whole surface area of the dummy target. It was planned that later target installations would include a mask upstream of the target,

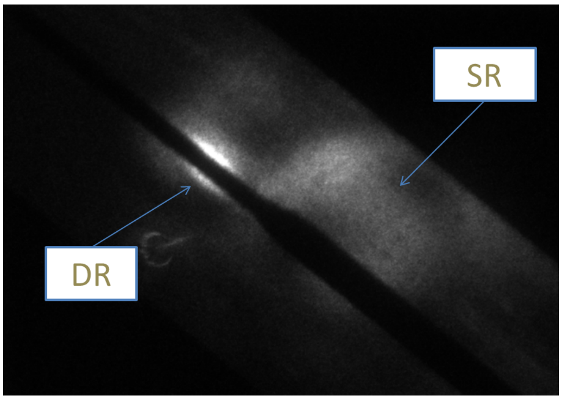

Figure 4.4: Image of the dummy target showing the regions of localised TR and SR on the slit edges and approximately uniform SR background at 400 nm wavelength.

the images acquired during the commissioning of the system reinforced the need for an upstream mask by providing a qualitative estimation of how much background could be removed from the final DR images. Although the surface quality of the dummy target was poor, the high intensity regions of DR were identified on the slit edges as expected.

4.2.1 Alignment Procedure

The procedure to align the beam with the target aperture required a combination of diagnostic instruments. Beam loss monitors (BLMs) positioned downstream of the target were used to detect the scattered electrons due to the scraping of the beam tails on the target aperture. A continuous readout BPM was used to measure the electron beam position as steers were applied. A beam current monitor combined with online beam lifetime calculation was used to monitor the beam alignment relative to the target aperture. When the beam was misaligned with the aperture, significant drops in beam current were observed. Lastly once the electron beam was within close range of the target aperture, direct imaging of the target surface using the camera in the DR optical system could be employed.

To determine the coarse vertical position of the dummy target aperture the target was rotated such that the incident electron beam was perpendicular to the target edge i.e. the largest target surface was parallel to the horizontal plane (or the beam orbit plane). A vertical bump was used to pass the beam above the target. The beam was gradually lowered to approach the target. The position at which significant losses were detected on the BLMs was recorded. The target was then retracted and the process repeated from below the target using the separation distance between the target and the mask. The centre of rotation of the target holder assembly is aligned with the target aperture centre. Therefore taking the average of these two vertical positions gave a coarse estimate of the vertical position of the target aperture.

The fine vertical position of the target aperture was found by inserting the target to a position at which losses could be detected on the BLMs. The beam was then swept vertically along the tips of the target tines. The vertical position at which the minimum scraping was observed was taken as the central position of the target aperture.

From the preliminary test it was found that $5-10$ minutes was lost for each beam injection and manual beam alignment. The downtime due to this turnaround was significant compared to the beam time available for data acquisition. For this reason a program was developed to automate this task. The functionality of this program included the machine checks for injection by reading parameters from the CESR database and ensuring they were within operation boundaries, initiating beam injection from the synchrotron to the storage ring, reading out BPMs and applying steers for the electron beam route into the target aperture and triggering a machine log file to be taken. The machine log file which takes a snapshot of the machine lattice and parameters is called a “CONDX” file. This process code reduced the turnaround time to approximately 2 minutes.

Initially the same manual beam alignment methods previously described were used to establish the route (vertical bump setting and target insertion position) into the target aperture. This route was then used as an input file for the program.

4.2.2 Target Imaging

Unlike previous DR experiments in addition to the analysis in the far-field using the angular distribution of DR, information may be obtained through the analysis of direct imaging of the target surface. Here we briefly present analysis of the shadowing effect observed on the target surface.

From a dummy target surface image a profile was selected and plotted against the expected intensity distribution using the vertical polarisation component of the DR electric field defined in Equation 2.17b. In Figure 4.5 the amplitudes of the data peaks are symmetric indicating the beam was well centred in the aperture. The data was observed to be much broader than expected from the theory. This broadening may have been due to the finite beam size used to acquire the data rather than a single particle used in the theoretical model, misalignment of the polariser allowing some horizontal contribution and parasitic light from SR background. It should also be noted that the dummy target had a rough surface causing photons to be scattered and therefore may also contribute to the peak broadening observed.

The data and theory were also compared to the simulated Zemax output for a single electron which suggested that the broadening was not due to aberrations from the optical system [60]. The exposure time of the camera was 15 ms (CesrTA revolution period $T = 2.56$ μs), therefore beam jitter although not observed on the BPMs could have also contributed.

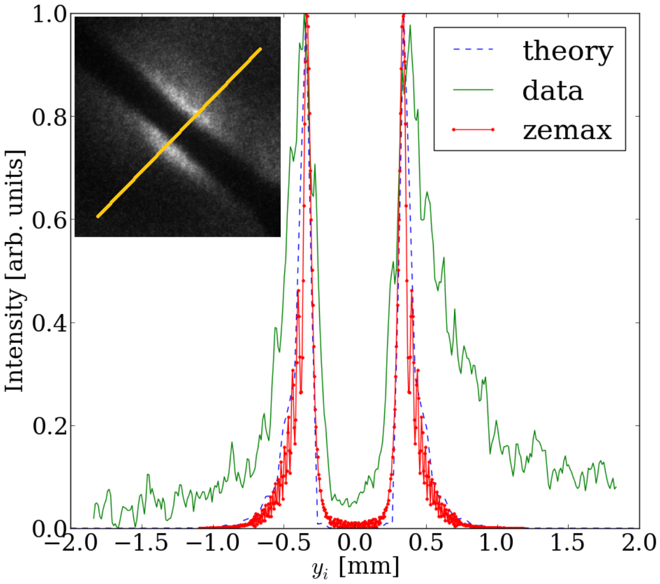

FIGURE 4.5: A plot of the intensity profile (solid line) and expected distributions from Equation 2.17b (dashed line) and Zemax (dash-dot line).

4.2.3 Beam Lifetime

For DR beam size measurement a target must be positioned close to but not impeding the charged particle trajectory. The interaction of the electric field of the charged particle with the atoms of the target is dependent on the the distance between the particle and the target edge. In a circular machine, the charged particle beam must pass through the target aperture millions of times. Therefore any excitations caused by the target on the beam will be cumulative. From this reasoning it was expected that the insertion of the target to the beam would cause some drop in beam lifetime.

The target and mask were mounted on a target mechanism with translation and rotation degrees of freedom. The translation of the target was recorded in computing units [cunits] where $\approx$ 200 cunits = 1 mm. In Figure 4.6 the positions of interest of the target and mask relative to the beam are shown. In this schematic the target is inserted from left to right. At 26600 cunits the beam passes through the wide aperture of the mask where the ODR model is applicable. At 28400 cunits the beam passes through the narrow aperture of the mask where inference effects must be considered and the ODRI model is used.

The beam lifetime at CesrTA for the 0.5 and 1.0 mm target apertures was 2 - 3 minutes. The vertical beam size was varied from 13 – 52 μm. The horizontal beam size was approximately 490 μm. The beam lifetime was not affected by the vertical beam size until σ_y = 50 μm where it could then be regained by manually adjusting the vertical beam position in the slit using target imaging.

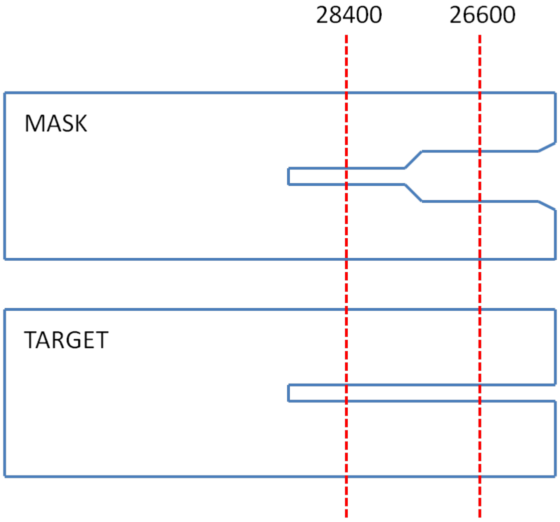

Figure 4.6: A schematic to indicate the mask and target positioning for ODR (zero interference) and ODRI (interference) studies at target translation positions of 26600 cunits and 28400 cunits respectively.

At the beginning of each shift a fast logger was initiated. This logged a series of parameters at a frequency of 1 Hz from the CESR database. Figure 4.7 shows the beam current and target translation position data recorded by the fast logger during a shift. In Figure 4.7(b) a shorter time span is plotted so that features are more easily identifiable. Here we see that with the target retracted the rate of beam current loss with time was approximately -0.66 mAhour^{-1}. It is also seen that the beam current loss rate is constant until the target reaches the ODR measurement position at 26600 cunits where a sharp drop-off in beam current is observed.

At the ODRI measurement position of 28400 cunits the beam lifetime was significantly reduced to approximately 0.5 minutes. Therefore it was extremely important for the beam alignment and target insertion to be automated as much as possible and to avoid losing a large proportion of the bunch charge. The final centering in the target aperture was done using manual adjustment of the vertical beam position.

Initially it was thought that higher order modes (HOMs) were being excited due to the presence of the target holder and support arm inside the comparatively large vacuum chamber. Depending on the wakefields, the beam lifetime could be inhibited due to head-tail oscillations or beam orbit deflection due to the tilt of the target with respect to the incoming electron beam. A beam orbit deflection was quickly disregarded since this would be observed over many turns of the synchrotron on the BPMs. The possible head-tail oscillation was less trivial to verify. It is known that wakefields are dependent on the charge of the single electron bunch. Therefore the beam lifetime should improve with decreasing charge per bunch. The 1 mA single bunch was changed to a 10 bunch train with a total beam current of 1 mA. No improvement in beam lifetime was observed

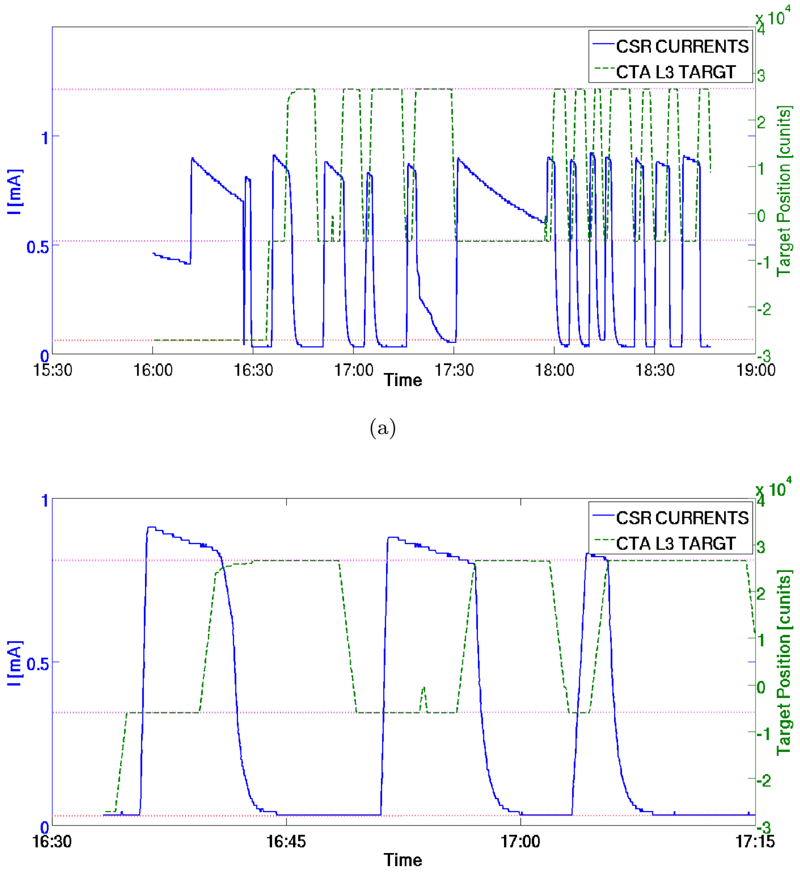

(a)

(b)

FIGURE 4.7: Fast log data of beam current and target translation position (a) and a zoomed in section (b). The red dotted line at target position −27113 cunits denotes the position where the target is fully retracted from the vacuum chamber. The purple dotted line at −6000 cunits denotes the standby position. The target must be retracted to the limit switch at this position for injection. At this position the target is safely retracted at the edge of the vacuum chamber. At 25800 cunits the target is located next to the beam. The position at 26600 cunits denotes the ODR measurement position of the target. The pink dotted line at 28400 cunits is the ODRI measurement position.

when operating at the lower charge per bunch mode. Thus it was unlikely that wakefield effects were the dominating process limiting the beam lifetime.

Beam scraping on the target aperture could also limit the beam lifetime. As the tails of the beam are scraped away, electrons from the core of the beam must take up positions in the tail and hence then be scraped away on the next revolution of the machine. With this hypothesis it would be expected that by reducing the vertical beam size in a given target aperture, the beam lifetime should improve. As aforementioned, no significant change in beam lifetime was observed at different beam sizes.

Here I refer to the work done by Mike Billing et al. at CesrTA to further investigate the vertical beam tails of the electron beam. At position 43W in the storage ring (see Figure 3.1), top and bottom vertical scrapers were inserted individually whilst measuring the beam lifetime. Downstream of the vertical scrapers photomultiplier tubes

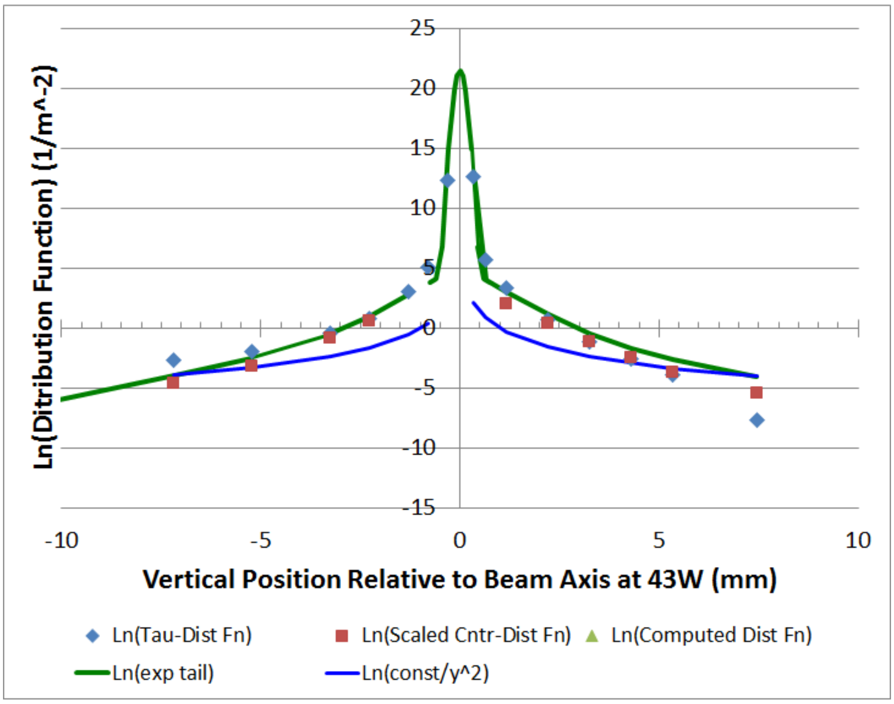

FIGURE 4.8: The vertical electron beam profile obtained by Mike Billing et al. by the vertical scraper investigation.

(PMTs) were used to simultaneously monitor the radiation due to the interaction with the scrapers. The counting rate of hits on the detector was read out and correlated with the beam lifetime. Scaling was then performed on the vertical beam size at 43W to obtain expected results for the DR monitor location at 48W in the storage ring. The main result of this study was a greater understanding of the vertical profile of the electron beam as shown in Figure 4.8. The core of the beam is well described by a Gaussian profile however the beam tails exhibit exponential behaviour.

In addition to beam scraping due to the beam tails given the vertical beam size, it was thought that the beam lifetime could also depend on the roll of the beam in the target aperture. Due to the large aspect ratio ($\sigma_y : \sigma_x$) of approximately $1 : 38$ if the horizontal axis of the beam was not parallel with the target aperture, significant beam scraping could also occur. This was also investigated by changing the skew of the beam in the target aperture, which could be monitored using direct imaging of the target surface. Again no improvement in the beam lifetime was observed.

For a non-invasive DR monitor the beam lifetime is a crucial parameter. In this section investigations have shown that with the current experimental setup, the reduction in lifetime predominantly due to scraping of the beam tails, could not be regained through transverse position and roll alignment of the beam in the target aperture. Increasing the target aperture size would be one way to improve the beam lifetime at the cost of lower DR intensity. Redesigning the mask and target assembly so that it does not need to be inserted so far into the beam could be another option.

Chapter 5

Experimental Results and Discussion

In this Chapter the results of the feasibility study for beam size measurements using DR on circular machines are presented. Although most of the commissioning of the DR monitor was described in the previous Chapter, such as the beam based alignment with the dummy target, the optimisation of the optical system was performed later and therefore is included here. Results were obtained using a single bunch electron beam of 1 mA beam current and 2.1 GeV beam energy. The typical errors associated with the results arise from the pixel shot noise of the image acquisition which scales as the square root of the image intensity and tends to follow a Poisson distribution. The results may be considered in three parts: direct surface imaging, ODR model analysis of the angular distribution and finally ODRI model analysis of the interference between the mask and target.

5.1 Observation of ODR at CesrTA

5.1.1 Vertical Polarisation Alignment

A comparison of the target surface images for horizontal and vertical polarisation components is shown in Figure 5.1. Through direct observation of the target surface it can be seen that the contribution of SR background is significantly greater for the horizontal polarisation. The diffraction rings observed in the SR distribution indicate that not all of the SR is directly incident on the target surface. Some of the SR may be reflected from bending magnets further upstream.

During the installation of the polariser in the optical system, the vertical polarisation was known to be within the range of 90 to 110 deg. To accurately determine the vertical

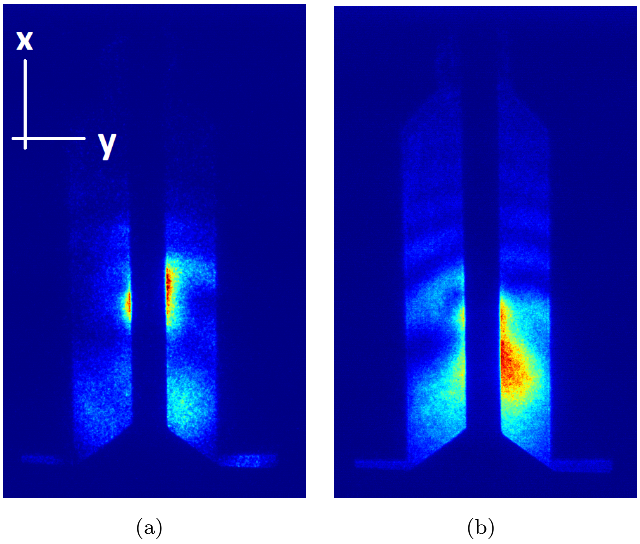

(a) (b)

FIGURE 5.1: Target surface images of the (a) vertical polarisation at 95 deg. and (b) horizontal polarisation at 180 deg. Note that the target images are rotated by 90 deg due to the spatial constraints of the imaging system: x-direction is parallel and y-direction is perpendicular with respect to the target tines (slit edges).

polarisation orientation within this 90 to 110 deg a polariser scan was performed and target surface images were acquired at different polariser orientations. In target imaging the DR source was identified as two bright spots on the slit edges. These two bright peaks along the slit edges changed in position along the slit edge with rotation of the polariser. Based on the assumption that the horizontal axis of the beam was parallel with the horizontal axis of the target i.e. the slit edge, the vertical orientation of the polariser should be at the orientation where the two bright spots on the slit edges were vertically aligned.

By drawing a line between the peak intensities of the two bright spots on the slit edges a tilt angle relative to the vertical axis of the target was obtained. The vertical axis is perpendicular to the slit edge. This tilt angle was recorded for each polariser orientation of the scan. At the vertical polarisation position, the tilt angle between the centroids on each slit edge should be zero i.e. the two centroids are vertically aligned. Provided that the horizontal plane of the beam is parallel with the target edge, this method provides a more accurate way to distinguish the vertical polarisation position using target imaging.

Figure 5.2(a) shows the polarisation scan taken during the December 2013 test where the red curve is an arbitrary polynomial fitted for guidance purposes only. The vertical and horizontal components correspond to the zero crossing polarisation positions. Since the vertical polarisation direction was known to be approximately 90 deg, the zero crossing near this value is the vertical polarisation component.

From the December 2013 scan, the vertical polarisation component was found to be at a polariser position of (93 ± 5) deg. This range was confirmed by the polariser scan taken

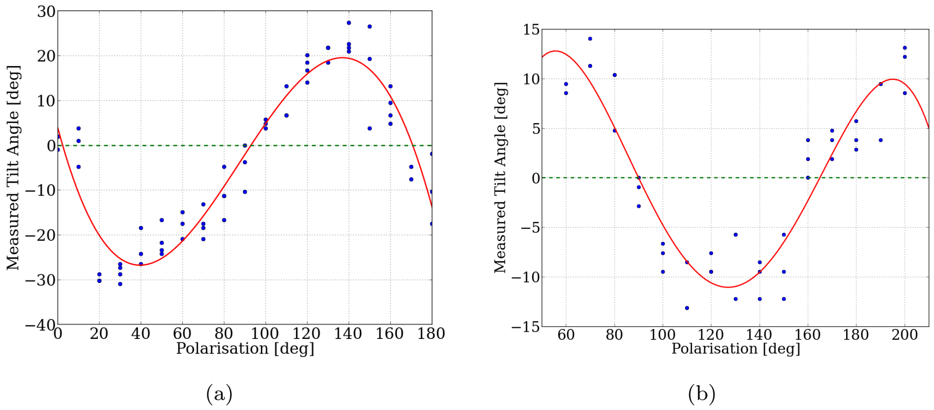

Figure 5.2: Polarisation scans taken in (a) December 2013 and (b) April 2014.

during the April 2014 beam test. In Figure 5.2(b) the polariser position corresponding to the vertical component was found to be at (90 ± 5) deg.

Based on these results and through direct observation of the DR signal relative to background, a polariser orientation of 95 deg was generally chosen as the vertical polarisation component position.

5.1.2 Beam Alignment in the Target Aperture and Beam Position Sensitivity

An image of the molecular adhesion target surface is shown in Figure 5.3. The electron beam is not fully inserted in the target aperture. At 600 nm wavelength, a significant reduction in the SR background across the surface of the target was observed. Therefore as expected, a better signal to noise ratio was achieved by operating at longer wavelengths.

Direct imaging of the target surface provided a means to accurately align the electron beam with the centre of the target aperture. The image sequence in Figure 5.4 shows the 0.5 mm target insertion. It is observed that although the mask positioned in front of the target blocks the majority of SR, a non-negligible proportion still passes through the mask aperture onto the target surface. Furthermore, for the particular target/mask assembly shown in Figure 5.4, the target is slightly longer than the tines of the mask, thus there is an additional contribution to background.

In target imaging the SR is seen as a uniform intensity on the target surface. The signal from DR is observed as a bright disc surrounding the electron beam. The horizontal position (in the direction parallel with the target tines) of the electron beam is fixed. DR theory states that the DR intensity decays exponentially from the slit edge. By taking the profile of the target image, the unique exponential feature of DR, which cannot be attributed to SR, can be seen. In Figure 5.5 the DR signal verification using the exponential fitting tool in LabView is shown. Once the DR signal was verified the beam

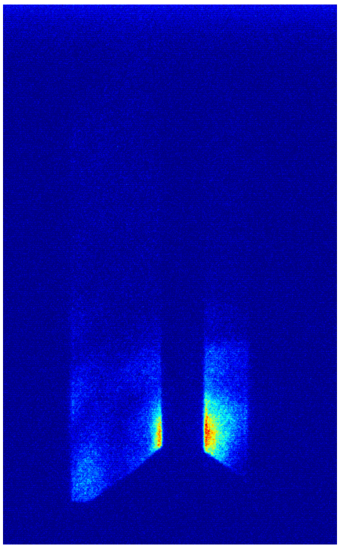

Figure 5.3: An image of the coated glass molecular adhesion target: 1.0 mm target aperture, 4.0 mm mask aperture, 600 nm wavelength and 21 μm vertical beam size as measured by the xBSM.

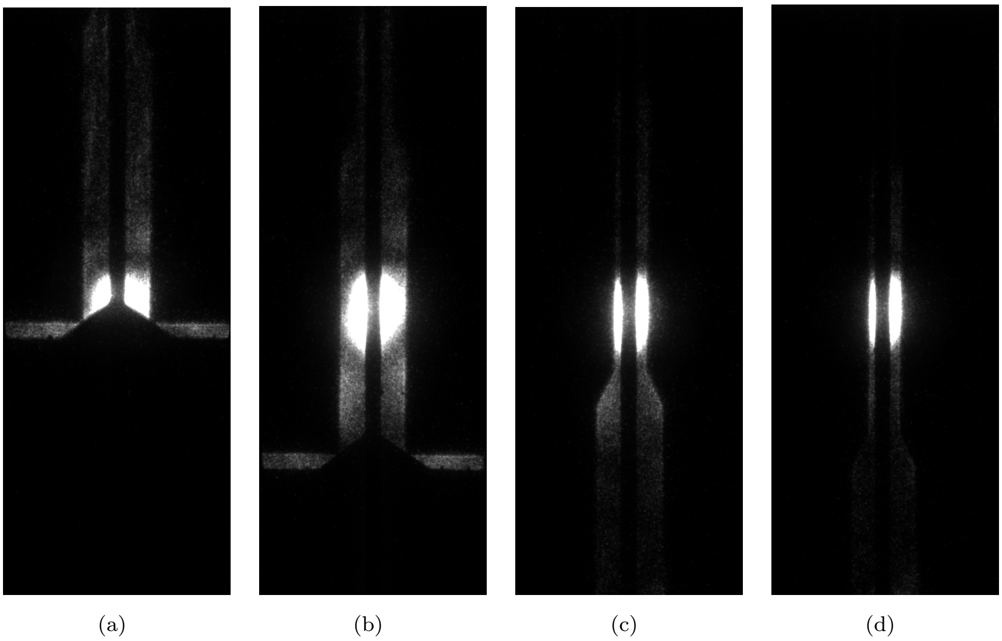
(a) (b) (c) (d)

Figure 5.4: Image sequence (a), (b), (c) and (d) showing the insertion of the target and alignment of the beam with the aperture. Due to the orientation of the optical system the images are rotated by 90° i.e. the horizontal plane along which the target is inserted is parallel with the target tines and the width of the target aperture is in the vertical plane.

was aligned to the centre of the target aperture by balancing the peak intensities on each tine of the target.

Using the target imaging model, the distribution across the target surface for a beam centred in the target aperture could be investigated. In Figure 5.6 a line profile for a

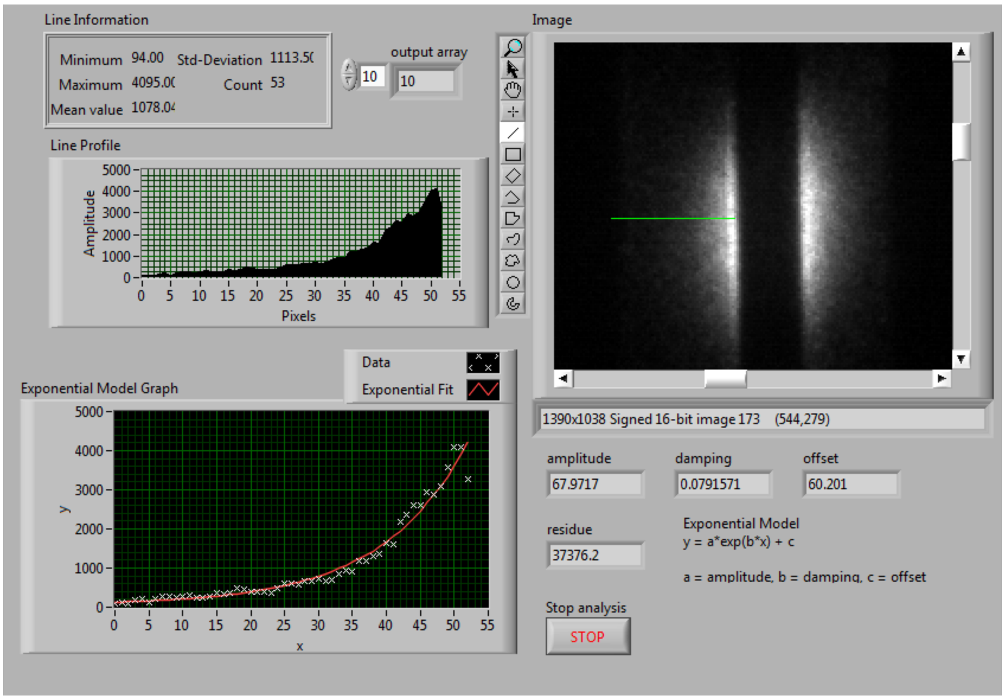

Minimum 94.00
Std-Deviation 1113.5
Maximum 4095.0
Count 53
Mean value 1078.0
output array 10 10
1390x1038 Signed 16-bit image 173 (544,279)
amplitude 67.9717
damping 0.0791571
offset 60.201
residue 37376.2
Exponential Model
y = a*exp(b*x) + c
a = amplitude, b = damping, c = offset

FIGURE 5.5: DR verification by fitting the exponential intensity decay from the target edge.

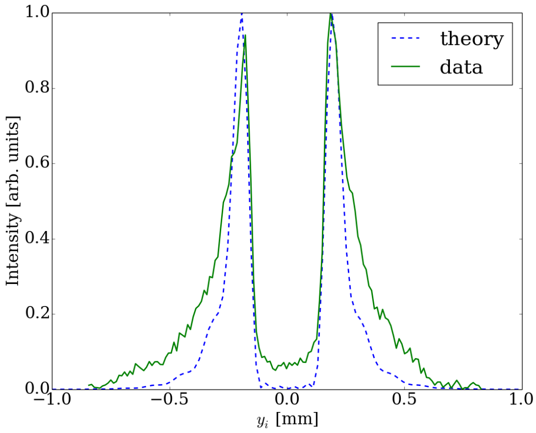

FIGURE 5.6: A fit of the normalised line profile from the 0.5 mm molecular adhesion target surface for a beam relatively well centred in the target aperture.

beam in the 0.5 mm aperture is shown. The peaks of the distribution are relatively symmetric indicating the beam was well centred in the aperture. However, upon comparing the data with the expected distribution from the target imaging model it is seen that the data is broader than predicted for a pure DR signal. This broadening is another indication of the SR background contribution. The non-zero intensity in the target aperture for the data distribution is background scattered from the vacuum chamber.

5.1.3 Shadowing of the Electromagnetic Field

Within the DR monitor at CesrTA, the mask and target are mounted to a common holder as shown in Figure 5.7. The separation distance between the mask and target is 15.5 mm. As described in Chapter 1 an observable interference effect occurs if the condition $a_1 \geq 4a_2$ is not satisfied where a_1 is the mask aperture size and a_2 is the target aperture size. In this case, shadowing may be observed on the target surface.

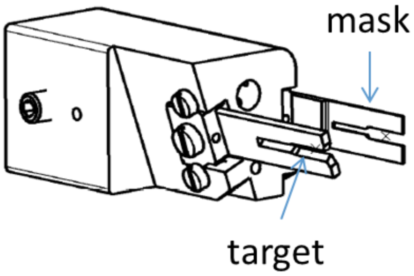

FIGURE 5.7: Schematic of the mask and target assembly.

The formation zone L_f (see Equation 2.13 in Chapter 1) is the region behind the aperture through which an electron has passed. In this region the Coulomb field of the ultra-relativistic ($\gamma >> 1$) electron and the forward DR (FDR) from the aperture cannot be measured separately [62]. There are two points of view to describe shadowing: for convenience we will refer to them here as the optical view and the Coulomb field view.

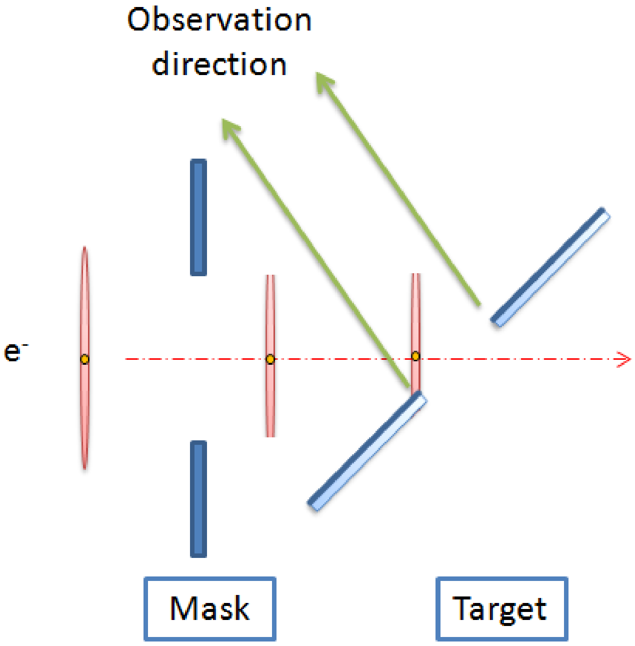

FIGURE 5.8: Shadowing of the Coulomb field.

In the Coulomb field point of view, the electric field associated with the electron beam is considered to consist of quasi-real photons. If we consider the case shown in Figure 5.7, the first aperture through which the beam passes is the mask. Scattering of the Coulomb field by the mask gives rise to DR. Since the mask does not have a reflective surface this is predominantly FDR. Positioned downstream, the target is in the shadow of the mask. Thus it emits almost no radiation. The Coulomb field is gradually "repaired" in the formation zone [62].

The shadowing effect can also be described using the optical point of view. In this case, shadowing appears as a destructive interference effect between the Coulomb field and the FDR [62]. Alternatively, this destructive interference can be considered as the cancellation of FDR from the mask with BDR emitted by the target.

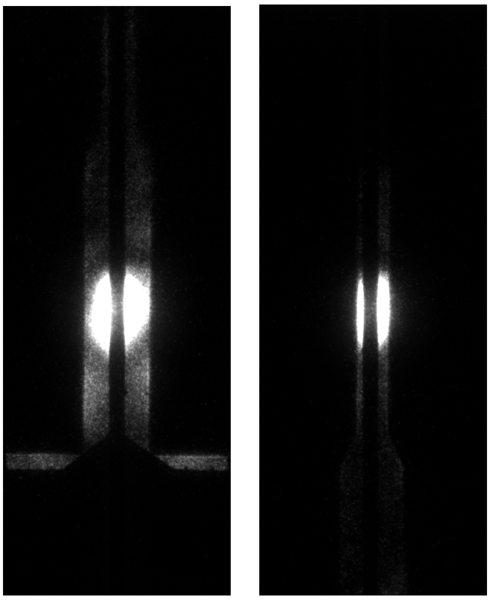

(a) (b)

FIGURE 5.9: Images of the 0.5 mm target surface: (a) with negligible shadowing from a 2 mm mask and (b) with significant shadowing from a 1 mm mask where $\lambda = 600$ nm.

In Figure 5.9 images of the target surface for different mask apertures are shown. In Figure 5.9(a) negligible shadowing was observed and the measured radius of the illuminated DR disc in the vertical direction (perpendicular to the target edge) was 0.96 mm. The effective field radius for an electron $r_e \approx \gamma\lambda/2\pi$ given $\gamma = 4110$ and $\lambda = 600$ nm was 0.4 mm. A factor of two difference is obtained between the calculated and measured radii of illumination of the DR disc in the vertical direction.

Figure 5.9(b) shows significant shadowing. The vertical width of the illuminated region has reduced from $2 \times 0.96 = 1.92$ mm to 1 mm defined by the mask aperture. Here the reader should note the significance in this observation of clear evidence of the shadowing effect on the target surface. The mask is separated from the target and the optical system is only imaging the target surface. Therefore although it is expected that SR cannot extend into the shaded regions of the target due to being blocked by the mask positioned upstream, DR emitted by the target should not have this boundary that is clearly observed.

5.2 ODR Angular Distribution Measurements

5.2.1 ODR Angular Distribution and Comparison with Theory

In Figure 5.10 the angular distribution from the molecular adhesion target is shown. The upper portion of the image showed the expected vertical polarisation distribution of DR. The unfocussed light in the lower portion of the image was thought to be SR. To further verify whether the upper portion was a true DR signal a comparison was made between the data and theoretical models.

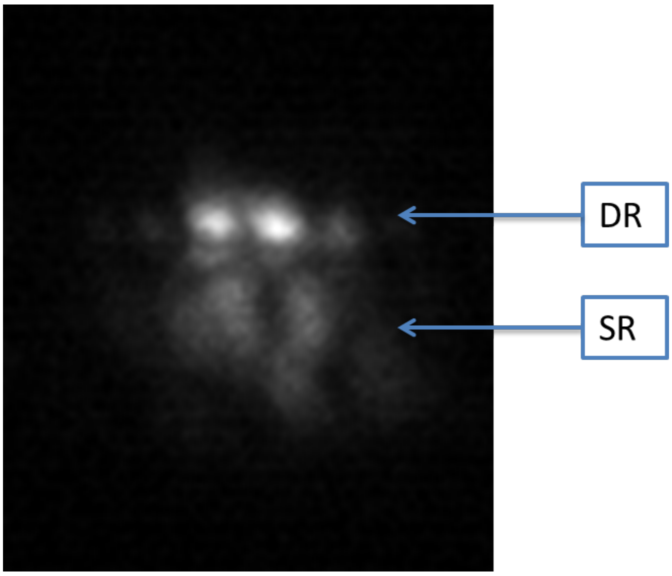

FIGURE 5.10: The DR angular distribution image of the coated glass molecular adhesion target: 1.0 mm target aperture, 4.0 mm mask aperture, 600 nm wavelength and 21 μm vertical beam size as measured by the xBSM.

The comparisons of the data with the ODR (see Equation 2.12) and ODRI models (see Equation 2.16) are shown in Figures 5.11 and 5.12 respectively. From the design of the optical system it was expected that 1 pixel = 0.0211 mrad. However to fit the central lobes of the data with the theoretical models this conversion had to be adjusted to 1 pixel = 0.0350 mrad. The modification of the pixel to angle cablibration fact worsened the alignment of the side lobes. The reason for this was expected to be due to interference with residual SR.

In Figure 5.11 the asymmetry could not be accounted for in the ODR model. Thus to fit the visibility i.e. the central minimum of the distribution, the best result was obtained using a beam size of 22.5 μm.

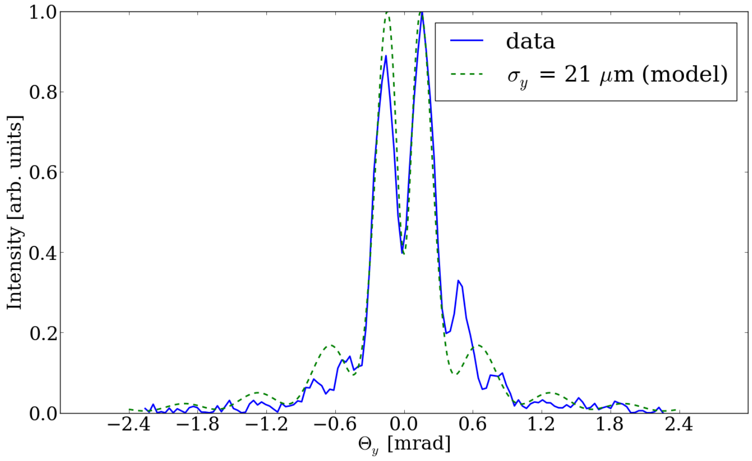

FIGURE 5.11: Comparison of the DR angular distribution with the ODR model: 1.0 mm target aperture, 4.0 mm mask aperture, 600 nm wavelength and 21 μm vertical beam size as measured by the xBSM.

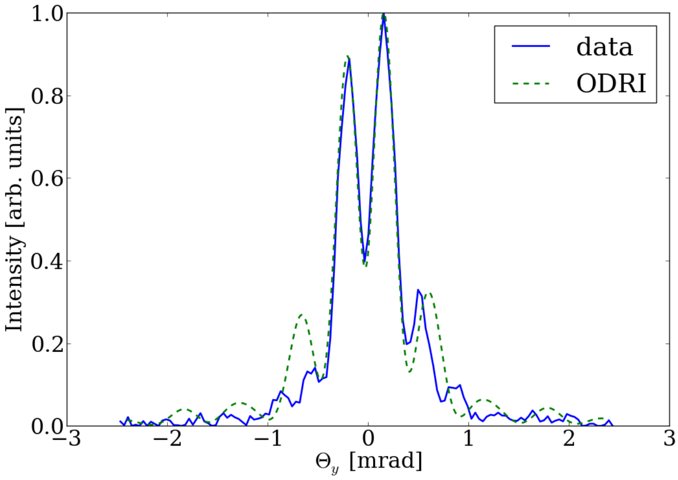

FIGURE 5.12: Comparison of the DR angular distribution with the ODRI model: 1.0 mm target aperture, 4.0 mm mask aperture, 600 nm wavelength and 21 μm vertical beam size as measured by the xBSM.

In the ODRI model, the asymmetry between the central lobes was accounted for by including a 40 nm offset between the non-coplanar tines of the target. This value was consistent with those reported in the fabrication and metrology reports for the molecular adhesion targets (see Chapter 3). To try to improve the fit with the ODRI model, estimations were made into the beam divergence however the change was negligible.

5.2.2 Back Focal Plane Alignment

Using angular distribution images taken over a scan of the longitudinal camera position on the linear translation stage the position of the back focal plane (BFP) was measured.

It is known that in the back focal plane, the horizontal peak width and the vertical peak separation should be at a minimum. In Figure 5.13 the minimum horizontal lobe widths were measured and plotted. The BFP was found to be at the linear translation stage position of (48 ± 2) mm.

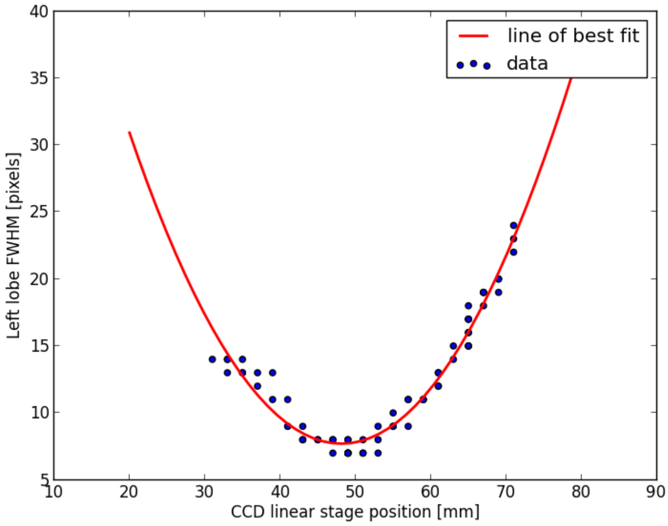

FIGURE 5.13: Measurement of the back focal plane using a linear translation stage scan.

5.2.3 Beam Size Effect and Analysis

The angular distribution of DR for the non-interference setup using 0.5 mm target and 2 mm mask is shown in Figure 5.14. As expected, the central lobes have a higher intensity compared to the side fringes which are just visible.

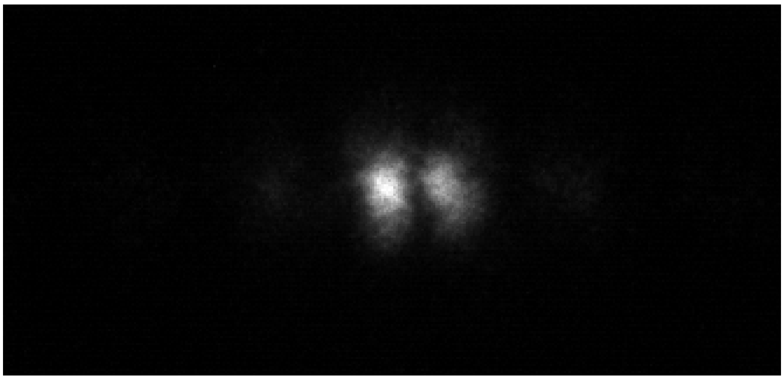

FIGURE 5.14: An example of the DR angular distribution: $\lambda = 600$ nm, 0.5 mm target and 2 mm mask.

The visibility (I_{min}/I_{max}) of the DR angular distribution is sensitive to beam size. As described in Chapter 1, the visibility can be measured from the central line profile or vertical projection of the angular distribution. The xBSM was used as the reference beam size monitor from which we could compare the DR monitor measurements. A variety of beam sizes were measured at 400 and 600 nm wavelengths. From DR theory it is known that the sensitivity to beam size scales inversely with wavelength.

In Figure 5.15 the beam size sensitivity is illustrated. The visibility of the vertical projections at 45 μm beam size were larger than that at 17 μm as expected. The 45 μm line profile with a known beam offset relative to the target centre also had a greater visibility than that of the centred beam. Thus in Figure 5.15 the ambiguity and contribution due to beam offset in the target aperture to the beam size measurement can be observed. Here, it should be noted that although the beam offset was observed from the target images, it could not be quantified.

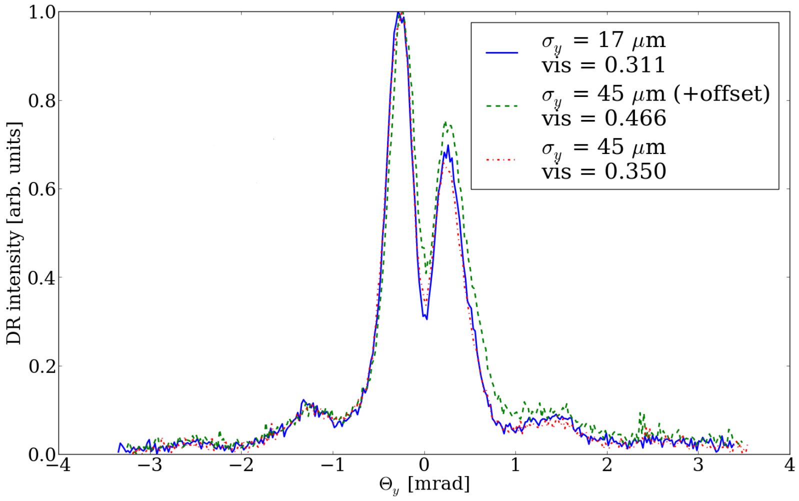

FIGURE 5.15: A comparison of projected vertical polarisation components (PVPCs) for different beam sizes.

Using the ODR model and PVPC technique, the expected visibility curve was simulated. Given a 600 nm wavelength and 0.5 mm target aperture size, for each beam size in the range 0 to 50 μm the angular distribution was simulated. From each angular distribution the PVPC was obtained and the expected visibility for each beam size was recorded. The resulting expected visibility curve is shown Figure 5.16 (blue line). The theoretical visibility curve assumes a zero background contribution thus the curve passes through the origin.

The expected theoretical visibility curve in Figure 5.16 was then fitted using the method of least squares with Equation 5.1 to obtain the coefficients a_0, a_1 and a_2. The coefficient a_0 defines the crossing point on the visibility scale. The fitted coefficients of the expected visibility curve were : $a_0 = 0.0$, $a_1 = -15.49$ and $a_2 = 2.130 \times 10^7$.

$$R = a_0 + a_1\sigma_y + a_2\sigma_y^2 \tag{5.1}$$

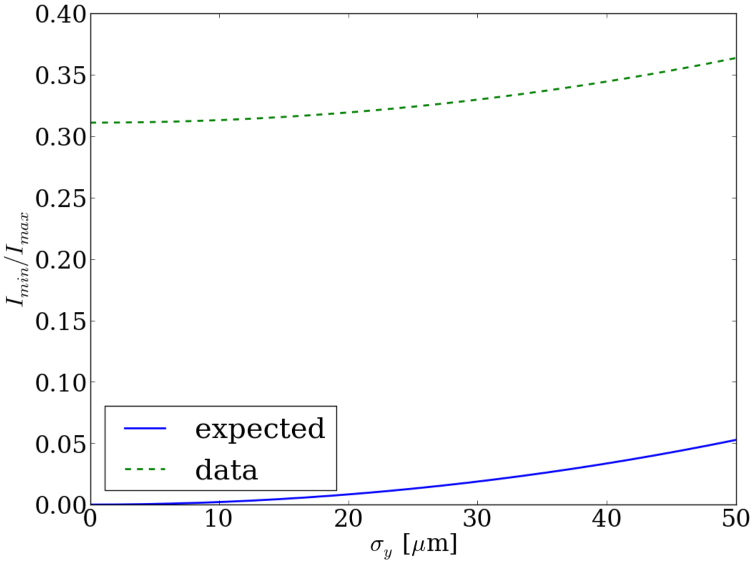

FIGURE 5.16: Expected (blue line) and measured (green dashed line) visibility curves for 0.5 mm target and 600 nm wavelength.

For real data measurements there will be some background contribution to the DR signal image. Thus a_0 will be larger than zero. Using the angular distribution from the real data at 17.6 μm beamsize an estimation of the background offset was determined. From the theoretical curve in Figure 5.16 it is seen that there is a very small difference in visibility between 0 μm and 17.6 μm beamsize. Thus this estimation assumes that the background level is approximately the same as the measured visibility at 17.6 μm which was 0.311 for the particular image that was analysed. Therefore to obtain an estimation of the real visibility curve from the data, the 0.311 background was added to the theoretical curve obtained from the simulation.

The difference in visibility between 17.6 and 45 μm beamsize using the ODR model simulation was 0.034. The difference in visibility between 17.6 and 45 μm beamsize using from the real data was 0.039 i.e. almost the same as expected from the theoretical model. Therefore in Figure 5.16 it was a reasonable assumption that only the background offset parameter a_0 in Equation 5.1 needed to be adjusted to 0.311 for the estimated visibility curve of the real data.

To obtain a more accurate representation of the measured visibility curve at 600 nm wavelength the average visibility data points at 17.6 and 46.2 μm beamsize were measured. To obtain the average data points, multiple images at each beam size were analysed using the ODR with PVPC technique. These average data points denoted by green circles are shown in Figure 5.17 where the errorbars denote the standard error for each mean value.

The average visibility data points for 17.6 and 46.2 μm were 0.2978 and 0.3380 respectively. As aforementioned, since the real data trend followed the quadratic gradient

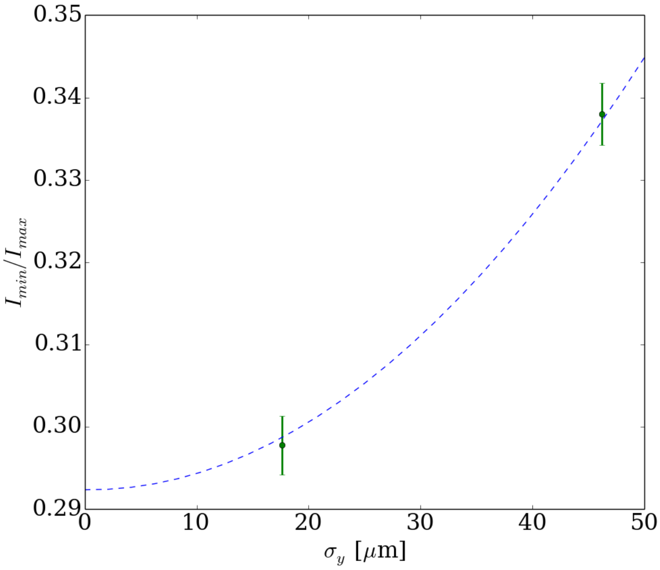

FIGURE 5.17: Resultant visibility curve at 600 nm wavelength and 0.5 mm target aperture from a least squares fit of the average visibility (green circles) at two beam sizes.

expressed by the expected theoretical curve the coefficients from the fit of the theoretical curve of with Equation 5.1 were applied to the real data. Therefore given the average visibility data points of the real data and the fixed coefficients $a_1 = -15.49$ and $a_2 = 2.130 \times 10^7$ a least squares fit was performed to obtain an accurate value for a_0.

In Figure 5.17 the visibility curve from the least squares fit of the data is shown by the blue line. Here the background offset for the real data was found to be $a_0 = 0.292$. This background offset is predominantly due to the SR.

Data was also acquired at 36.6 μm beam size and 600 nm wavelength. At this beam size the measured visibilities from two images were 0.346 and 0.341. In comparison with the fitted real visibility curve in Figure 5.17 these values are extremely large to the expected value of approximately 0.32. Unfortunately, from direct imaging of the target surface it was found that the beam was not well centred in the target aperture. Due to this offset in the target and the ambiguity between beam size and beam offset, the measured beam size for this injection data set was increased and thus cannot be included in the fitted visibility curve of Figure 5.17.

A significant SR contribution to the beam size measurement was observed at 600 nm wavelength. In this regime, it was found that SR contributed primarily as a background offset and did not modify the DR interference fringes noticeably. The beam size sensitivity improves with decreasing wavelength. However, in this experiment the SR contribution increased with decreasing wavelength. At 400 nm it was not possible to accurately measure the visibility due to the modification of the distribution due to SR.

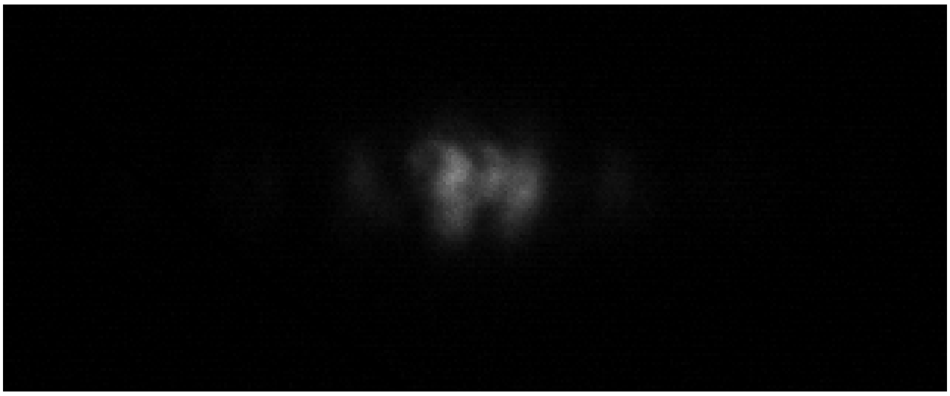

Figure 5.18: DR angular distribution at 400 nm wavelength and 0.5 mm target aperture.

In Figure 5.18 the angular distribution of DR at 400 nm in the 0.5 and 2.0 mm target and mask apertures respectively is shown. The central line profile from Figure 5.18 is compared with the expected distribution from the ODR model in Figure 5.19. In this case the DR fringes have been distorted in amplitude and shape due to the interference with SR.

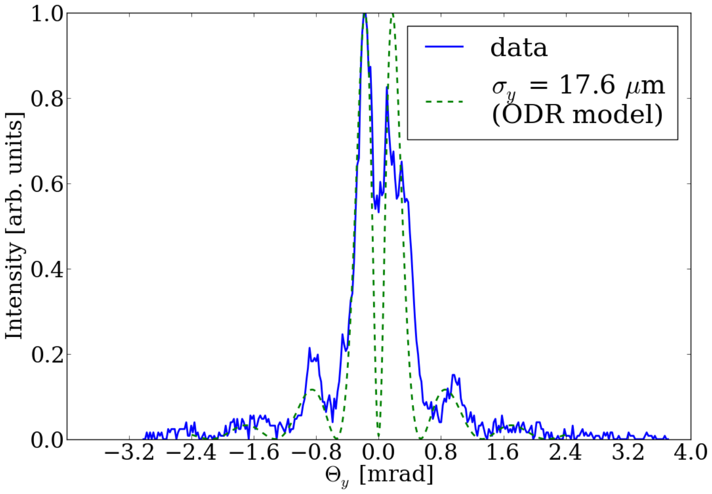

Figure 5.19: Comparison of the 400 nm line profile and expected ODR distribution.

5.3 ODRI Angular Distribution Measurements

For the case where the interference between forward and backward DR is not negligible i.e. when the mask aperture is only twice greater than the target, the angular distributions should be analysed using the ODRI model. In addition to beam size sensitivity, the ODRI model is also sensitive to the beam divergence. In the Monte Carlo application of the ODRI model, the summation of the DR intensity distribution for each electron of the beam is simulated. Therefore each electron is assigned a transverse position and divergence in the beam satisfying the user-defined beam profile. The beam profile and beam divergence are assumed to be Gaussian.

5.3.1 Calculation of the Beam Divergence

To fit the beam size only, a reasonable estimate of the beam divergence was calculated. This was done by calculating the vertical beam emittance using the beam size measurement from the xBSM and the machine optics shown in Table 5.1.

		X [mm]				**Y [mm]**			
Name	**S**	**Beta**	**Phi**	**Eta**	**Orb**	**Beta**	**Phi**	**Eta**	**Orb**
— e- xBSM	23.40	1.35	-	-	-0.025	12.5	-	-	0.015
486 DET_48W	379.403	41.68	44.412	-0.13	0.088	7.86	28.729	0.00	0.000

Table 5.1: Twiss parameters at the xBSM and ODR monitor locations in the storage ring.

The xBSM vertical beam size measurement in pixels $\sigma_y^{pix}(xBSM)$ may be converted to microns $\sigma_y(xBSM)$ using the relation

$$\sigma_y(xBSM) = \sqrt{\left(\frac{50\sigma_y^{pix}(xBSM)}{2.5}\right)^2 - 16^2 - 0.000001}. \tag{5.2}$$

where a measurement at the xBSM of $\sigma_y^{pix}(xBSM) = 1.37$ pixels corresponds to a beam size measurement of 22.2 μm.

From Table 5.1 the Twiss parameters at the locations of the xBSM and ODR monitor are obtained as $\beta_y(xBSM) = 12.5$ m and $\beta_y(ODR) = 7.86$ m respectively. Using this information combined with

$$\sigma_y(ODR) = \sqrt{\frac{\beta_y(ODR)}{\beta_y(xBSM)}} \cdot \sigma_y(xBSM), \tag{5.3}$$

the ratio of the vertical beam size at the ODR monitor $\sigma_y(ODR)$ to the xBSM measurement $\sigma_y(xBSM)$ is $\sigma_y(ODR)/\sigma_y(xBSM) = 0.793$.

Given that $\alpha_y(ODR) = -1.5189$ and using

$$\gamma_y(ODR) = \frac{1 + \alpha_y^2(ODR)}{\beta_y(ODR)}, \tag{5.4}$$

it is found that $\gamma_y(ODR) = 0.4207\ \mathrm{m}^{-1}$ [63].

Using the phase space ellipse shown in Figure 5.20 the natural vertical emittance ε_y is calculated to be $\sigma_y^2(xBSM)/\beta_y(xBSM) = 3.96 \times 10^{11}$ m. From the vertical emittance, the vertical beam size and beam divergence at the ODR location in the storage may be determined using

$$\sigma_y(ODR) = \sqrt{\varepsilon_y \beta_y(ODR)}, \tag{5.5a}$$

$$\sigma_y'(ODR) = \sqrt{\varepsilon_y \gamma_y(ODR)}. \tag{5.5b}$$

In this case, the beam size and beam divergence are 17.6 μm and 4.08 μrad respectively. These results are summarised in Table 5.2.

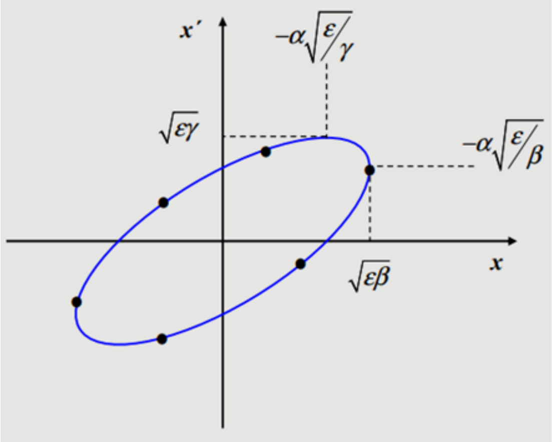

FIGURE 5.20: Calculation of the emittance using the phase space ellipse.

$\sigma_y(xBSM)$ [μ m]	ε_y [m]	$\sigma_y(ODR)$ [μ m]	$\sigma'_y(ODR)$ [μrad]
22.2	3.06E-11	17.6	4.08
46.1	1.70E-10	36.6	8.46
58.2	2.71E-10	46.2	10.7

Table 5.2: Table of beam size and divergence at the ODR monitor.

5.3.2 ODRI Measurements

In Figure 5.21 the ODR and ODRI angular distributions may be compared. Figure 5.21(a) shows the non-interference case (ODR) using a 0.5 mm target and 2.0 mm mask. Figure 5.21(b) shows the interference case (ODRI) using a 1.0 mm mask. An enhancement of the side fringes is observed due to the interference between FDR and BDR from the mask and target respectively.

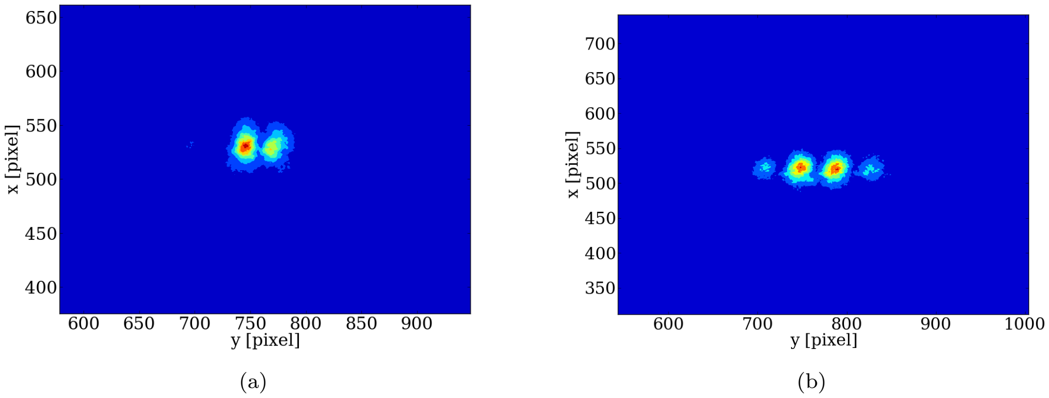

(a) (b)

Figure 5.21: Contour plots of the angular distributions for a) ODR and b) ODRI.

From the ODRI images the central line profiles for different beam sizes were plotted against the expected distributions predicted by the ODRI model. In Figure 5.22 the comparisons between the ODRI model and measured angular distributions for 17.6 μm and 36.6 μm beam sizes are shown.

The asymmetry between the two central lobes of Figure 5.22(a) can be fitted by adjusting the coplanarity offset parameter of the target tines in the ODRI model. The coplanarity offset required for this fit was -40.0 nm which is comparable to that expected from the metrology measurements of the molecular adhesion targets.

The ODRI model predicted that the minima of the angular distributions should go to zero i.e. no light intensity. However the minima of both of these data line profiles were non-zero and significantly larger than predicted by the ODRI model. It is likely that background SR was responsible for this difference between the theoretical prediction and acquired data.

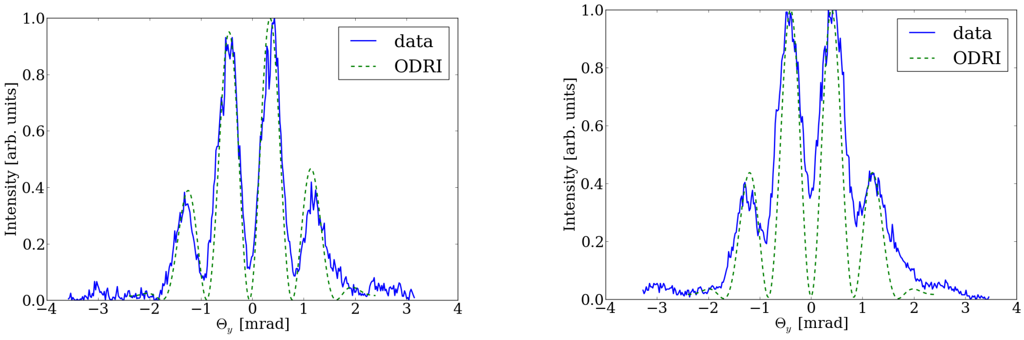

(a)

(b)

FIGURE 5.22: ODRI line profiles at 600 nm wavelength for a) $\sigma_y = 17.6$ μm, $\sigma'_y =$ 4.08 μrad and b) $\sigma_y = 36.6$ μm, $\sigma'_y = 8.46$ μrad.

A beam offset relative to the centre of the target aperture may similarly distort the angular distribution. To quantify the beam position offset, the line profile in Figure 5.22(a) was fitted using the method of least squares with the beam position as a fit variable. The result of the least squares fit is shown in Figure 5.23. The beam offset was found to be 120.0 μm.

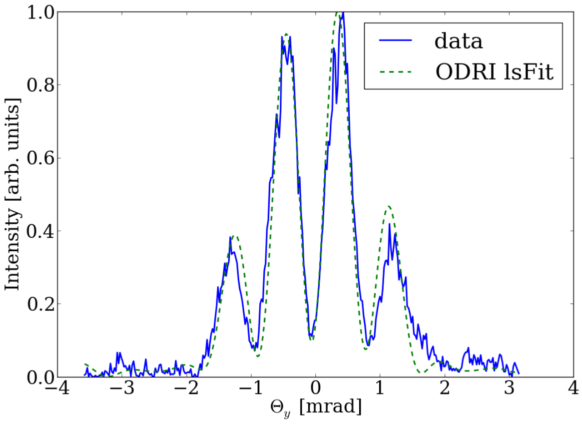

FIGURE 5.23: A beam offset of 120 μm obtained using a least squares fit for ODRI data.

In Figure 5.24 the contour plot and fitted angular distribution are shown at 400 nm wavelength. To attain a reasonable fit of the data many parameters had to be optimised including the beam offset relative to the target centre, misalignment between the mask and target slit centres and coplanrity of the target tines.

In comparison to the ODR measurements acquired in the larger mask aperture, the distortion at 400 nm due to the increased SR is less significant since the ODRI case makes use of the narrower mask aperture. Therefore provided a robust fitting algorithm could be obtained the beam size sensitivity for the ODRI setup is likely to be better than that for the ODR model due to the smaller contribution of SR background.

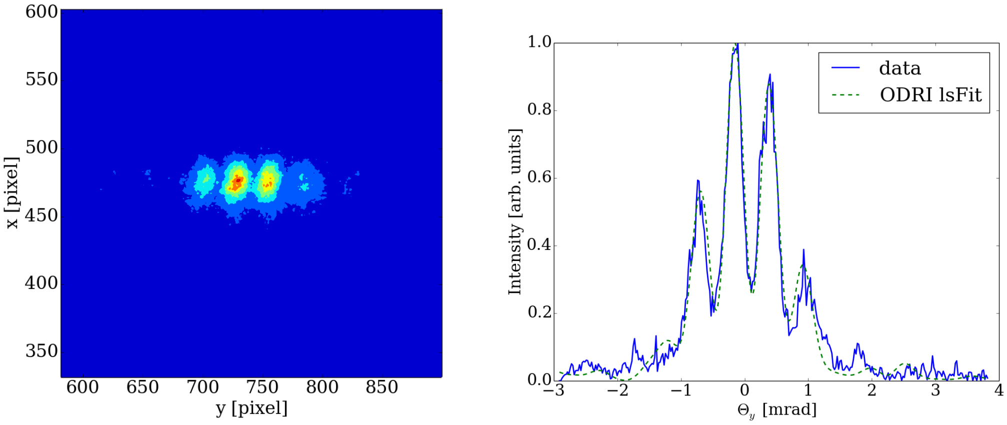

(a) (b)

FIGURE 5.24: Comparison of the ODRI model and data at 400 nm wavelength, 0.5 mm target aperture, 1.0 mm mask aperture, 30 nm target coplanarity offset, -26.5 μm non-linearity between the mask and target slit centres, 150 μm beam offset relative to the target centre, $\sigma_y = 46.2$ μm and $\sigma'_y = 10.7$ μrad.

Chapter 6

Conclusions

In this thesis the feasibility of diffraction radiation for non-invasive micron-scale transverse beam size measurement in circular machines has been investigated. A DR monitor was designed, installed and commissioned at CesrTA with specific emphasis on the beam conditions and requirements for operation on the storage ring.

In comparison to previous ODR experiments on linear machines, installing the monitor on a circular machine particularly affected the design of the target and vacuum chamber due to the wakefield effect, and the method of beam alignment with the target aperture. Since the target must be retracted for injection into the storage ring a fork-like target design connected to a target holder mechanism had to be implemented. To limit distortions to the DR angular distribution the coplanarity of the target was required to be within 10% of the observation wavelength. Various fabrication techniques, such as chemical etching and molecular adhesion using different materials were thoroughly researched and tested.

On a circular machine the beam lifetime must also be monitored. Therefore a detailed method of alignment of the beam in the target aperture had to be established. This was of paramount important for the instrument to operate and also to prevent damage to the target apparatus.

Furthermore, the design of the DR monitor had to account for the wakefields induced by the beam passing through the large cavity of the vacuum chamber when the DR monitor was not in use. Therefore a retractable section of beam pipe was also included in the design of the DR vacuum chamber for when the monitor was not in use.

The principle source of background in DR experiments is synchrotron radiation. On a circular machine there are many bending magnets where SR is emitted. The location of the DR vacuum chamber in the L3 straight was selected with the aim of being as far as possible from the upstream bending magnet to limit the SR incident on the target. Unfortunately to improve the beam size sensitivity using DR, shorter wavelengths must be used. However the SR contribution to background is increased as you go to shorter wavelengths. Therefore a compromise wavelength had to be chosen to provide a reasonable beam size sensitivity and workable signal-to-background ratio.

The optical system also had to be carefully designed to limit the background from synchrotron radiation and provide both direct imaging of the target surface and angular distribution measurements. Considerations had to be made due to the spatial constraints on the system limiting the path length to be within the prewave zone. Direct imaging of the target provided a useful beam alignment tool in addition to the BPMs around the target location. The beam size sensitivity was contained in the angular distribution of DR.

Images of the target surface were compared with those expected from DR theory. The exponential intensity decay of DR from the slit edges was used to verify the DR signal from background. Direct imaging was also used to commission the optical system including the polariser orientation and to investigate interference effects between the mask and target resulting in shadowing.

DR angular distributions were acquired at 400 and 600 nm wavelengths. The target aperture sizes used were 0.5 and 1.0 mm. Upstream of the target a stepped mask was positioned to allow data acquisition with and without interference effects. The interference-free setup used a mask aperture four times larger than the target aperture whereas the interference-present setup employed a mask aperture size double that of the target. In the presence of interference effects broadening of the lobes and enhancement of the side fringes was observed.

The beam size sensitivity was investigated using two models: ODR and ODRI for the interference-free and interference-present systems respectively. An independent x-ray beam size monitor at CesrTA was used to record the vertical beam size in the ring.

At different beam sizes from 17 to 45 μm the visibility of the DR angular distribution was recorded and compared with those expected from the ODR model. It was found that the beam size sensitivity of the DR monitor agreed well with the visibility curve predicted by the model provided the visibility offset due to background SR was accounted for. Unfortunately the ambiguity between beam size and beam offset with respect to the target centre meant that some error was introduced. However this was improved by taking the average visibility from multiple images.

The ODRI model was also used to fit data taken at different beam sizes and wavelength. This model implements many more variables for the fitting however this makes it more complicated to attribute changes to the angular distribution solely due to a difference in beam size. Since the ODRI setup used a smaller mask aperture size the background contribution due to SR was lower, therefore measurements were feasible at 400 nm.

6.1 Improvements to the CesrTA DR monitor

The beam size sensitivity of the DR monitor improves as the wavelength is reduced. However at shorter wavelengths, the signal-to-noise ratio is poor due to the increased contribution of SR.

To significantly reduce the SR reaching the camera the target has been redesigned for future tests at CesrTA. Previously the whole surface of the molecular adhesion targets were coated with Aluminium to reflect all incident rays.

The target images acquired and described in this thesis have shown that only a small region around the target aperture needs to be reflective since the DR distribution is a localised disk around the charged particle beam. Therefore by all incident SR rays on the target outside of this reflective region will not be reflected and hence, not contribute to the DR images. With this improved signal-to-noise ratio, DR observation at shorter wavelengths approaching the UV becomes feasible.

A simultaneous trigger to acquire a beam orbit, xBSM beam size measurement and DR monitor image was commissioned. Presently the 1 mA single bunch beam at CesrTA did not provide enough DR light intensity for single turn beam size measurement. By improving the photon sensitivity of the optical system it may open the way for single turn beam size measurement using DR.

6.2 Potential Application for the Large Hadron Collider

At CesrTA the beam energy E of the circulating electrons is 2.1 GeV. Given Equation 6.1 where m is the particle rest mass and c is the speed of light, this energy corresponds to a Lorentz factor $\gamma = 4.1e3$.

$$E = \gamma mc^2 \tag{6.1}$$

Protons in the LHC with energy of 4 TeV have a similar Lorentz factor to the 2.1 GeV electrons at CesrTA. Using Equation 6.1 the Lorentz factor $\gamma = 4.2e3$ is obtained.

The typical beam dimensions of proton beams in the LHC are in the millimetre range so that a resolution of 100 μm is sufficient in most cases [1, 18]. The target aperture size should be $10\sigma_y$. Given a rough beam size $\sigma_y = 1$ mm results in a target aperture of 10 mm. The impact parameter is half of the target width, in this case 5 mm.

Using Equation 2.4 the characteristic DR emission wavelength can be calculated. For $h = 5$ mm and $\gamma = 4.2e3$ the wavelength is in the long infrared range $\lambda = 7$ μm.

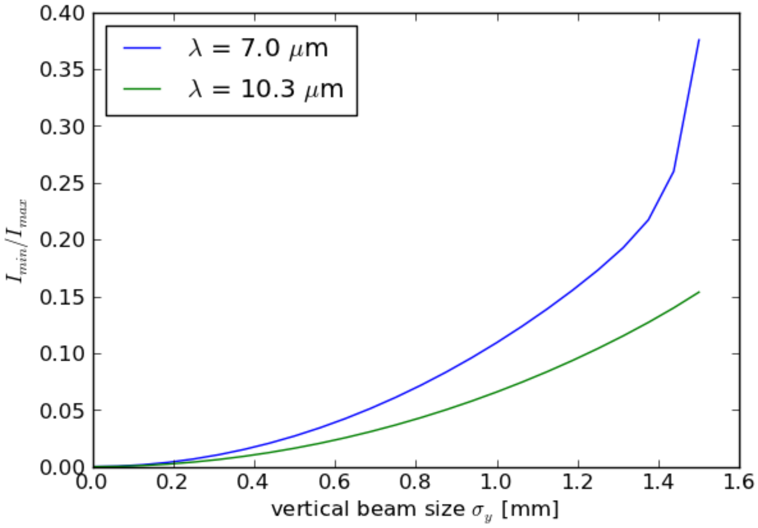

FIGURE 6.1: Visibility curves simulated for the LHC.

In Figure 6.1 the visibility curves were simulated via the ODR model for 7 and 10.3 μm wavelengths using the parameters above. Many thermal imaging systems are commercially available with peak sensitivity at 10 μm since this corresponds to human body temperature, therefore this wavelength was also simulated.

The visibility ranges from zero to 0.1 at 1.0 mm beam size. This 10% difference is double that which was used at CesrTA where the visibility ranged from zero to 0.05 at 50 μm. Therefore the beam size sensitivity for a DR monitor at the LHC is potentially a factor of two better over the range of beam sizes of interest.

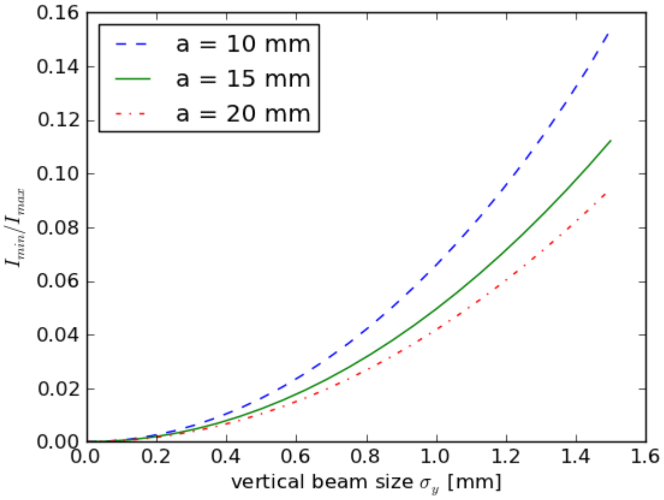

FIGURE 6.2: Visibility curves for different target apertures.

The main source of background in DR measurements is from SR. By using protons this background is significantly reduced. Furthermore, since the characteristic DR wavelength is in the infrared spectral range the SR at at these long wavelengths is relatively low. Therefore with these considerations in mind a DR monitor would be more suitable for a proton circular machine rather than an electron beam since the background is low and the beam size resolution is relaxed.

Given a wavelength of 10.3 μm, the effect of the choice of target aperture size for the proton beam is investigated and presented in Figure 6.2. From the study at CesrTA it was observed that the beam lifetime improves with target aperture size. The visibility curves all range by at least 4% from zero to 1 mm beam size which is a sufficient beam size sensitivity for detection.

6.3 Coherence Length Study at CTF3

From the observations of the interference effect in target imaging at CesrTA, a follow up investigation was initiated at CTF3, CERN, Switzerland. To reproduce these observations at CTF3 a setup using two non-parallel screens shown in Figure 6.3 will be installed to simulate the ODR mask/target configuration. The use of OTR screens rather than ODR slits simplifies the hardware installation and operation. Furthermore, the 200 MeV electron beam available at CTF3 is too low energy for ODR measurements. In this setup, Optical Transition Radiation Interference (OTRI) may be observed at various screen separation distances.

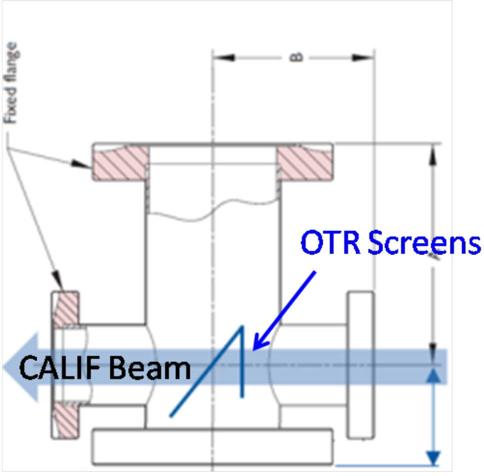

FIGURE 6.3: Schematic of the OTRI setup at CTF3 (courtesy of S. Mazzoni).

6.4 Combined OTR/ODR Monitor at ATF2

Following on from the improved performance of OTR and ODR monitors in recent years, the design of a combined high resolution OTR/ODR monitor is under-way. The main aim is to develop, install and test a combined OTR/ODR emittance station working initially in the visible spectrum whilst providing the opportunity to measure UV/soft

X-ray radiation to minimise the diffraction limit effect. Due to the small slit size required to measure sub-micron beam sizes and impact on beam lifetime in addition to SR background considerations, it was found that high resolution measurements would not be feasible at CesrTA. Instead the combined OTR/ODR monitor will be installed at ATF2 in Japan.

The goal resolutions for this combined monitor are < 1 μm and < 14 μm for OTR and ODR respectively. Since this monitor is located on a linear machine the ODR photon yield may be increased by a reduction of the slit aperture to $100 - 200$ μm. With a sufficient photon yield, the ODR resolution may be improved by operating at shorter wavelengths, most likely < 200 nm.

6.5 Summary

For future accelerators, such as the Compact Linear Collider, high resolution non-invasive beam size measurements are crucial. Although laser wire scanners do fulfil this specification the overheads and maintenance costs associated with these monitors would be very expensive for large-scale accelerators.

Diffraction radiation has been widely studied on linear machines. To complement this work and meet the needs of future accelerators, the feasibility of diffraction radiation monitors on circular machines has been investigated and presented in this thesis. The design, operation and performance of the diffraction radiation monitor installed and tested at CesrTA has been described.

Beam sizes of 17.6 μm and 45 μm have been measured at CesrTA using the ODR monitor operating at 600 nm wavelength. These beam size measurements were corroborated with an independent beam profiler. It was found that operating at shorter wavelengths was challenging due to the increased background from SR emitted from nearby bending magnets.

ODRI measurements were also performed. However due to the numerous degrees of freedom in the ODRI model in addition to the SR background, direct beam size measurement was unsuccessful. This could possibly be improved by using more sophisticated fitting algorithms.

The application of ODR target imaging as a beam position monitor has been demonstrated to align the beam with the centre of the target aperture. In this setup, the shadowing effect was observed.

In conclusion, the proof of principle test of the use of ODR monitors on circular machines is demonstrated in this thesis project. However, due to the impact on beam lifetime, other techniques for beam size monitoring may be more suitable. This is particularly true for electron storage rings where small target apertures must be used given the micron scale beam size. ODR monitors on proton/ion circular machines may be more feasible due to the relaxed resolution requirements.

This work has also contributed towards the initiation of new experiments at CTF3, ATF2 and potentially the LHC.

Appendix A

Technical Drawings

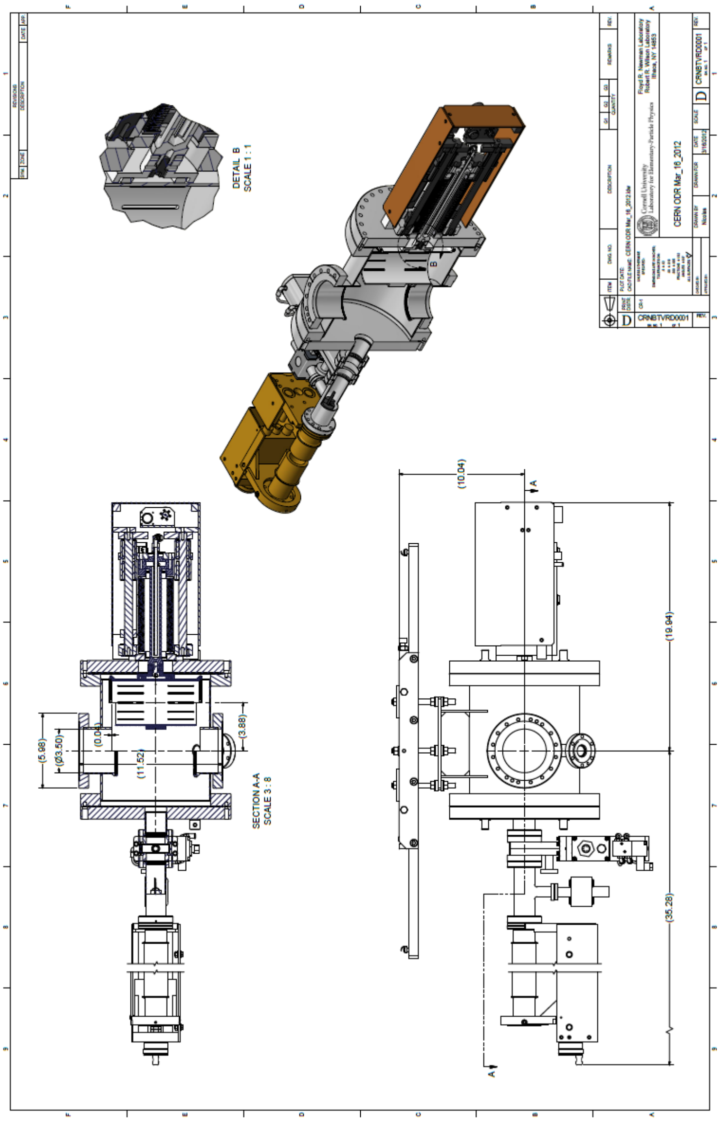

FIGURE A.1: Technical drawing of the DR vacuum chamber (by N. Chritin).

List of Figures

1.1 CLIC layout at 3 TeV [3]. . . . 2

1.2 Schematic of the PS and PSB rotational wire scanner [8]. . . . 4

1.3 Schematic (a) and photograph (b) of the OTR bean profile monitor at ATF2 [5]. . . . 5

1.4 Schematic of a pinhole camera where d is the source-to-pinhole distance, md is the pinhole-to-detector distance, w is the pinhole aperture size and λ is the wavelength [26]. . . . 7

1.5 Imaging principle of a pinhole camera. In this example h is the object height i.e. the electron beam size, L is the object-to-pinhole distance, L' is the pinhole-to-image plane distance and a' is the pinhole size [9]. . . . 7

1.6 Schematic of a SR interferometer where d_0 is the source-to-double slit distance, d_1 is the double slit-to-detector distance, w is the slit aperture size, D is the interslit distance of the double slit screen and λ is the wavelength [26]. . . . 8

1.7 A plot of the SR power vs wavelength for different beam energies [27]. . . 9

1.8 Laser wire schematic [17]. . . . 11

2.1 Schematic of DR emission from a particle moving in the vicinity of a medium [11] 18

2.2 Schematic of the emission cone angle for TR (shown here) and DR for three elementary sources on the target within the electron effective field radius [11]. . . . 19

2.3 Geometry of photon propagation in the prewave zone suppression setup using a thin lens where l is the distance from the target to the lens, BFL is the back focal length of the lens and $\rho_d(x, y)$ is the position of emission angle $\theta_{x,y}$ on the detector plane. . . . 19

2.4 DR emission from a half-plane [11]. . . . 21

2.5 Diffraction radiation angular distribution calculated using Equation 2.8 where $\gamma = 4110$, $h = 0.26$ mm, $\theta_x = 0$ and $\lambda = 400$ nm. . . . 21

2.6 Schematic of DR from a slit. . . . 22

2.7 Diffraction radiation angular distribution calculated using Equation 2.10 where $\gamma = 4.11 \times 10^3$, $a = 0.5$ mm, $\lambda = 400$ nm and $a_x = 0$. . . . 23

2.8 A summary of the steps performed in the PVPC technique for beam size measurement [33]. . . . 24

2.9 DR angular distributions at $t_x = 0$ for $a = 0.5$ mm and $E = 2.1$ GeV: (a) comparison of $\sigma_y = 0$ μm and 50 μm at 200 nm and (b) comparison of $\sigma_y = 0$ μm and 50 μm at 400 nm. . . . 25

2.10 DR angular distributions at $t_x = 0$ for $\lambda = 400$ nm and $E = 2.1$ GeV: (a) comparison of $\sigma_y = 0$ μm and 50 μm at $a = 0.5$ m and (b) Comparison of $\sigma_y = 0$ μm and 50 μm at $a = 1.0$ mm. 26
2.11 Visibility curves showing the increased beam size sensitivity at shorter wavelengths using a 2.1 GeV beam energy and 0.5 mm target aperture. . 26
2.12 Visibility curves for beam size measurement using 400 nm wavelength and 0.5 mm target aperture for different beam energies. 27
2.13 Angular distributions to show the ambiguity between beam size and beam offset with respect to the target centre. 27
2.14 Definition of the coordinate system used in the ODRI model- modified from [12]. 30
2.15 A schematic illustrating the additional parameters of the ODRI model: coplanarity Δ, mask and target non-linearity δ and distance between the mask and target d. 31
2.16 The effect of target coplanarity on the DR angular distribution for a single electron passing through the target centre where $a_2 = 1.0$ mm, $\lambda = 400$ nm and $E = 2.1$ GeV. 31
2.17 Comparison of the interference effect given a 1.0 mm target aperture for 1.0, 2.0 and 4.0 mm mask apertures for 400 nm wavelength, 2.1 GeV beam energy and 25 μm beam size. The 2.0 and 4.0 mm mask aperture distributions are overlaid with one another showing very little difference. However a significant difference is observed between the 1.0 and 2.0 mm mask aperture distributions. 32
2.18 Comparison of ODR and ODRI for a 0.5 mm target aperture: 400 nm wavelength, 2.1 GeV, $a_2 = 0.5$ mm and $a_1 = 2.0$ and 1.0 mm for the ODR and ODRI cases respectively.. 33
2.19 Breaking the ambiguity in the angular distributions by using a 0.1 mm misalignment between the target and mask aperture centres for the case of zero beam offset with 50 μm beam size and zero beam size with 50 μm beam offset where $\lambda = 400$ nm, $E = 2.1$ GeV, $a_2 = 0.5$ mm and $a_1 = 1.0$ mm. 34
2.20 Geometry for imaging with DR from a circular aperture presented here to show the subscript notation for the source, lens and detector plans [44]. 36
2.21 Target imaging point spread function (PSF) at $x_i = 0$ for a single electron with parameters: $\gamma = 4110$, $t_1 = t_2 = 0.25$ mm, $\lambda = 600$ nm, $\theta_m = 0.0636$, $k = 10.5 \times 10^6$ m^{-1} and $M = -0.611$. 36
2.22 Gaussian distributed beam profile (a) and DR distribution on the target surface (b) using the Monte Carlo approach (green histogram) with the normal probability density function (dashed red line) for $\sigma_y = 17.6$ μm. . 37
2.23 PSF at $x_i = 0$ for a single electron passing through a rectangular slit with 20 μm vertical offset relative to the slit centre with parameters: $t = 100$ μm, $t_1 = 30$ μm and $t_2 = 70$ μm [44]. 37
2.24 PSF of the DR from a rectangular slit for the horizontal (a) and vertical (b) components [44]. 38
2.25 PSF at $x_i = 0$ for a single electron passing through a rectangular slit with 20 μm vertical offset relative to the slit centre [44]. 38

3.1 A modified figure showing the layout of CESR from [47]. 40
3.2 Layout of the xBSM [49]. 42

3.3 Simplified schematic of the xBSM layout where a is the total vertical extent of partial transmission through the mask material, a' is the vertical extent of slits in the mask, L is the source to optical element distance and L' is the optical element to detector distance. for general operation a pinhole optical element is used [9]. 43
3.4 Pinhole detector histogram with fit using the pinhole (vertical slit) xBSM setup [49]. 44
3.5 Layout of vBSM optics [52]. 45
3.6 Typical CCD images recorded by the vBSM at two different image planes: (a) direct image and (b) interferometer image are at the image plane of the source point, (c) is at the image plane of the double slits and (d) is the integrated horizontal intensity profile of (c) [50]. 46
3.7 Overview of the DR vacuum tank. 47
3.8 Technical drawing of the replacement chamber (by N. Chritin and J. Conway). 47
3.9 Photographs of the replacement chamber (courtesy of J. Conway). 48
3.10 DR viewport specification (courtesy of Vaqtec SRL). 49
3.11 Dummy target in the vacuum chamber viewed from the downstream direction (courtesy of Y. Li). 50
3.12 Technical drawing of the chemically etched target (by N. Chritin). 50
3.13 Combined 0.5 and 1.0 mm aperture chemically etched target [54]. 51
3.14 Definitions of roughness measurement where peaks and valleys are labelled Zp_i and Zv_i respectively over the sampling length l [54]. 52
3.15 Measurements of the flatness across the set 7V targets: (a, c) combined 0.5/1.0 mm target and (b, d) 1.0 mm target [54]. 54
3.16 Measurements of the flatness across the set 2V targets: (a, c) combined 0.5/1.0 mm target and (b, d) 1.0 mm target [54]. 55
3.17 Photograph of the 2 mm Silicon molecular adhesion target. 55
3.18 Technical drawing of the 1.0 mm Al/Cr coated Silica molecular adhesion target (courtesy of Winlight Optics). 56
3.19 Flatness measurements for the 1.0 mm Si molecular adhesion target (courtesy of Winlight Optics). 59
3.20 Schematic of the reflection geometry of the target. 60
3.21 Reflectance curves for different materials at target tilt angle $\theta_0 = 70°$: the “solid line” denotes the vertical polarisation component R_p and the “dashed line” denotes the horizontal polarisation component R_s. 62
3.22 Target holder with mask and target mounted (by N. Chritin). 63
3.23 Measurements of the flatness across masks E: (a, c) Mask E1 and (b, d) Mask E2 [54]. 64
3.24 Measurements of the flatness across Masks H [54]. 65
3.25 Optical system schematic showing the main components. 66
3.26 Photographs of the optical system: (a) in December 2013 before installation and (b) in December 2014 in the accelerator tunnel. 66
3.27 Technical drawing of the optical components positions (by J. Conway). . . 67
3.28 Spectral sensitivity of the M2582 intensifier (courtesy of Proxivision). . . 69
3.29 Block digram of the camera module (courtesy of Proxivision). 70

3.30 Comparison of the DR angular distribution in the far-field, in the back focal plane of an ideal lens and in the back focal plane of the plano-convex lens ($\lambda = 400$ nm, $\gamma = 4110$, $\theta_x = 0$, $a = \frac{\gamma\lambda}{2\pi}$) [59]. 71
3.31 Zemax output: (a) source, (b) detector plane and (c) horizontal cross-section of the detector plane [60]. 71
3.32 Comparison of the angular distribution in far-field condition, in the near-field using an ideal and also a real biconvex lens [60]. 72

4.1 Horizontally polarised irradiance plot of synchrotron radiation on the target surface from the simulations in SRW. 76
4.2 Vertically polarised irradiance plot of synchrotron radiation on the target surface from the simulations in SRW. 76
4.3 SR spectra output from SRW for the horizontal and vertical polarisation components. 77
4.4 Image of the dummy target showing the regions of localised TR and SR on the slit edges and approximately uniform SR background at 400 nm wavelength. 78
4.5 A plot of the intensity profile (solid line) and expected distributions from Equation 2.17b (dashed line) and Zemax (dash-dot line). 80
4.6 A schematic to indicate the mask and target positioning for ODR (zero interference) and ODRI (interference) studies at target translation positions of 26600 cunits and 28400 cunits respectively. 81
4.7 Fast log data of beam current and target translation position (a) and a zoomed in section (b). The red dotted line at target position −27113 cunits denotes the position where the target is fully retracted from the vacuum chamber. The purple dotted line at −6000 cunits denotes the standby position. The target must be retracted to the limit switch at this position for injection. At this position the target is safely retracted at the edge of the vacuum chamber. At 25800 cunits the target is located next to the beam. The position at 26600 cunits denotes the ODR measurement position of the target. The pink dotted line at 28400 cunits is the ODRI measurement position. 82
4.8 The vertical electron beam profile obtained by Mike Billing et al. by the vertical scraper investigation. 83

5.1 Target surface images of the (a) vertical polarisation at 95 deg. and (b) horizontal polarisation at 180 deg. Note that the target images are rotated by 90 deg due to the spatial constraints of the imaging system: x-direction is parallel and y-direction is perpendicular with respect to the target tines (slit edges). 85
5.2 Polarisation scans taken in (a) December 2013 and (b) April 2014. 86
5.3 An image of the coated glass molecular adhesion target: 1.0 mm target aperture, 4.0 mm mask aperture, 600 nm wavelength and 21 μm vertical beam size as measured by the xBSM. 87
5.4 Image sequence (a), (b), (c) and (d) showing the insertion of the target and alignment of the beam with the aperture. Due to the orientation of the optical system the images are rotated by 90° i.e. the horizontal plane along which the target is inserted is parallel with the target tines and the width of the target aperture is in the vertical plane. 87

5.5 DR verification by fitting the exponential intensity decay from the target edge. 88
5.6 A fit of the normalised line profile from the 0.5 mm molecular adhesion target surface for a beam relatively well centred in the target aperture. . . 88
5.7 Schematic of the mask and target assembly. 89
5.8 Shadowing of the Coulomb field. 89
5.9 Images of the 0.5 mm target surface: (a) with negligible shadowing from a 2 mm mask and (b) with significant shadowing from a 1 mm mask where $\lambda = 600$ nm. 90
5.10 The DR angular distribution image of the coated glass molecular adhesion target: 1.0 mm target aperture, 4.0 mm mask aperture, 600 nm wavelength and 21 μm vertical beam size as measured by the xBSM. . . . 91
5.11 Comparison of the DR angular distribution with the ODR model: 1.0 mm target aperture, 4.0 mm mask aperture, 600 nm wavelength and 21 μm vertical beam size as measured by the xBSM. 92
5.12 Comparison of the DR angular distribution with the ODRI model: 1.0 mm target aperture, 4.0 mm mask aperture, 600 nm wavelength and 21 μm vertical beam size as measured by the xBSM. 92
5.13 Measurement of the back focal plane using a linear translation stage scan. 93
5.14 An example of the DR angular distribution: $\lambda = 600$ nm, 0.5 mm target and 2 mm mask. 93
5.15 A comparison of projected vertical polarisation components (PVPCs) for different beam sizes. 94
5.16 Expected (blue line) and measured (green dashed line) visibility curves for 0.5 mm target and 600 nm wavelength. 95
5.17 Resultant visibility curve at 600 nm wavelength and 0.5 mm target aperture from a least squares fit of the average visibility (green circles) at two beam sizes. 96
5.18 DR angular distribution at 400 nm wavelength and 0.5 mm target aperture. 97
5.19 Comparison of the 400 nm line profile and expected ODR distribution. . . 97
5.20 Calculation of the emittance using the phase space ellipse. 99
5.21 Contour plots of the angular distributions for a) ODR and b) ODRI. . . . 100
5.22 ODRI line profiles at 600 nm wavelength for a) $\sigma_y = 17.6$ μm, $\sigma'_y = 4.08$ μrad and b) $\sigma_y = 36.6$ μm, $\sigma'_y = 8.46$ μrad. 101
5.23 A beam offset of 120 μm obtained using a least squares fit for ODRI data. 101
5.24 Comparison of the ODRI model and data at 400 nm wavelength, 0.5 mm target aperture, 1.0 mm mask aperture, 30 nm target coplanarity offset, -26.5 μm non-linearity between the mask and target slit centres, 150 μm beam offset relative to the target centre, $\sigma_y = 46.2$ μm and $\sigma'_y = 10.7$ μrad. 102

6.1 Visibility curves simulated for the LHC. 106
6.2 Visibility curves for different target apertures. 106
6.3 Schematic of the OTRI setup at CTF3 (courtesy of S. Mazzoni). 107

A.1 Technical drawing of the DR vacuum chamber (by N. Chritin). 110

List of Tables

1.1 Transverse beam size requirements for CLIC (where MDI is the Machine Detector Interface and RTML is the Ring To Main Linac) [3]. 2

3.1 Parameters of the Cornell Electron Storage Ring Test Accelerator (CESRTA) [9]. 41
3.2 Phase 1 Experiment parameters for CesrTA (courtesy of M. Billing) and comparison with the CLIC damping ring complex [3]. 41
3.3 Geometrical parameters defining the CesrTA xBSM beamlines [9]. 43
3.4 Conditions of measurement for the masks and chemically etched targets [54]. 52
3.5 Roughness results for the chemically etched targets [54]. 53
3.6 Aperture size measurement of the chemically etched targets [54]. 53
3.7 Summary of flatness measurements for the chemically etched targets [54]. 53
3.8 Comparison of the specification and measured values of the block for the 1 mm Al/Cr coated Silica molecular adhesion target (courtesy of Winlight Optics). 57
3.9 Comparison of the specification and measured values of the tines for the 1 mm Al/Cr coated Silica molecular adhesion target (courtesy of Winlight Optics). 57
3.10 Metrology results of the assembled 1 mm Al/Cr coated Silica molecular adhesion target (courtesy of Winlight Optics). The positions of 4.5 mm and 14.5 mm correspond to the start and end points of the "zone utile" area. 57
3.11 Comparison of the specification and measured values of the block for the 0.5 mm Al/Cr coated Silica molecular adhesion target (courtesy of Winlight Optics). 58
3.12 Comparison of the specification and measured values of the tines for the 0.5 mm Al/Cr coated Silica molecular adhesion target (courtesy of Winlight Optics). 58
3.13 Metrology results of the assembled 0.5 mm Al/Cr coated Silica molecular adhesion target (courtesy of Winlight Optics). The positions of 4.5 mm and 14.5 mm correspond to the start and end points of the "zone utile" area. 58
3.14 Mask aperture sizes. 63
3.15 Roughness results for the masks [54]. 63
3.16 Aperture size measurement of the masks [54]. 64
3.17 Flatness measurements across each tine for the masks [54]. 65

4.1 L3 straight section lattice components ordered in positron direction convention (reverse order for electrons). 75

5.1 Twiss parameters at the xBSM and ODR monitor locations in the storage ring. 98
5.2 Table of beam size and divergence at the ODR monitor. 100

Bibliography

[1] O. Bruning, H. Burkhardt, and S. Myers. The large hadron collider. *Progress in Particle and Nuclear Physics*, 67(3):705–734, 7 2012.

[2] ATLAS Collaboration. Observation of a new particle in the search for the standard model higgs boson with the ATLAS detector at the LHC. *Physics Letters B*, 716(1):1–29, 9/17 2012.

[3] M. Aicheler, P. Burrows, T. Draper, T. Garvey, P. Lebrun, K. Peach, N. Phinney, H. Schmickler, and D. :. Toge Schulte N. A multi-TeV linear collider based on CLIC technology: CLIC conceptual design report. Technical Report CERN-2012-007, 2012.

[4] J. P. Delahaye, G. Guignard, T. Raubenheimer, and I. Wilson. Scaling laws for e+/e- linear colliders. *Nuclear Instruments and Methods in Physics Research Section A: Accelerators, Spectrometers, Detectors and Associated Equipment*, 421(3):369–405, 2/1 1999.

[5] K. Kruchinin, A. Aryshev, P. Karataev, B. Bolzon, T. Lefevre, S. Mazzoni, M. Shevelev, S. T. Boogert, L. J. Nevay, N. Terunuma, and J. Urakawa. Sub-micrometer transverse beam size diagnostics using optical transition radiation. *Phys.: Conf. Ser.*, 517(012011), 2014.

[6] W. S. Graves, E. D. Johnson, and S. Ulc. A high resolution electron beam profile monitor and its applications. In *AIP Conference Proceedings*, page 206, 1998.

[7] U. Hahn, N. v. Bargen, P. Castro, O. Hensler, S. Karstensen, M. Sachwitz, and H. Thom. Wire scanner system for FLASH at DESY. *Nuclear Instruments and Methods in Physics Research Section A: Accelerators, Spectrometers, Detectors and Associated Equipment*, 592(3):189–196, 7/21 2008.

[8] G. Baud, B. Dehning, J. Emery, J-J Gras, A. Guerrero, and E. Piselli. Performance assessment of wire-scanners at CERN. In *Proceedings of IBIC2013*, page 499, 2013.

[9] J. P. Alexander, A. Chatterjee, C. Conolly, E. Edwards, M. P. Ehrlichman, E. Fontes, B. K. Heltsley, W. Hopkins, A. Lyndaker, D. P. Peterson, N. T. Rider, D. L. Rubin, J. Savino, R. Seeley, J. Shanks, and J. W. Flanagan. Vertical beam size

measurement in the CESR-TA storage ring using x-rays from synchrotron radiation. *Nuclear Instruments and Methods in Physics Research Section A: Accelerators, Spectrometers, Detectors and Associated Equipment*, 748(0):96–125, 6/1 2014.

[10] A. Hansson, E. Walln, and . Andersson. Transverse electron beam imaging system using visible synchrotron radiation at MAX III. *Nuclear Instruments and Methods in Physics Research Section A: Accelerators, Spectrometers, Detectors and Associated Equipment*, 671(0):94–102, 4/11 2012.

[11] P. Karataev. Investigation of optical diffraction radiation for non-invasive low-emittance beam size diagnostics, 2004.

[12] A. Cianchi, M. Castellano, L. Catani, E. Chiadroni, K. Honkavaara, and G. Kube. Nonintercepting electron beam size monitor using optical diffraction radiation interference. *Phys. Rev. ST Accel. Beams*, 14(10):102803, 2011.

[13] E. Chiadroni, M. Castellano, A. Cianchi, K. Honkavaara, G. Kube, V. Merlo, and F. Stella. Non-intercepting electron beam transverse diagnostics with optical diffraction radiation at the DESY FLASH facility. *Nuclear Instruments and Methods in Physics Research Section B: Beam Interactions with Materials and Atoms*, 266(17):3789–3796, 9 2008.

[14] A. H. Lumpkin, J. W. Berg, N. S. Sereno, D. W. Rule, and C. Y Yao. Near-field imaging of optical diffraction radiation generated by a 7-GeV electron beam. *Physical Review Special Topics Accelerators and Beams*, 10(2):022802, 2007.

[15] L. Corner, A. Aryshev, G. A. Blair, S. T. Boogert, P. Karataev, K. Kruchinin, N. Terunuma, J. Urakawa, and R. Walczak. Laserwire: A high resolution non-invasive beam profiling diagnostic. *Nuclear Instruments and Methods in Physics Research, Section A: Accelerators, Spectrometers, Detectors and Associated Equipment*, 2013. Article in Press.

[16] K. Balewski, G. A. Blair, S. T. Boogert, G. Boorman, J. Carter, T. Kamps, T. Lefevre, H. Lewin, F. Poirier, S. Schreiber, and K. Wittenburg. Beam profile measurements at PETRA with the laserwire compton scattering monitor. In *Proceedings of EPAC 2004*, page 2526, 2004.

[17] L. J. Nevay, R. Walczak, and L. Corner. High power fiber laser system for a high repetition rate laserwire. *Phys. Rev. ST Accel. Beams*, 17(7):072801, 2014.

[18] K. Wittenburg. Specific instrumentation and diagnostics for high-intensity hadron beams. *CERN Yellow Report*, page 251, 2013.

[19] M. Koujili, J. De Freitas, B. Dehning, J. Koopman, and D. :Sapinski Ramos M. Fast and high accuracy wire scanner. In *Proceedings of DIPAC09*, page 188, 2009.

[20] A. P. Potylitsyn. Transition radiation and diffraction radiation. similarities and differences. *Nuclear Instruments and Methods in Physics Research Section B: Beam Interactions with Materials and Atoms*, 145(12):169–179, 10/2 1998.

[21] M. Castellano and V. Verzilov. Spatial resolution in optical transition radiation beam diagnostics. *Phys. Rev. ST Accel. Beams*, 1(6):062801, 1998.

[22] P. Karataev, A. Aryshev, S. Boogert, D. Howell, N. Terunuma, and J. Urakawa. First observation of the point spread function of optical transition radiation. *Phys. Rev. Lett.*, 107(17):172801, 2011.

[23] M. Ross, S. Anderson, J. Frisch, K. Jobe, D. McCormick, B. McKee, J. Nelson, T. Smith, H. Hayano, T. Naito, and N. Terunuma. A very high resolution optical transition radiation beam profile monitor*. *SLAC-PUB*, 9280, 2002.

[24] P. Piot, J. C. Denard, P. Adderley, K. Capek, and E. Feldl. High current CW beam profile monitors using transition radiation at CEBAF. In *Particle Accelerator Conference, 1997. Proceedings of the 1997*, volume 2, page 2198, 1997.

[25] G. Kube. Review of synchrotron radiation based diagnostics for transverse profile measurements. In *Proceedings of DIPAC 2007*, page MOO1A03, 2007.

[26] S. Takano. Beam diagnostics with synchrotron radiation in light sources. In *Proceedings of IPAC10*, volume C100523, page WEZMH01, 2010.

[27] Properties of synchrotron radiation, 2011.

[28] A. Bosco, M. T. Price, G. A. Blair, S. T. Boogert, G. Boorman, S. Malton, C. Driouichi, T. Kamps, F. Poirier, K. Balewski, E. Elsen, V. Gharibyan, H. C Lewin, S. Schreiber, N. Walker, and K. Wittenburg. A two-dimensional laser-wire scanner for electron accelerators. *Nuclear Instruments and Methods in Physics Research Section A: Accelerators, Spectrometers, Detectors and Associated Equipment*, 592(3):162–170, 7/21 2008.

[29] I. Agapov, G. A. Blair, and M. Woodley. Beam emittance measurement with laser wire scanners in the international linear collider beam delivery system. *Phys. Rev. ST Accel. Beams*, 10(11):112801, 2007.

[30] R. Alley, D. Arnett, E. Bong, W. Colocho, J. Frisch, S. Horton-Smith, W. Inman, K. Jobe, T. Kotseroglou, D. McCormick, J. Nelson, M. Scheeff, S. Wagner, and M. C. Ross. A laser-based beam profile monitor for the SLC/SLD interaction region. *Nuclear Instruments and Methods in Physics Research Section A: Accelerators, Spectrometers, Detectors and Associated Equipment*, 379(3):363–365, 9/21 1996.

[31] S. T. Boogert, G. A. Blair, G. Boorman, A. Bosco, L. C. Deacon, P. Karataev, A. Aryshev, M. Fukuda, N. Terunuma, J. Urakawa, L. Corner, N. Delerue, B. Foster, D. Howell, M. Newman, R. Senanayake, R. Walczak, and F. Ganaway. Micron-scale laser-wire scanner for the KEK accelerator test facility extraction line. *PhysRevSTAB.13.122801*, 13(12):122801, 2010.

[32] Yosuke Honda, Noboru Sasao, Sakae Araki, Yasuo Higashi, Toshiyuki Okugi, Takashi Taniguchi, Junji Urakawa, Yoshio Yamazaki, Koichiro Hirano, Masahiro Nomura, Mikio Takano, and Hiroshi Sakai. Upgraded laser wire beam profile monitor. *Nuclear Instruments and Methods in Physics Research Section A: Accelerators, Spectrometers, Detectors and Associated Equipment*, 538(13):100–115, 2/11 2005.

[33] P. Karataev, S. Araki, R. Hamatsu, H. Hayano, T. Muto, G. Naumenko, A. Potylitsyn, N. Terunuma, and J. Urakawa. Beam-size measurement with optical diffraction radiation at KEK accelerator test facility. *Phys. Rev. Lett.*, 93:244802, 2004.

[34] E. Chiadroni, M. Castellano, A. Cianchi, K. Honkavaara, G. Kube, V. Merlo, and F. Stella. Non-intercepting electron beam transverse diagnostics with optical diffraction radiation at the DESY FLASH facility. In *Proceedings of PAC07*, page 3982. IEEE, 2007.

[35] L. Wartski, S. Roland, J. Lasalle, M. Bolore, and G. Filippi. Interference phenomenon in optical transition radiation and its application to particle beam diagnostics and multiple scattering measurements. *J. Appl. Phys.*, 46(8):3644, 1975.

[36] M. Castellano. A new non-intercepting beam size diagnostics using diffraction radiation from a slit. *Nuclear Instruments and Methods in Physics Research Section A: Accelerators, Spectrometers, Detectors and Associated Equipment*, 394(3):275–280, 7/21 1997.

[37] R. B. Fiorito and D. W. Rule. Diffraction radiation diagnostics for moderate to high energy charged particle beams. *Nuclear Instruments and Methods in Physics Research Section B: Beam Interactions with Materials and Atoms*, 173(12):67–82, 1 2001.

[38] E. J. N. Wilson. *An Introduction to Particle Accelerators.* Oxford University Press, 2001.

[39] A. P. Potylitsyn, M. I. Ryazanov, M. N. Strikhanov, and A. A. Tishchenko. *Diffraction Radiation from Relativistic Particles.* Springer, Berlin Heidelberg, 2010.

[40] P. V. Karataev. Pre-wave zone effect in transition and diffraction radiation: Problems and solutions. *Physics Letters A*, 345(46):428–438, 10/3 2005.

[41] MAX BORN and EMIL WOLF. *CHAPTER VIII - ELEMENTS OF THE THEORY OF DIFFRACTION*, pages 370–458. Principles of Optics (Sixth (Corrected) Edition). Pergamon, 1980.

[42] P. Karataev, R. Hamatsu, T. Muto, S. Araki, H. Hayano, J. Urakawa, G. Naumenko, A. Potylitsyn, and T. Hirose. Application of optical diffraction radiation to a non-invasive low-emittance high-brightness beam diagnostics. In *Quantum aspects of beam physics. Proceedings, Joint 28th Advanced Beam Dynamics and Advanced and Novel Accelerator Workshop, QABP'03*, page 111, January 7-11, 2003 2004.

[43] M. Slater, C. Adolphsen, R. Arnold, S. Boogert, G. Boorman, F. Gournaris, M. Hildreth, C. Hlaing, F. Jackson, O. Khainovski, Yu G. Kolomensky, A. Lyapin, B. Maiheu, D. McCormick, D. J. Miller, T. J. Orimoto, Z. Szalata, M. Thomson, D. Ward, M. Wing, and M. Woods. Cavity BPM system tests for the ILC energy spectrometer. *Nuclear Instruments and Methods in Physics Research Section A: Accelerators, Spectrometers, Detectors and Associated Equipment*, 592(3):201–217, 7/21 2008.

[44] D. Xiang. Imaging of high-energy electron beam profile with optical diffraction radiation. *Phys.Rev.ST Accel.Beams*, 10(062801), 2007.

[45] D. Rubin, D. Sagan, and J. Shanks. CesrTA layout and optics. In *Proceedings, 23rd Conference, PAC'09*, page WE6PFP103, 2010.

[46] T. Behnke, J. E. Brau, B. Foster, J. Fuster, M. Harrison, J. M. Paterson, M. Peskin, M. Stanitzki, N. Walker, and H. Yamamoto. The international linear collider technical design report. Volume 1 Executive Summary, 2013.

[47] LEPP CesrTA. CESR with the CLEO and CHESS experimental areas.

[48] The CESR storage ring.

[49] N. T. Rider, M. G. Billing, M. P. Ehrlichman, D. P. Peterson, D. Rubin, J. P. Shanks, and K. G. Sonnad. Operation of a single pass, bunch-by-bunch x-ray beam size monitor for the CESR test accelerator research program. page 585, 2012.

[50] S. T. Wang, D. L. Rubin, J. Conway, M. Palmer, D. Hartill, R. Campbell, and R. Holtzapple. Visible-light beam size monitors using synchrotron radiation at CESR. *Nuclear Instruments and Methods in Physics Research Section A: Accelerators, Spectrometers, Detectors and Associated Equipment*, 703(0):80–90, 3/1 2013.

[51] D. P. Peterson, J. P. Alexander, C. Conolly, N. Eggert, E. Fontes, W. Hopkins, B. Kries, A. Lyndaker, M. McDonald, M. Palmer, M. Rendina, P. Revesz, N. Rider, J. Savino, R. Seeley, and J. W. Flanagan. CESRTA x-ray beam size monitor operation. In *Proceedings of IPAC'10*, page 1194, 2010.

[52] S. Wang, D. L. Rubin, and C. R. Strohman. A turn-by-turn beam profile monitor using visible synchrotron radiation at CESR-TA. In *Proceedings of IPAC2013*, page 849, 2013.

[53] S. T. Wang, J. Conway, M. Palmer, D. Hartill, D. L. Rubin, R. Campbell, and R. Holtzapple. Horizontal beam-size measurements at CESR-TA using synchrotron-light interferometer. In *Proceedings of IPAC2012*, 2012.

[54] L. Remandet. Target metrology, EDMS.1274854, CERN.

[55] M. S. Kulkarni and H. F. Erk. Acid-based etching of silicon wafers: Mass-transfer and kinetic effects. *Journal of The Electrochemical Society*, 147(1):176, 2000.

[56] S. Kerdiles, C. Duret, A. Vaufredaz, and F. Metral. Process for bonding by molecular adhesion, 2012.

[57] Jean M. Bennett and Harold E. Bennet. *Polarization*, pages 10–9. Handbook of Optics (sponsored by the Optical Society of America). McGraw-Hill Book Company, New York, 1978.

[58] Edward D. Palik. *Handbook of Optical Constants of Solids*, volume 1-3. Elsevier Inc, 1997.

[59] T. Aumeyr, M. G. Billing, L. M. Bobb, B. Bolzon, E. Bravin, P. Karataev, K. Kruchinin, T. Lefevre, and S. Mazzoni. Advanced simulations of optical transition and diffraction radiation. *Phys.Rev.ST Accel.Beams*, 18(4):042801, 2015.

[60] T. Aumeyr, P. Karataev, M. G. Billing, L. M. Bobb, B. Bolzon, T. Lefvre, and S. Mazzoni. ZEMAX simulations for an optical system for a diffraction radiation monitor at CesrTA. In *IPAC 2013*.

[61] ESRF. Synchrotron radiation workshop (SRW), 2009.

[62] G Naumenko, X Artru, A Potylitsyn, Yu Popov, and M.Shevelev L Sukhikh and. "shadowing" of the electromagnetic field of relativistic charged particles. *Journal of Physics: Conference Series*, 236(1):012004, 2010.

[63] Alexander Wu Chao and Maury Tigner. *2.1.1 Phase Space, Linear Betatron Motion*, page 65. Handbook of Accelerator Physics and Engineering. World Scientific, Singapore, second edition, 1999. Imported from Invenio.